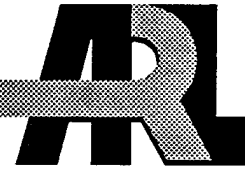


ARMY RESEARCH LABORATORY



Hydrocode Simulation of the Formation and Penetration of a Linear Shaped Demolition Charge Into an RHA Plate

G. A. Gazonas
S. B. Segletes
S. R. Stegall
C. V. Paxton



ARL-TR-788

July 1995

19951011 068

APPROVED FOR PUBLIC RELEASE; DISTRIBUTION IS UNLIMITED.

DTIC QUALITY INSPECTED 5

NOTICES

Destroy this report when it is no longer needed. DO NOT return it to the originator.

Additional copies of this report may be obtained from the National Technical Information Service, U.S. Department of Commerce, 5285 Port Royal Road, Springfield, VA 22161.

The findings of this report are not to be construed as an official Department of the Army position, unless so designated by other authorized documents.

The use of trade names or manufacturers' names in this report does not constitute endorsement of any commercial product.

REPORT DOCUMENTATION PAGE

*Form Approved
OMB No. 0704-0188*

Public reporting burden for this collection of information is estimated to average 1 hour per response, including the time for reviewing instructions, searching existing data sources, gathering and maintaining the data needed, and completing and reviewing the collection of information. Send comments regarding this burden estimate or any other aspect of this collection of information, including suggestions for reducing this burden, to Washington Headquarters Services, Directorate for Information Operations and Reports, 1215 Jefferson Davis Highway, Suite 1204, Arlington, VA 22202-4302, and to the Office of Management and Budget, Paperwork Reduction Project (0704-0188), Washington, DC 20503.

1. AGENCY USE ONLY (Leave blank)	2. REPORT DATE	3. REPORT TYPE AND DATES COVERED	
	July 1995	Final, Jan-Dec 1994	
4. TITLE AND SUBTITLE			5. FUNDING NUMBERS
Hydrocode Simulation of the Formation and Penetration of a Linear Shaped Demolition Charge Into an RHA Plate			PR: 4G015-402-P4
6. AUTHOR(S)			
G. A. Gazonas, S. B. Segletes, S. R. Stegall, and C. V. Paxton			
7. PERFORMING ORGANIZATION NAME(S) AND ADDRESS(ES)			8. PERFORMING ORGANIZATION REPORT NUMBER
U.S. Army Research Laboratory ATTN: AMSRL-WT-PD Aberdeen Proving Ground, MD 21005-5066			ARL-TR-788
9. SPONSORING / MONITORING AGENCY NAME(S) AND ADDRESS(ES)			10. SPONSORING / MONITORING AGENCY REPORT NUMBER
11. SUPPLEMENTARY NOTES			
12a. DISTRIBUTION / AVAILABILITY STATEMENT		12b. DISTRIBUTION CODE	
Approved for public release; distribution is unlimited.			
13. ABSTRACT (Maximum 200 words)			
<p>This report presents the results of a combined experimental and numerical investigation of the formation and penetration of a linear shaped demolition charge into a rolled homogeneous armor (RHA) plate. The demolition charge is composed of a mild steel liner, filled with castable Composition-B high explosive. The numerical computations were conducted before the experiments using the Lagrangian hydrocode EPIC92 and predict a jet tip free flight velocity of about 5.2 km/s at 12 μs. However, observed jet tip free flight velocities of the linear shaped charge (LSC) range from 3.3 to 3.5 km/s as determined from flash radiography, and 3.5 km/s using a special electrical makewire circuit test fixture. The reason for the large discrepancy between the predicted and observed jet tip free flight velocities appears to be related to computational inaccuracies resulting from the highly distorted computational mesh in the collapsing liner. Using the automatic rezone feature in the EPIC94 version of the hydrocode results in the reduction of the jet tip velocity from 4.7 km/s to 3.8 km/s at 4 μs. However, computations beyond 4 μs were not possible due to numerical instabilities associated with requiring a vanishingly small integration time increment resulting from an equation-of-state instability. Penetration depths into two rectangular, 2-in-thick (50.8 mm) RHA plates measure 17 and 18 mm respectively, whereas the hydrocode simulation predicts a greater penetration depth of 22.9 mm. The work attests to the importance of conducting experiments in order to verify baseline hydrocode simulations.</p>			
14. SUBJECT TERMS		15. NUMBER OF PAGES	
linear shaped charge; hydrocode; demolition charge; rolled homogeneous armor (RHA)		85	
16. PRICE CODE			
17. SECURITY CLASSIFICATION OF REPORT	18. SECURITY CLASSIFICATION OF THIS PAGE	19. SECURITY CLASSIFICATION OF ABSTRACT	20. LIMITATION OF ABSTRACT
UNCLASSIFIED	UNCLASSIFIED	UNCLASSIFIED	UL

INTENTIONALLY LEFT BLANK.

ACKNOWLEDGMENTS

This work was supported by the Naval Explosive Ordnance Disposal (NAVEOD) Technology Center, Indian Head, MD, under U.S. Army Research Laboratory (ARL) Work Order No. 4G015-402-P4. The authors would like to acknowledge the overall assistance of Mr. Atul Patel and Mr. Richard Gold of NAVEOD with regards to the linear shaped charge demolition problem. Thanks also go to Mr. Todd Bjerke and Mr. Richard Gold for their constructive reviews.

Accesion For	
NTIS	CRA&I <input checked="" type="checkbox"/>
DTIC	TAB <input type="checkbox"/>
Unannounced <input type="checkbox"/>	
Justification _____	
By _____	
Distribution / _____	
Availability Codes	
Dist	Avail and / or Special
A-1	

INTENTIONALLY LEFT BLANK.

TABLE OF CONTENTS

	<u>Page</u>
ACKNOWLEDGMENTS	iii
LIST OF FIGURES	vii
1. INTRODUCTION.....	1
2. COMPUTATIONS.....	2
2.1 LSC Jet Formation	5
2.2 LSC Jet Penetration	12
3. EXPERIMENTS	12
3.1 Free Flight LSC Jet Tip Velocity (Makewire Circuit)	12
3.2 Free Flight LSC Jet Tip Velocity (Orthogonal X-rays)	15
3.3 LSC Jet Penetration Measurements.....	17
4. COMPARISON OF COMPUTATIONS AND EXPERIMENTS	20
5. CONCLUSIONS	24
6. REFERENCES	25
APPENDIX A: SHAPED CHARGE JET FORMATION INPUT DECK AND COMPUTATIONAL RESULTS.....	27
APPENDIX B: SHAPED CHARGE JET PENETRATION INPUT DECK AND COMPUTATIONAL RESULTS.....	45
DISTRIBUTION LIST	79

INTENTIONALLY LEFT BLANK.

LIST OF FIGURES

<u>Figure</u>		<u>Page</u>
1. Critical dimensions of the Mk-7 Mod 8 demolition charge	1	
2. Computational mesh for jet formation problem (in meters).....	3	
3. Adiabatic flow stress versus equivalent plastic strain for 1006 mild steel as a function of strain rate.....	3	
4. JWL equation of state isentrope for Comp-B	4	
5. a) Computational mesh, b) Magnified computational mesh in the vicinity of the shaped charge jet tip (in meters).	5	
6. Prediction of jet contour at 12 μ s (solid line) versus hydrocode simulation (dots)	6	
7. LSC jet geometry at 12 μ s (in meters).	7	
8. Cumulative jet mass versus position at 12 μ s.....	7	
9. Axial velocity versus position at 12 μ s	8	
10. Cumulative mass versus velocity at 12 μ s.....	8	
11. Nodal mass points in simulated jet compared to fit using (v,z) and dM/dz data at 12 μ s	11	
12. Nodal mass points in simulated jet compared to fit using (v,z) and dM/dz data interpolated back to 8 μ s.....	11	
13. Idealized jet contour impinging upon monolithic target at 7.2 μ s.....	12	
14. Plexiglas makewire test fixture for free flight velocity measurement (RHA witness plate is 1-in [25.4 mm]-thick).....	13	
15. Oscilloscope traces.	14	
16. Test configuration for free flight velocity measurement	15	

LIST OF FIGURES (continued)

<u>Figure</u>		<u>Page</u>
17.	Radiographic film cassette damaged by LSC liner fragment	16
18.	Liner imprint on wall of test facility.....	16
19.	X-ray radiograph of LSC (axial view) 73.5 μ s	17
20.	LSC test configurations a) nonuniform, and b) uniform.	18
21.	Damaged RHA plate (plan view) for nonuniform standoff test. Detonation wave traveled from left to right (indicated by arrows).	19
22.	Cross sections through a) RHA plate 2-in (50.8 mm)-thick, and b) Mild steel plate 1-in (25.4 mm)-thick	20
23.	Jet velocity versus axial position at 4 μ s and 12 μ s a) Original liner with erosion = 0.0, b) Dense mesh, c) Dense mesh with flat liner, d) Modified dense mesh, flat inner liner with apex angle = 82 $^{\circ}$	21
24.	Computational mesh (magnified) for the dense liner in the vicinity of the liner apex at: a) t = 0 μ s, and b) t = 4 μ s	23
25.	Computational mesh (magnified) for the modified dense mesh in the vicinity of the liner apex at: a) t = 0 μ s, and b) t = 4 μ s	23
26.	Computational mesh (magnified) rezoned at: a) t = 2 μ s, and b) t = 4 μ s	23

1. INTRODUCTION

Military demolition operations use a variety of shaped charge geometries (e.g., cylindrical, linear, curvilinear, and flexilinear) for the clearance of obstacles and barriers, the destruction of facilities and materiel, the construction of roads and trenches, and in land clearance and quarrying. The linear shaped charge (LSC) is commonly used in explosive ordnance disposal (EOD) as a means to initially cut open cases containing explosive-filled ordnance. The Mk-7 Mod 8 demolition charge (Figure 1) consists of an inert mild steel container (liner) filled with plastic explosive (e.g., C-4). A blasting cap is placed on the top surface of the explosive to prime the charge.

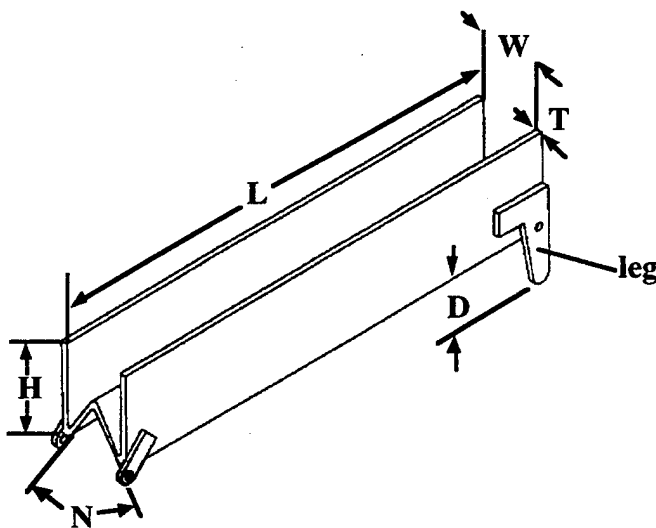


Figure 1. Critical dimensions of the Mk-7 Mod 8 demolition charge (Department of the Navy EOBD/Department of the Army TM/U.S. Air Force TO 60A-2-1-51 1992).

The charges may be used individually or linked together in a continuous series if a long cut is desired. Linking several individual charges together in series is achieved by connecting the short leg of one charge to the long leg of an adjacent charge; in this configuration, the charge has a uniformly short standoff distance on the order of 28 mm (1.1 in), in the series arrangement (the dimensions of the Mk-7 Mod 8 charge are: $N = 800$, $W = 1.00$ in [25.4 mm], $T = 0.053$ in [1.35 mm], $H = 1.12$ in [28.45 mm], $L = 6.0$ in [152.4 mm], and $D = 1.06$ in [26.92 mm]).

The experimental determination of optimal jet cutting properties for a particular EOD application requires parametric variation of design variables such as the liner material, liner geometry, standoff distance, and explosive properties. Since experiments can be costly and hazardous to conduct, there is a strong motivation to develop numerical methods using hydrocodes to assist in the development of EOD procedures. Even though the Mk-7 series of demolition charges have a well-defined penetration depth

into steel and aluminum, these LSCs are known to produce low-order or high-order detonations (see Department of the Navy EODB/Department of the Army TM/U.S. Air Force TO 60A-2-1-51 1992). In this study, we use the Lagrangian-based hydrocode EPIC92 (Elastic Plastic Impact Calculations) (Johnson et al. 1992a, 1992b) to model the formation of an LSC (Mk-7 Mod 8 demolition charge), and its subsequent penetration into a 2-in (51 mm)-thick rolled-homogeneous-armor (RHA) plate. The incorporation of slideline erosion algorithms has permitted Lagrangian computations in large-scale penetration problems (Johnson 1984); nonetheless, Raftenberg (1994) points out that there are a paucity of shaped charge jet (SCJ) penetration studies using EPIC in the open literature. The Raftenberg (1994) study primarily concentrates on failure modeling of a thin RHA target perforated by a shaped charge of relatively long standoff distance; in that work, a 7.73 km/s particulated-copper jet tip is simulated by a 5-parameter geometric model using flash radiographic data. In this study, however, the jet is continuous and has a short standoff distance. Since the jet tip begins interacting with the RHA target almost immediately after it is formed, it is difficult to characterize the jet geometry using radiographic methods. For this reason, in this study, we model *both* the formation and penetration of the LSC using the EPIC92 hydrocode.

Experiments were performed for which the jet tip free flight velocity data are obtained from flash radiographs, and from a test fixture that is specially designed to measure the free flight velocity of the jet using a makewire circuit. These data are compared with the hydrocode velocity predictions in order to assess EPIC92 computational accuracy for the jet *formation* problem. The hydrocode computations were performed first, followed by the experiments, in order to avoid the bias inherent in studies which “tweak” the simulation parameters so as to exactly fit the experiment. Indeed, one of the motivations of the current study is to assess the accuracy of the hydrocode in instances where experimental data are lacking, such as in demolition work where data can be hazardous or costly to obtain. In addition, we compare the depth of penetration into the RHA target with the penetration depth predicted by the hydrocode. Finally, the accuracy in predicting the penetration depth will be shown to be a direct function of our ability to accurately model the formation of the jet.

2. COMPUTATIONS

Computations were performed using the Lagrangian-based explicit EPIC92 hydrocode (Johnson 1977; Johnson et al. 1992a, 1992b) that has been primarily used in the analysis of terminal ballistic or hypervelocity impact problems.

In the current case, we are trying to idealize the jet from an Mk-7 LSC, so that a rezoned version of the problem, without the difficulties associated with the distorted grid, may be employed to simulate the jet penetration. Our problem is further complicated by the fact that the jet must be idealized at a relatively late point in the jet formation process (chosen at 12 μ s), so that the rear of the jet is formed,

and is thus characterizable; yet the penetration simulation to follow is at such a short standoff that the resultant idealization must be backed up in time (to 7.2 μ s) to the onset of penetration. The initial grid for the jet formation problem appears in Figure 2. It consists of 1,485 nodes and 2,732 finite elements. The initial finite element grid was generated from the charge geometry given in the Introduction. The input deck and computational results out to 20 μ s appear in Appendix A.

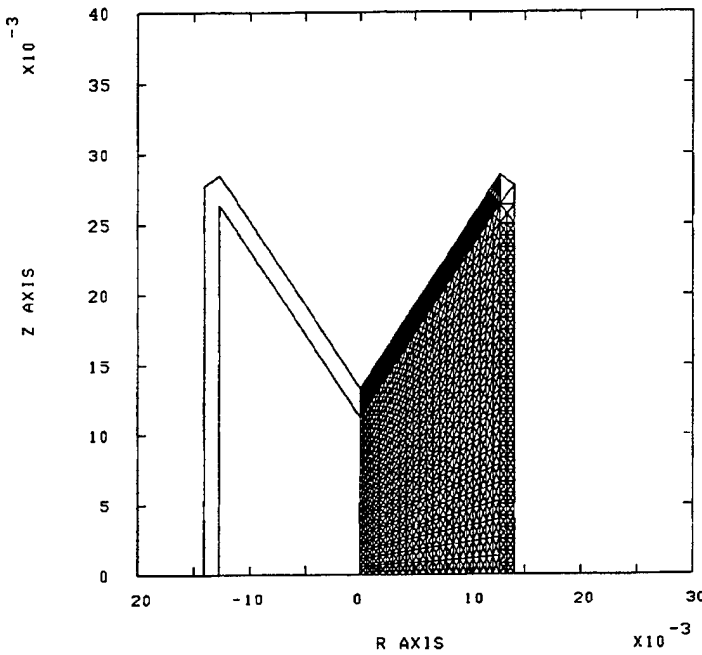


Figure 2. Computational mesh for jet formation problem (in meters).

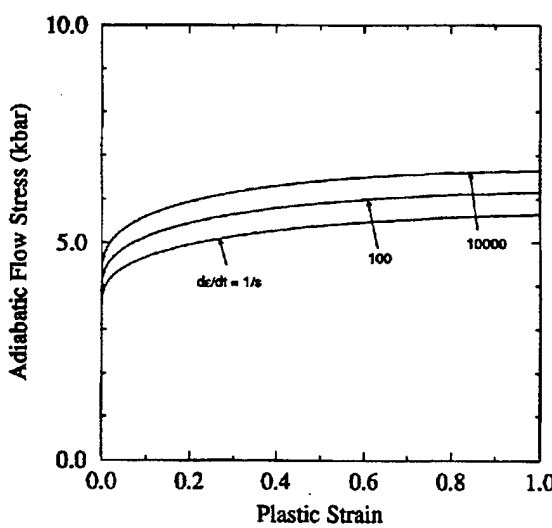


Figure 3. Adiabatic flow stress versus equivalent plastic strain for 1006 mild steel as a function of strain rate.

The distortional behavior of the mild steel liner material is modeled using the Johnson-Cook viscoplastic constitutive model (Johnson and Cook 1985) together with a von Mises initial yield condition (EPIC92 material model 6, 1006 steel, Figure 3). An isotropic hardening rule governs subsequent yield surface behavior together with a radial-return algorithm (Johnson 1984; Cook, Rajendran, and Grove 1992). Because of the high strain rates encountered in impact problems, the temperature fields in bodies modeled using EPIC92 are adiabatic ($dQ = 0$, i.e., there is no heat flow within the body) and thermal softening of a material element is directly proportional to the amount of accumulated plastic work. The dilatational behavior of the Comp-B high explosive is modeled using the Jones-Wilkins-Lee (JWL) equation of state (EPIC92 material model 43, Figure 4). The entire cross section of the finite element charge is simultaneously detonated in order to approximate a 2-D plane detonation wave traveling along the length of the charge.

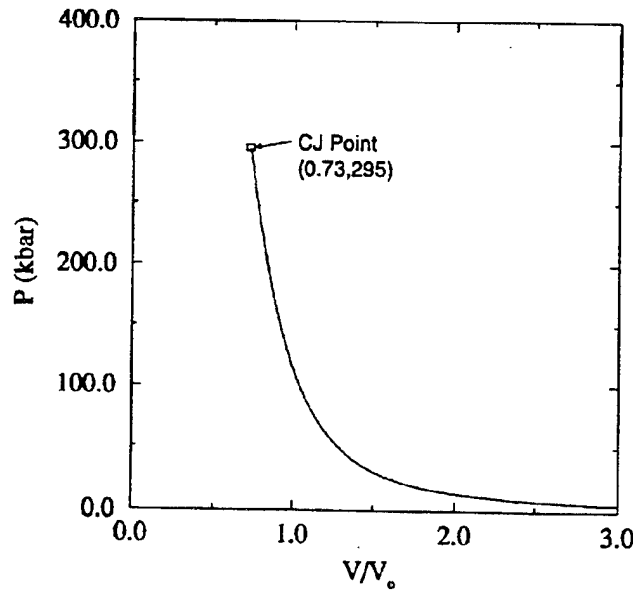


Figure 4. JWL equation-of-state isentrope for Comp-B.

The damage criterion in EPIC92 is assumed to be a scalar function of the incremental (cumulative) equivalent plastic strain, normalized with respect to the fracture strain (Johnson et al. 1992a, 1992b). If the damage threshold is exceeded in a particular finite element, the element behaves as a fluid, and cannot sustain shear or tensile stresses. EPIC92 has the capability of handling severe distortions encountered in SCJ penetration problems using an element erosion algorithm that eliminates

element volume, but retains element mass (e.g., when a critical value of the equivalent plastic strain is exceeded).

The initial mesh geometry for the penetration computations is illustrated in Figure 5. The initial geometry was derived based on the results of the jet formation simulation to be subsequently described. At the start of the computation, both the tip of the LSC jet and RHA target are in normal contact.

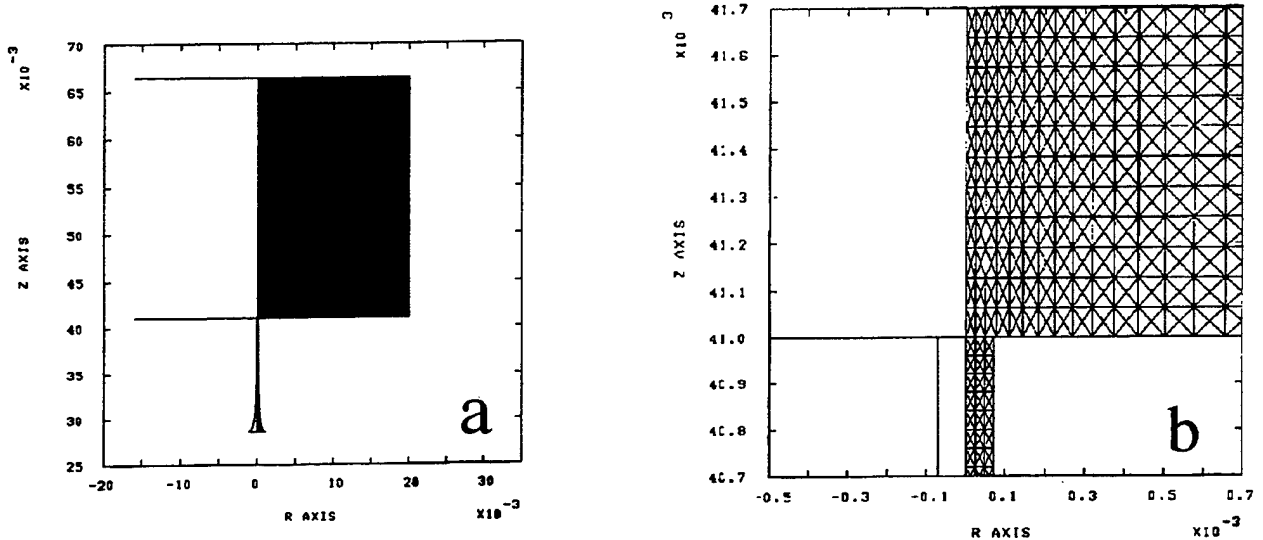


Figure 5. a) Computational mesh, b) Magnified computational mesh in the vicinity of the shaped charge jet tip (in meters).

The linear contact region between jet tip and target describes a locus of slideline points wherein both the jet tip and the target have been alternately defined as master and slave erosional surfaces. This procedure permits both the jet and the target to erode during the penetration process. The entire jet penetration simulation consists of 37,224 finite elements and 19,300 nodes; however, 3,720 elements and 2,170 nodes comprise the jet geometry, while the remainder are in the target. The finite elements are 2-D plane strain constant strain triangles (CSTs), with an assumed displacement field which varies linearly within each finite element. The jet *penetration* computations are described in detail in Section 2.2. In the next section, we more fully describe the details and difficulties encountered in modeling the jet *formation* problem.

2.1 LSC Jet Formation. When simulating the collapse and jet formation of a shaped charge, the resultant velocity distribution in the simulated jet is a function not only of axial location (which the idealized theories assume), but also of radial distance (Walters and Zukas 1989). Similarly, the discretized nature of Lagrangian simulations is such that additional velocity scatter along the simulated

jet occurs. This scattered velocity distribution poses problems when trying to idealize the jet in one dimension for subsequent modeling and/or analysis. The problem is modeled in 2-D plane strain, and therefore, to simulate a plane detonation wave traveling normal to the cross section of the LSC, all of the Comp-B is assumed to simultaneously detonate at the start of the simulation.

We first fit a curve directly to the cumulative mass distribution as a function of jet velocity, thus obtaining $M(v)$. Unfortunately, the velocity scatter inherent in the jet formation simulation caused the poor resultant fit, when viewed in terms of mass versus position (i.e., jet geometry). An enlarged view of this poor fit is shown in Figure 6, where the curve predicting the outer contour of the jet is compared to the liner's node points of the computer simulation at 12 μs .

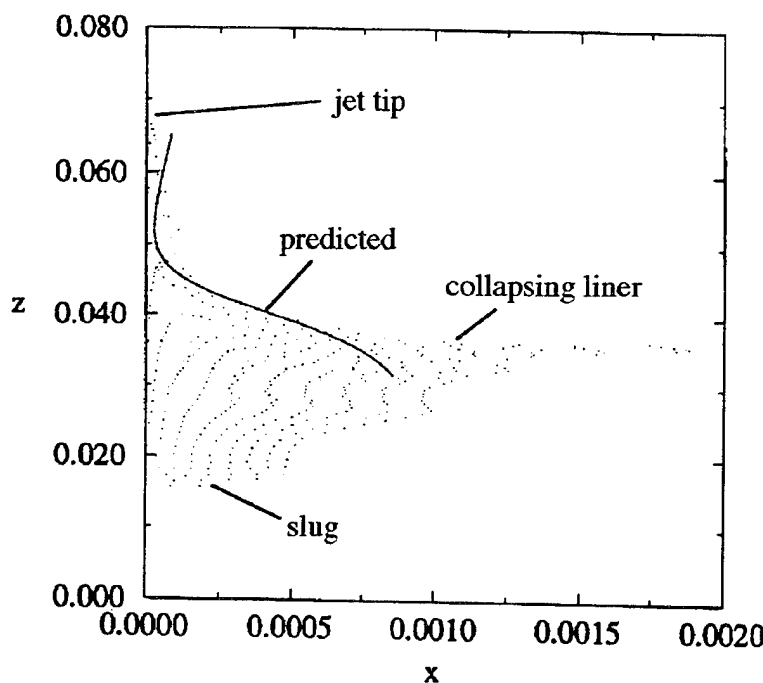


Figure 6. Prediction of jet contour at 12 μs (solid line) versus hydrocode simulation (dots)
(length dimensions in meters, not to scale).

The full grid of the jet formation simulation at 12 μs is shown in Figure 7. The original inner steel liner consists of 446 nodes and 800 elements. In light of this unacceptable fit, a second approach was taken, whereby cumulative jet mass was fit as a function of axial jet coordinate at the selected fitting time, $\bar{t} = 12 \mu\text{s}$, giving $M(\bar{z})$ (see Figure 8). Use of this fit to axial location should guarantee a good fit to the jet geometry. If a reasonable fit can be made to the scattered data of axial position versus jet velocity, $\bar{z} = \bar{z}(v)$ (see Figure 9), then the fit to cumulative mass versus velocity may be derived by combining

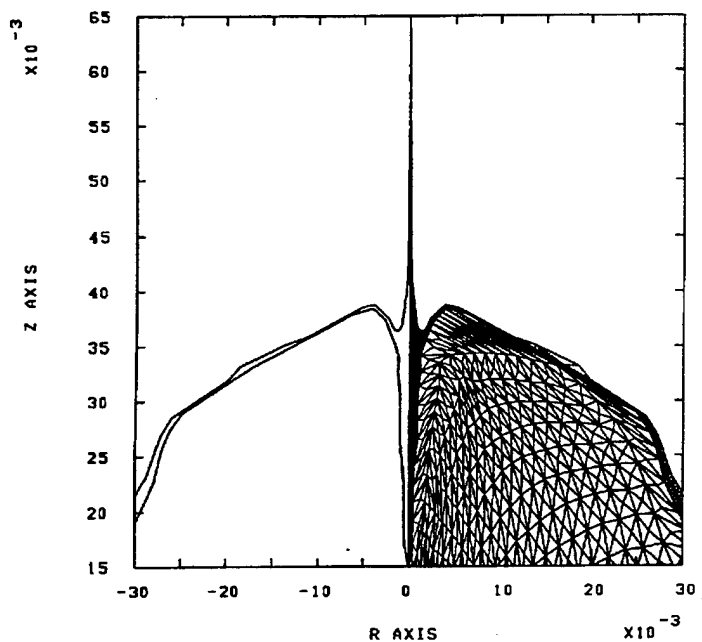


Figure 7. LSC jet geometry at 12 μ s (in meters).

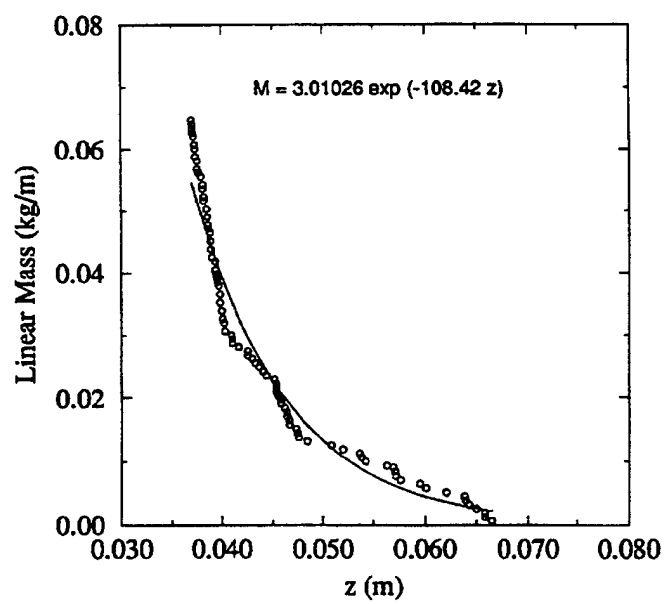


Figure 8. Cumulative jet mass versus position at 12 μ s.

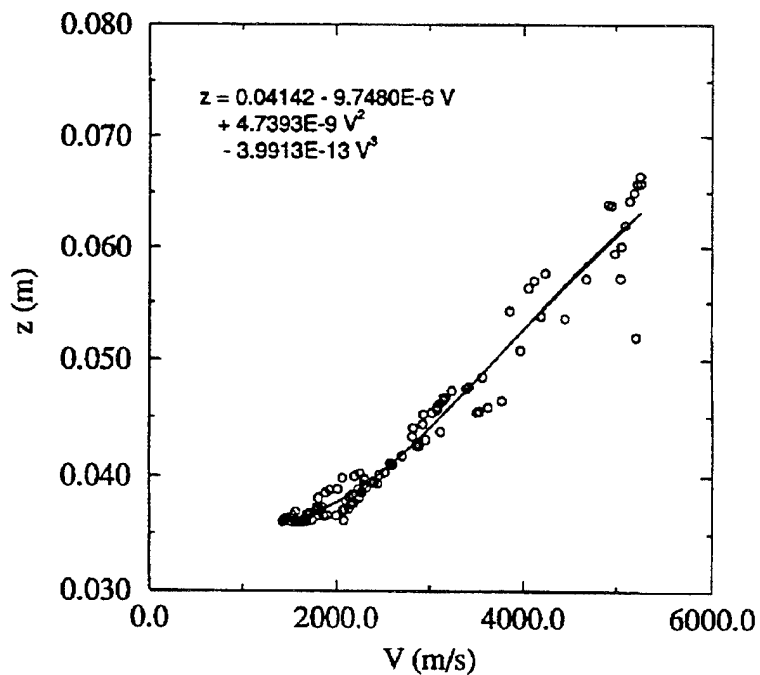


Figure 9. Axial velocity versus position at 12 μ s.

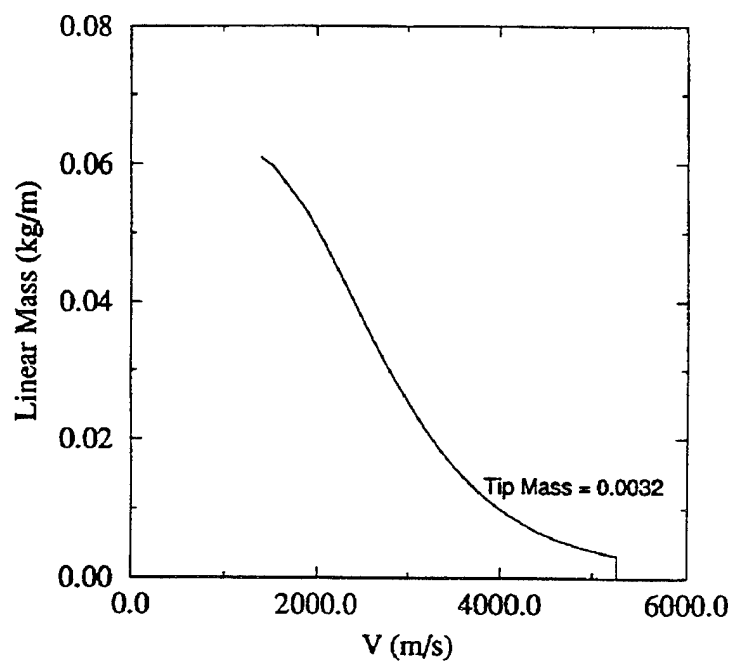


Figure 10. Cumulative mass versus velocity at 12 μ s.

the two fits; thus, $M(v) = M(\bar{z}(v))$ (see Figure 10). The following fitting forms have been employed for this particular data set in question:

$$M(\bar{z}) = Ke^{-B\bar{z}} \quad (1)$$

$$\bar{z}(v) = C_0 + C_1 v + C_2 v^2 + C_3 v^3 \quad , \quad (2)$$

where K, B and the C terms are fitting constants. Thus, cumulative mass is obtainable in terms of jet velocity, and its derivative also, given by

$$\frac{dM}{dv} = -KB \frac{d\bar{z}}{dv} e^{-B\bar{z}} \quad (3)$$

for the fitting forms proposed.

For a linear shaped charge jet of unit depth, density ρ , and half-thickness d , the derivative of the cumulative mass curve is described by

$$\frac{dM}{dz} = -2\rho d \quad . \quad (4)$$

If the cumulative mass distribution is known, and it is the jet half thickness to be determined, simple algebraic manipulation and the use of the chain rule provide that

$$d = \frac{-dM/dv}{2\rho dz/dv} \quad . \quad (5)$$

The cumulative mass derivative is given above in Equation 3, using parameters from the fits, while the position derivative will now be described.

The axial coordinate, \bar{z} , applies specifically at the fitting time of 12 μ s. By assuming that the jet particles do not accelerate after the jet is formed (i.e., constant velocity jet particles), the axial coordinate of a jet particle at any time may be directly obtained from

$$z = \bar{z} + v(t - \bar{t}) \quad . \quad (6)$$

With this equation, the derivative of position versus velocity is simply

$$\frac{dz}{dv} = \frac{d\bar{z}}{dv} + (t - \bar{t}) \quad . \quad (7)$$

Again, the \bar{z} derivative is obtainable from the data fit in Equation 2. Combining and substituting these terms gives the fit to the jet half thickness as

$$d(v, t) = \frac{KB(d\bar{z} / dv)e^{-B\bar{z}}}{2\rho(d\bar{z} / dv + t - \bar{t})} \quad . \quad (8)$$

For the jet tip of given mass, M_0 , a half diameter $d_0 = d(v_0)$ is assumed and length L_0 is computed via

$$L_0 = \frac{M_0}{2\rho d_0} \quad . \quad (9)$$

The geometric fit, using the current technique, is shown at 12 μ s (Figure 11). The fit is good from the jet tip back to the location $\bar{z} = 0.041$ m, corresponding to a jet velocity of approximately 2.5 km/s. It is believed that the relative jet thickness is large enough at this jet location so that the “effective” tail of the jet will lie ahead of this location. Thus, the divergent fit behind this location should not affect the penetration capability of the jet. Figure 12 depicts the jet fit, backed up in time to 8 μ s, and compares it to the hydrocode results at that time. As can be seen, the fit to the jet contour, and thus the technique for backing up the idealization in time, properly accounts for mass continuity over time. Figure 13 provides a not-to-scale geometrical representation of the idealized jet contour impinging upon the monolithic target at 7.2 μ s in time. The target location was chosen 12.7 mm (0.5 in) from the original Mk-7 liner base, which is a representative standoff at which the device is employed. Again, Figure 5b shows the computational grid in a closeup at the jet/target interface, depicting the grid resolution. In the current configuration, the jet penetration simulation has 26,444 elements and 13,855 nodes (Figure 5a).

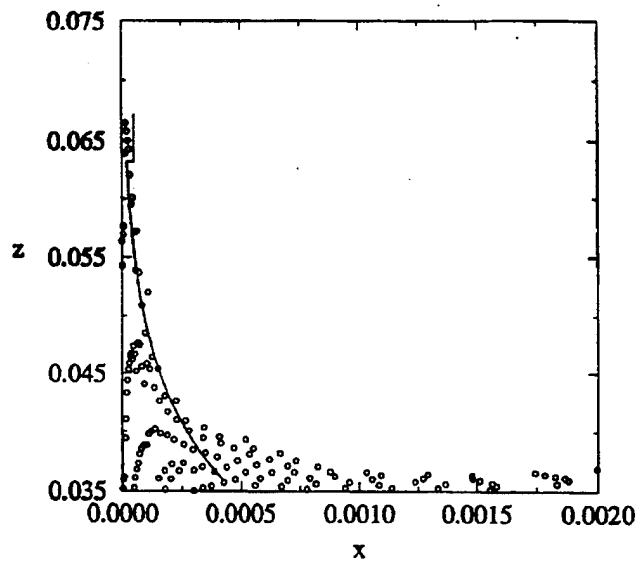


Figure 11. Nodal mass points in simulated jet compared to fit using (v,z) and dM/dz data at 12 μ s (length dimensions in meters, not to scale).

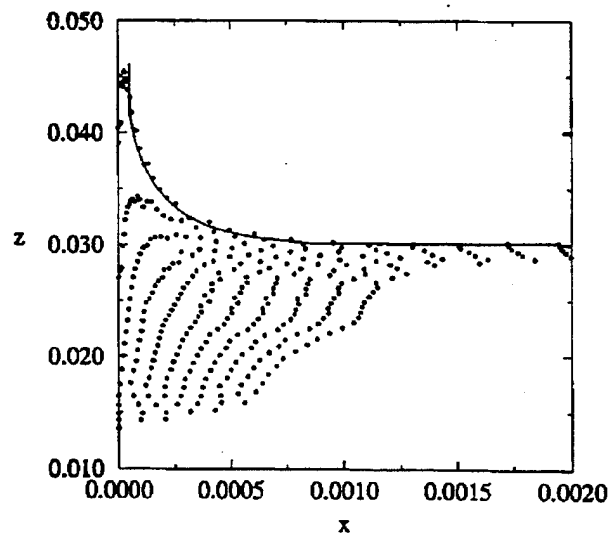


Figure 12. Nodal mass points in simulated jet compared to fit using (v,z) and dM/dz data interpolated back to 8 μ s (length dimensions in meters, not to scale).

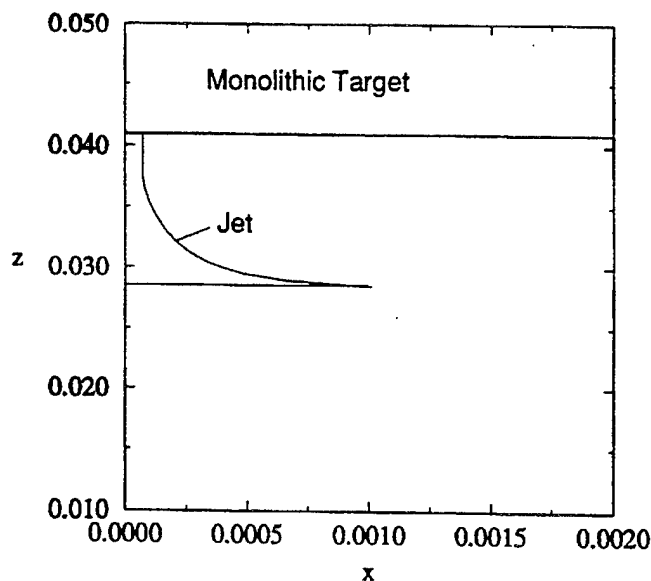


Figure 13. Idealized jet contour impinging upon monolithic target at 7.2 μ s
(length dimensions in meters, not to scale).

2.2 LSC Jet Penetration. Having fully characterized the LSC jet geometry and initial velocity, we proceed to solve the *penetration* problem. The complete LSC penetration simulation is illustrated at 4 μ s time intervals in Appendix B. Although the RHA plate used in the experiment was 2-in (50.8 mm)-thick, we chose to reduce the size of the total problem by modeling a plate of only half the actual plate thickness (i.e., a 1-in [25.4 mm]-thick plate). We felt justified in using a reduced plate thickness in our simulation since the documented cutting depth for the Mk-7 Mod 8 LSC is only 18 mm (0.70 in) (see Department of the Navy EODB/Department of the Army TM/U.S. Air Force TO 60A-2-1-51 1992). The EPIC92 input deck for the LSC jet penetration problem can also be found in Appendix B. The penetration depth of the jet is 24.5 mm when measured from the front plane of the target. If one accounts for target bulge as unpenetrated material, then penetrated thickness = original thickness - unpenetrated thickness = 25.4 mm - 2.5 mm = 22.9 mm.

3. EXPERIMENTS

3.1 Free Flight LSC Jet Tip Velocity (*Makewire Circuit*). The free flight velocity of the LSC was determined at ARL Range 17 by measuring the travel time of the jet as it consecutively severed three parallel double-lead wires, fastened to a plexiglas test fixture (Figure 14). As each wire is impinged by the electrically conductive jet, a circuit is completed sending a signal to an oscilloscope from which the travel time and velocity of the jet can be deduced. A breakwire circuit was not used because it might interact with the electrically conductive jet. A uniform standoff distance is assured by elevating the short legs of the liner with wooden spacers. The charge is detonated at one end by hotwire initiation

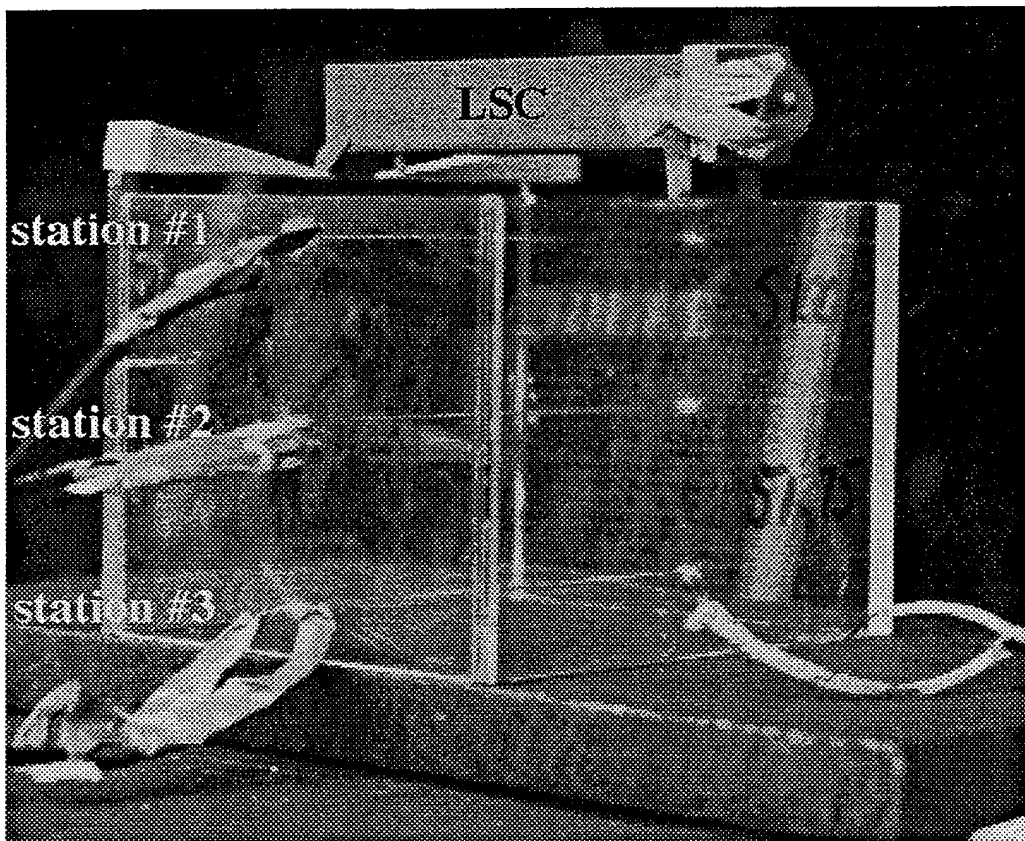


Figure 14. Plexiglas makewire test fixture for free flight velocity measurement
(RHA witness plate is 1-in [25.4 mm]-thick).

of two layers of C-6 Detasheet explosive that are press fit onto the Comp-B; each layer of Detasheet is about 6-mm thick. Detasheet is manufactured by Dupont and is composed of 68% PETN, 28% acetyl tributyl citrate, and 8 % nitrocellulose (Asay et al. 1994). The test fixture stands on a 1-in (25.4 mm)-thick rectangular witness plate composed of RHA. As the jet tip cuts through each double-lead, the wires are bridged, which completes the electrical *makewire* circuit. When the circuit is completed, a 67.5-volt signal is simultaneously discharged from a battery to a Nicolet model 2090 oscilloscope. Prior to detonating the charge, the oscilloscopes are triggered and begin to collect data at a sampling rate of 50 ns/pt. Two separate experiments were conducted to estimate the free-flight velocity of the jet. For Shot #1, the jet tip severs the first wire at station 1 (Figure 13), and oscilloscopes #1 and #3 record signals after 23.2 μ s and 22.8 μ s respectively (Figure 14). The jet tip severs the second wire at station 2, and oscilloscopes #1 and #2 record signals after 38.0 μ s respectively. Finally, the jet tip severs the third wire

at station 3, and oscilloscopes # 2 and #3 record signals at $52.95 \mu\text{s}$ and $52.5 \mu\text{s}$ respectively. A similar sequence of events occurs for Shot # 2 but with slightly different interstation distances and travel times (Figure 15). Jet velocities are deduced from these data. The test results are compiled in Table 1. The free flight jet tip velocity is found to average $3.52 \pm 0.10 \text{ km/sec}$ and is relatively constant over a total flight distance of about 4 in (100 mm).

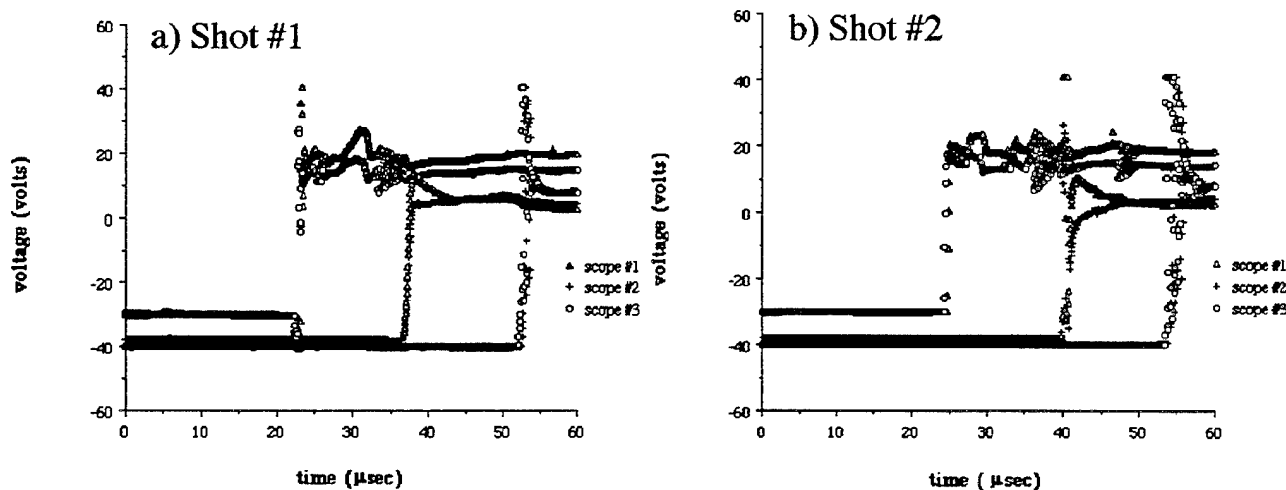


Figure 15. Oscilloscope traces.

Table 1. Free Flight Velocity Measurements

Shot #	Stations	Interstation Distance (mm)	Travel Time (μs)	Jet Tip Velocity (km/s)
1	1 to 2	51.0	14.8	3.445
	2 to 3	51.75	14.95	3.46
	1 to 3	102.75	29.7	3.46
2	1 to 2	51.5	14.9	3.456
	2 to 3	51.5	13.9	3.7
	1 to 3	103.0	28.85	3.57
average:				3.52

3.2 Free Flight LSC Jet Tip Velocity (*Orthogonal X-rays*). The free flight velocity of the LSC was also determined at ARL Range 16 by an orthogonal x-ray measurement method so that a direct comparison could be made to the electrical makewire measurement method. The experimental test configuration is illustrated in Figure 16. The LSC is shown suspended by two nylon ropes with radiographic film cassettes oriented at right angles relative to the charge. Our attempts to obtain orthogonal radiographs of the jet as it formed were unsuccessful because the radiographic film cassettes were damaged by laterally projected fragments of the steel liner (Figure 17). In one test, such a fragment remained relatively intact and created a rectangular imprint on the interior wall of the test facility (Figure 18). A shield was then constructed by cutting a rectangular hole in a 2-in (50.8 mm)-thick RHA plate. The LSC was suspended within the hole in an attempt to prevent the side fragments of the liner from puncturing the photographic plate; this test configuration was also relatively ineffectual in preventing photographic plate damage, so jet tip velocity had to be estimated from a single radiograph (Figure 19). Knowing the distance from the base of the LSC to the tip of the jet, one can determine the jet tip velocity from information about the test system time delays. Test system time delays were estimated at 3 μ s for predetonation electrical delay, 3 μ s for Datasheet burn delay, 3 μ s to 6 μ s for Comp-B burn delay, and 5 μ s for jet formation delay. The jet formation delay is the time required for the jet to emerge from the base of the LSC at a given cross section, once the detonation wave reaches that cross section, and is included in the delay times since all distance measures were made from the base of the LSC. The jet formation delay was determined from the hydrocode computations (see Appendix A).

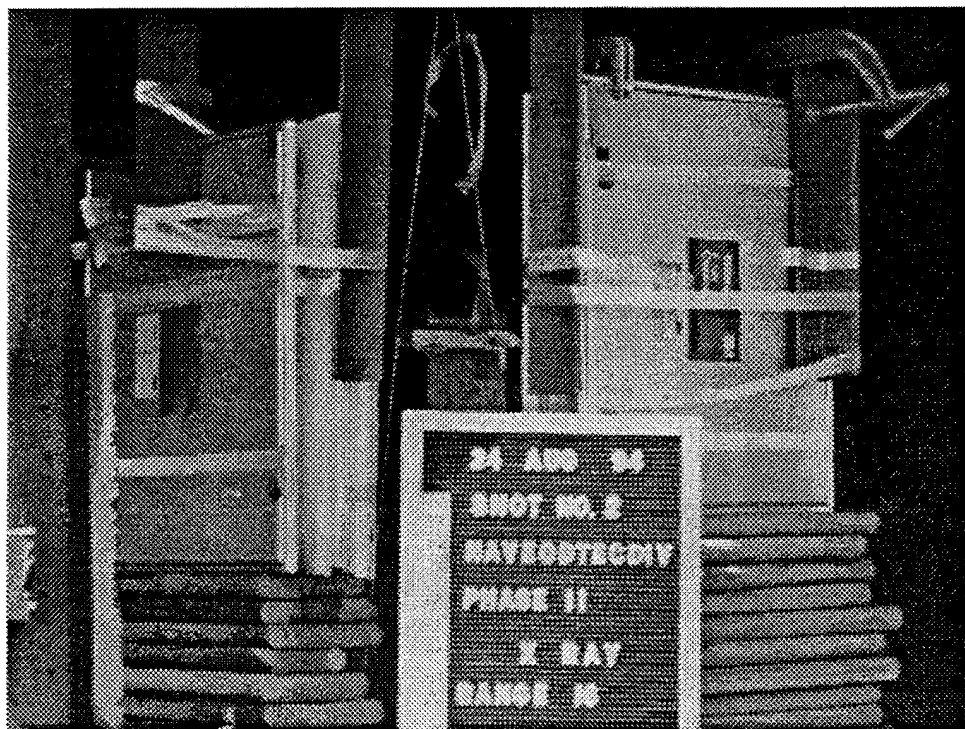


Figure 16. Test configuration for free flight velocity measurement.



Figure 17. Radiographic film cassette damaged by LSC liner fragment.

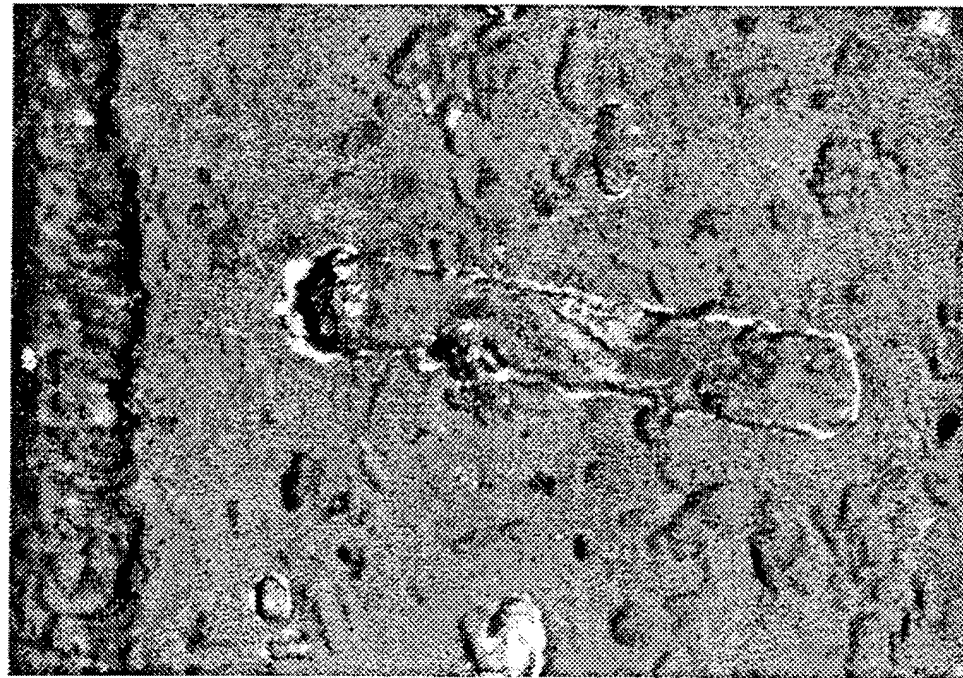


Figure 18. Liner imprint on wall of test facility

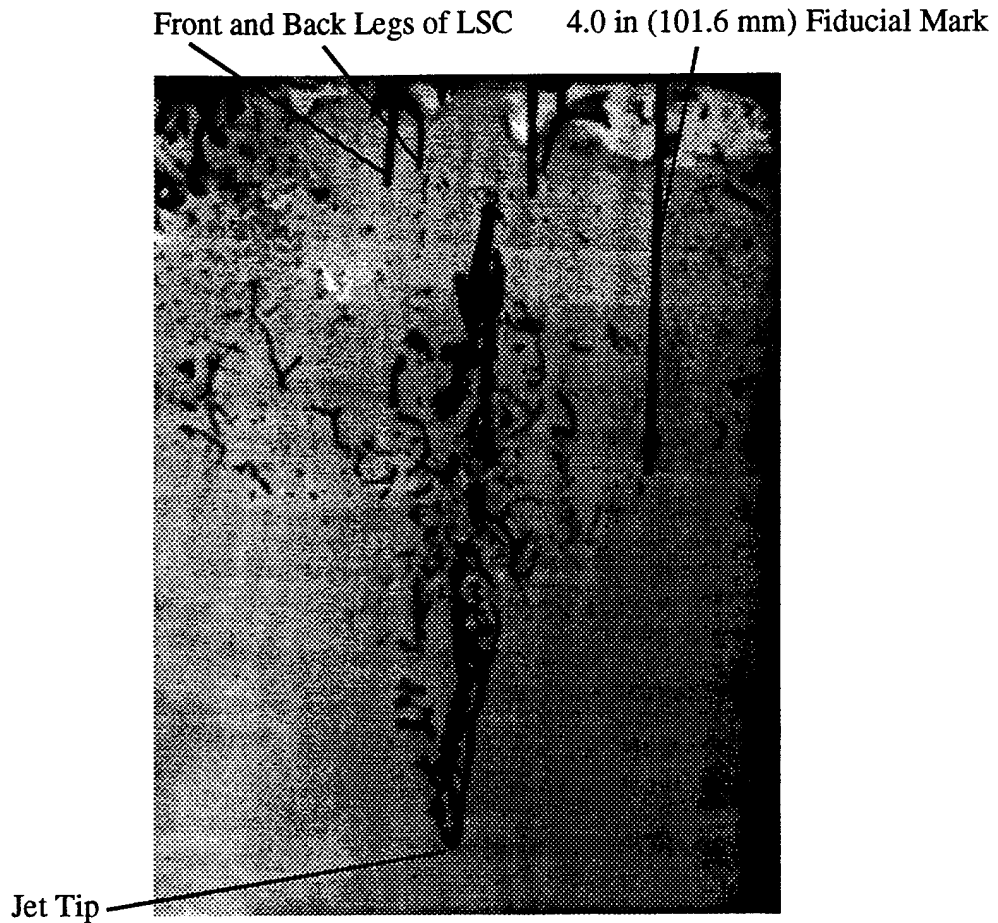
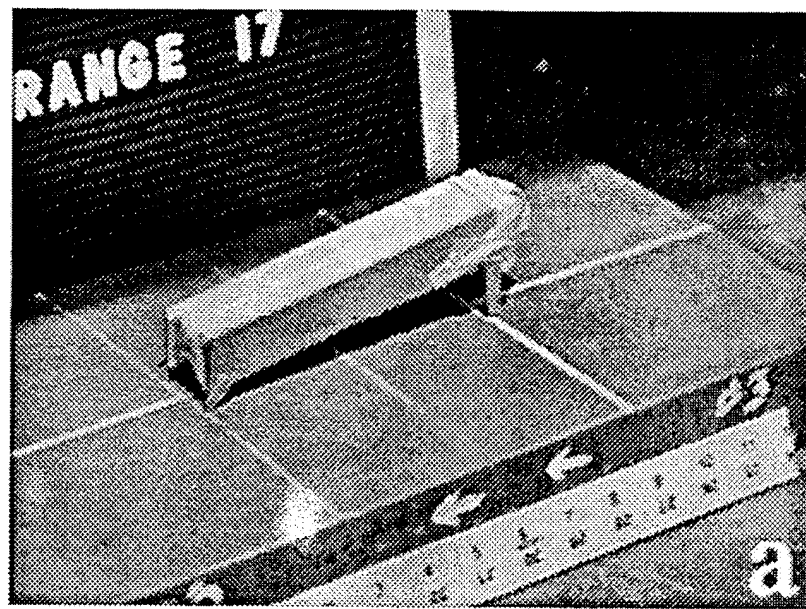


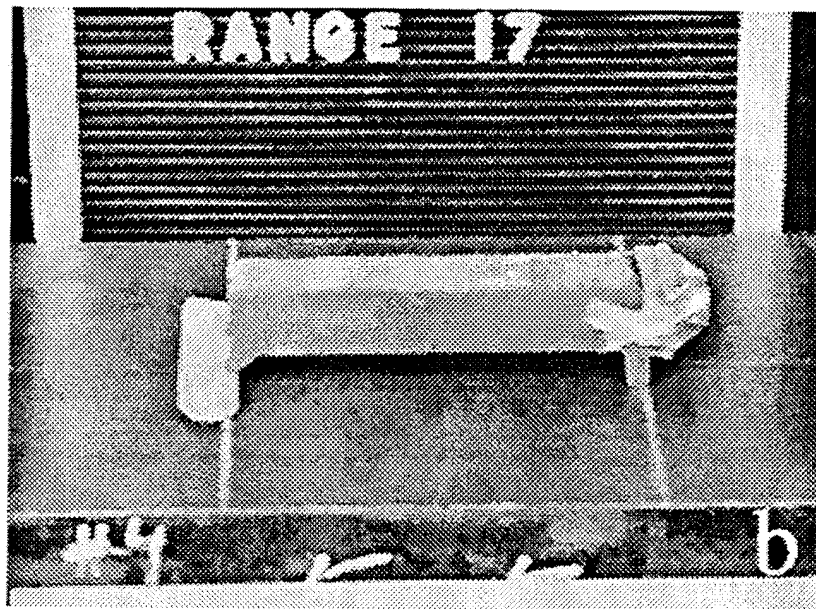
Figure 19. X-ray radiograph of LSC (axial view) at 73.5 μ s.

The total time delay thus ranges from 14 μ s to 17 μ s. The radiograph flash time occurred at 73.5 μ s so that the total travel time ranged from 56.5 μ s to 59.5 μ s. The distance traveled by the jet is estimated at 197.9 mm from the radiograph so that jet tip velocity is estimated to range from 3.3 km/s to 3.5 km/s.

3.3 LSC Jet Penetration Measurements. The penetration performance of the LSC into RHA plates that measure 450x200x51 mm is characterized using two test configurations. In the first test configuration (Figure 20a), the LSC has a nonuniform standoff distance in which the liner base makes an angle of about 8.6° with the surface of the RHA plate. In the second test configuration, shortening the long legs, and elevating the short legs of the LSC with wooden spacers (Figure 20b) creates a uniform standoff distance on the order of 12.7 mm. The Comp-B within the liner is detonated normal to its long axis by precursively detonating two, 5-mm thick Datasheet explosive wafers at one end of the charge; this same explosive initiation procedure was used in the free flight experiments. Figure 21 shows a plan view of the damaged RHA plate experiments from the nonuniform standoff test. A relatively straight narrow cut is seen, 10-mm wide at the center, and about 170-mm long. The cut in the RHA is



a



b

Figure 20. LSC test configurations, a) nonuniform, and b) uniform.

virtually the same in both the uniform and the nonuniform standoff test. A relatively straight narrow cut is seen, 10-mm wide at the center, and about 170-mm long. The cut in the RHA is virtually the same in both the uniform and nonuniform charge configurations. However, the jet penetrated to a depth of 18 mm in the nonuniform charge configuration, and to a depth of only 17 mm for the uniform charge configuration; the penetration measurements were made by sectioning the RHA plates normal to the long axis of symmetry of the cut, and then measuring the distance from the bottom surface of the plate to the

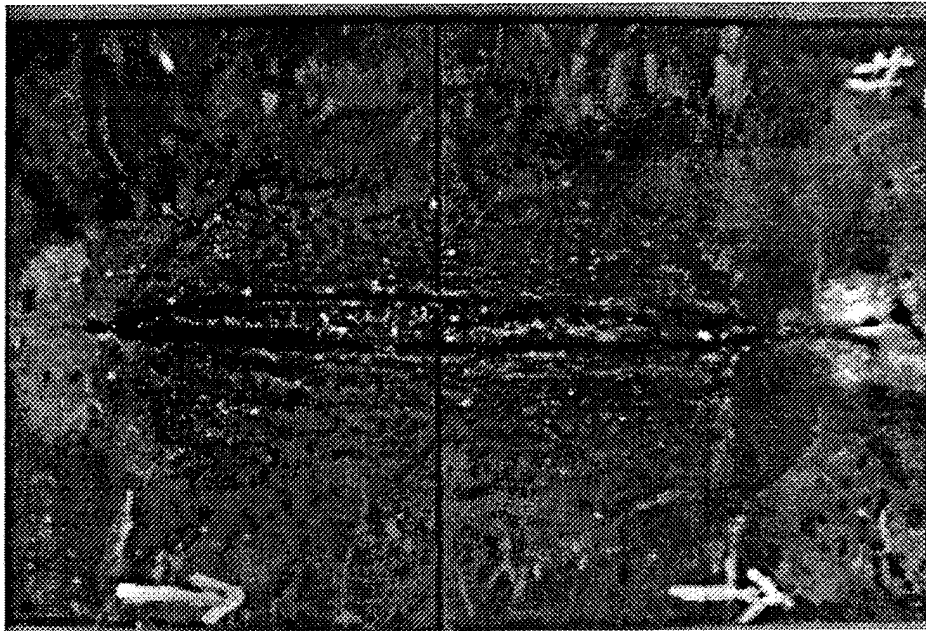


Figure 21. Damaged RHA plate (plan view) for nonuniform standoff test.
Detonation wave traveled from left to right (indicated by arrows).

bottom of the cut and subtracting this distance from the initial plate thickness of 51 mm. Figure 22a shows a closeup view of the sectioned plate for the nonuniform standoff test; residual liner material is visible at the base of each of the cuts. An experiment was also conducted using a 25.4-mm-thick mild steel target. The cut is wider (15 mm) in the mild steel plate than in the RHA plate. In addition, the jet nearly penetrated through the mild steel plate and caused it to bulge and crack longitudinally along the lower surface (Figure 22b). The 152-mm-long LSC creates a cut in the mild steel that is about the same length as the cut in the RHA (i.e., about 170 mm).

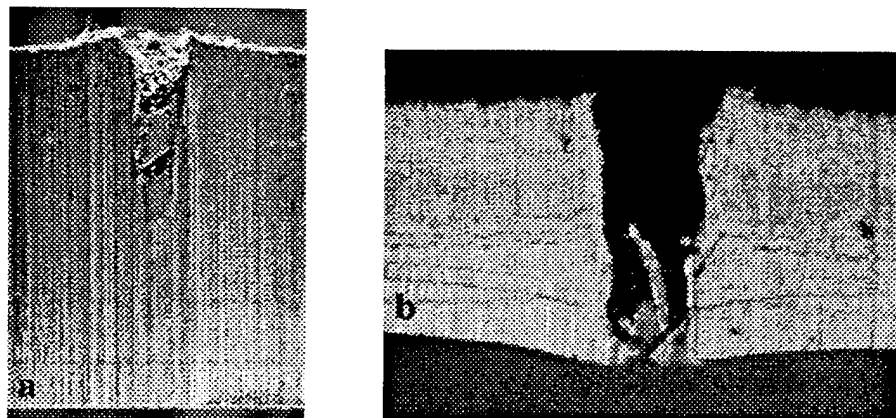


Figure 22. Cross sections through a) RHA plate 2-in (50.8 mm)-thick,
and b) Mild steel plate 1-in (25.4 mm)-thick.

4. COMPARISON OF COMPUTATIONS AND EXPERIMENTS

The hydrocode simulations predict a jet tip free flight velocity of about 5.2 km/s. However, observed jet tip free flight velocities of the LSC range from 3.3 to 3.5 km/s as determined from flash radiography, and 3.52 km/s using a special makewire circuit test fixture. Furthermore, the simulations predict a greater penetration depth of 22.9 mm, whereas penetration depths into two rectangular, 2-in-thick RHA plates measure about 17 and 18 mm respectively. The greater predicted plate penetration depth is expected since the predicted jet tip velocities were greater than those observed. We decided to rerun the *jet formation* problem by varying certain input parameters in an attempt to reduce the predicted jet tip velocity. The following additional simulations were conducted, yet all were relatively unsuccessful in significantly decreasing the jet velocity; a synopsis of these results appears as snapshots of the jet velocity versus axial position at 4 μ s and 12 μ s for each of the following conditions:

- (1) Original liner mesh density with element erosion = 0.0 (Figure 23a).
- (2) A mesh density increase through the liner thickness by a factor of two (dense mesh) (Figure 23b).
- (3) A dense mesh with a flat inner liner mesh geometry (Figure 23c).
- (4) A modified dense mesh with a flat inner liner mesh geometry and apex angle = 82° (Figure 23d).

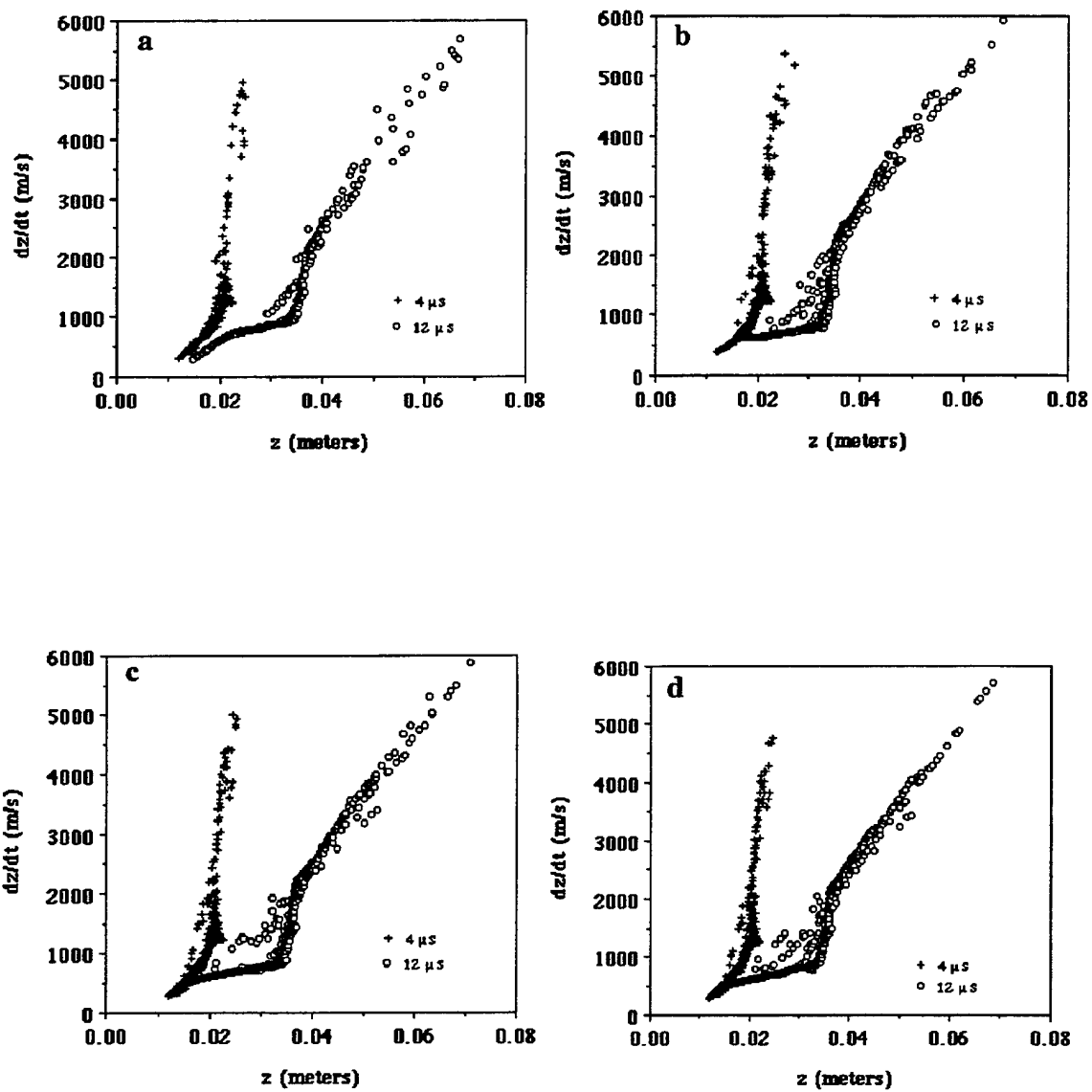


Figure 23. Jet velocity versus axial position at 4 μ s and 12 μ s. a) Original liner with element erosion = 0.0, b) Dense mesh, c) Dense mesh with flat liner, d) Modified dense mesh, flat inner liner with apex angle = 82 $^{\circ}$.

Magnified views in the vicinity of the liner apex of both the dense mesh, and the modified dense mesh at 0 μ s and 4 μ s appear in Figures 24 and 25, respectively. The effect of increasing the finite element density in the liner is to increase the jet velocity (e.g., compare maximum jet tip velocity in Figures 23b, c, and d with that in Figure 23a) rather than to decrease jet velocity; similar spatial resolution effects are reported in Walters and Zukas (1989) in some EPIC lead hemispherical liner computations. The Walters and Zukas (1989) computations predict jet tip velocities to within 5.3% of the experimentally measured velocities, yet our computations overpredict the jet tip velocity by 33%. The good agreement between the predicted and experimental results of Walters and Zukas (1989) could be a result of the smoothly varying surface geometry of the hemispherical liner. Altering the LSC liner geometry from v-notch to flat, however, only slightly reduced the maximum jet tip velocity (e.g., compare maximum jet tip velocity in Figure 23b with that in Figure 23c).

We also attempted to rezone the liner at 2 μ s, since the triangular elements in the jet tip become highly distorted and may artificially affect mesh stiffness and hence nodal displacements and velocities. We were unsuccessful in using the EPIC92 rezoner. We also hypothesized that in the fully 3-D problem, a pressure-release wave might closely follow the detonation wave as it travels along the axis of the LSC; the pressure-release wave would have the effect of reducing the total momentum transferred to the liner and thus decrease the jet tip velocity. The pressure-release phenomenon might affect the computational results for our 2-D plane strain model, so several simulations were also conducted, whereby the explosive material was dropped from the analysis at 4 μ s, 6 μ s, and 8 μ s (effectively modeling the pressure release phenomenon); dropping the explosive material at these times did not appreciably decrease the jet tip velocities. Finally, we reran the problem using the EPIC94 version of the hydrocode which has an automatic mesh rezone feature. This attempt provided successful computations to 4 μ s with the original mesh density. The jet tip velocity was reduced from 4.7 km/s at 4 μ s in the original problem (see Figure 23a) to 3.8 km/s in the rezoned problem at 4 μ s (Figure 26b). We were unable to obtain results beyond 4 μ s because of numerical instabilities associated with requiring a vanishingly small integration time increment as a result of an equation-of-state instability. It is interesting to note that these numerical instabilities were not encountered when the problem was initially run without rezoning. Unstable numerical behavior was also encountered when we doubled the mesh density and used the EPIC94 automatic rezoner.

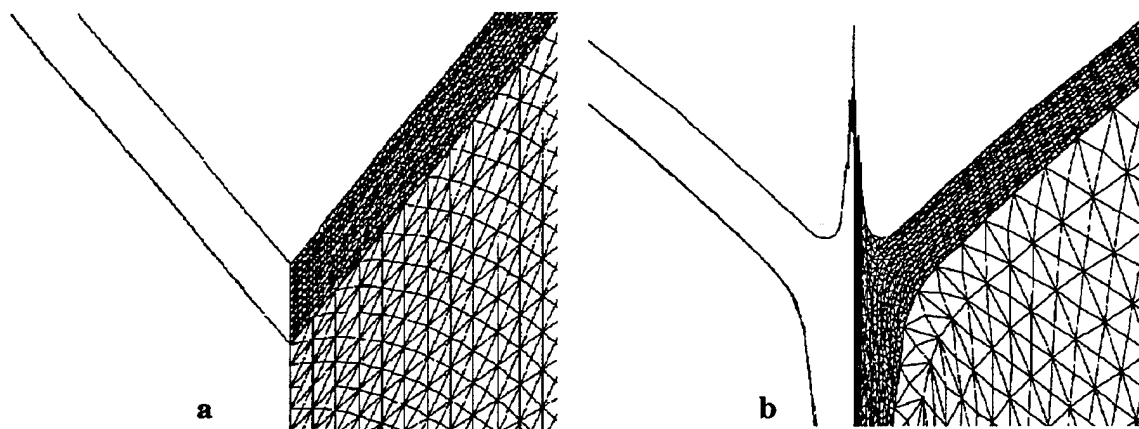


Figure 24. Computational mesh (magnified) for the dense liner in the vicinity of the liner apex at: a) $t = 0 \mu\text{s}$, and b) $t = 4 \mu\text{s}$.

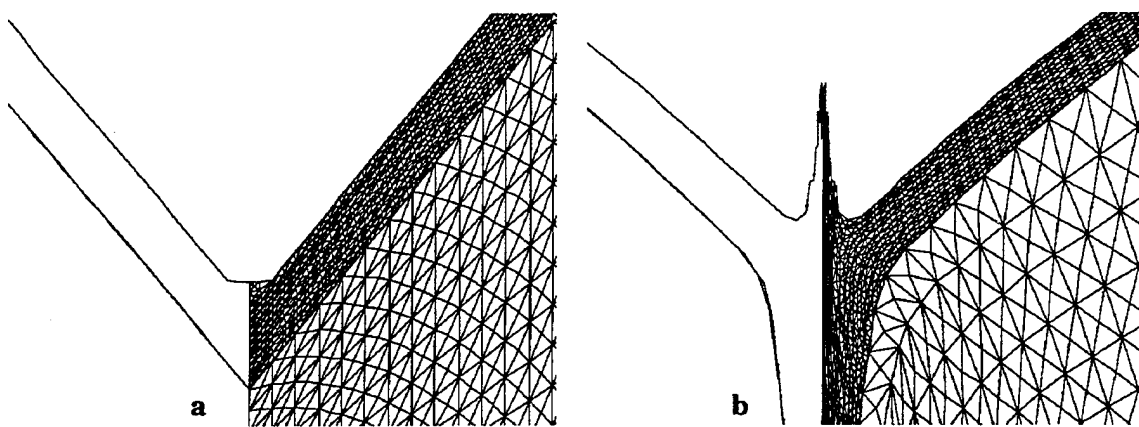


Figure 25. Computational mesh (magnified) for the modified dense mesh in the vicinity of the liner apex at: a) $t = 0 \mu\text{s}$, and b) $t = 4 \mu\text{s}$.

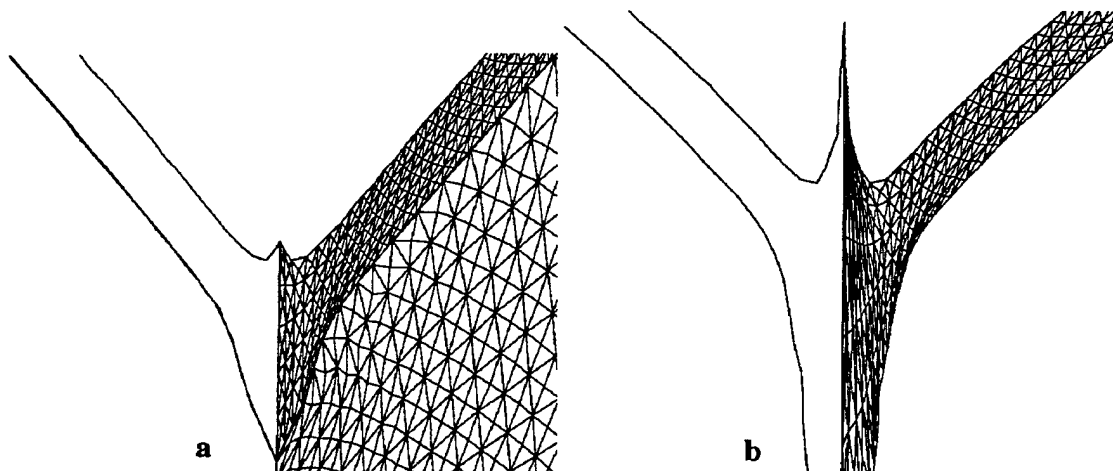


Figure 26. Computational mesh (magnified) rezoned at: a) $t = 2 \mu\text{s}$, and b) $t = 4 \mu\text{s}$.

5. CONCLUSIONS

- (1) Lagrangian hydrocode computations in 2-D plane strain using EPIC92 predict an early time jet tip velocity of 5.2 km/s at 12 μ s for the Mk-7 Mod 8 demolition charge; this result greatly overpredicts the observed later time jet tip free flight velocities which range from 3.3 to 3.5 km/s at nearly 60 μ s using flash radiography, and 3.52 km/s averaged from 20 μ s to 60 μ s using an electrical makewire circuit.
- (2) Jet tip velocity was not constant in the simulation, rising from 4.7 km/s at 4 μ s to 5.2 km/s at 12 μ s. After the jet has formed, such accelerations are nonphysical, based upon our understanding of the jet formation process, and likely result from the overly stiff nature of the constant strain triangles used to simulate the jet formation process.
- (3) Parametric attempts to reduce the jet tip velocity prediction by: a) eliminating jet erosion (i.e., setting the element erosion feature = 0.0), b) doubling liner mesh density, c) flattening the liner apex angle, and d) increasing the liner apex angle from 80° to 82°, were unsuccessful.
- (4) Use of the automatic rezone feature in the EPIC94 version of the hydrocode resulted in a reduction of the jet tip velocity from 4.7 km/s to 3.8 km/s at 4 μ s in the coarse mesh. The computations thus overpredict the observed jet tip velocity by 8 % if one assumes a constant velocity jet. Computations beyond 4 μ s were not possible due to numerical instabilities associated with requiring a vanishingly small integration time increment resulting from an equation-of-state instability. This behavior was also observed in the denser mesh. We were unsuccessful in utilizing the *manual* EPIC92 rezoner.
- (5) Penetration depths into two rectangular, 2-in (50.8 mm)-thick RHA plates measured 17 and 18 mm respectively, whereas the hydrocode simulation predicted a greater penetration depth of 22.9 mm. The overprediction in the computed penetration depth is expected since jet tip velocities were also overpredicted by the hydrocode. The work attests to the importance of conducting experiments in order to verify baseline hydrocode simulations.

6. REFERENCES

- Asay, B. W., J. B. Ramsay, M. U. Anderson, and R. A. Graham. "Shock Response of the Commercial High Explosive Datasheet." Shock Waves, vol. 3, pp. 267-271, 1994.
- Cook, W. H., A. M. Rajendran, and D. J. Grove. "An Efficient Numerical Implementation of the Bodner-Partom Model in the EPIC-1 Code." Engineering Fracture Mechanics, vol. 41, no. 5, pp. 607-623, 1992.
- Department of the Navy EODB/Department of the Army TM/U.S. Air Force TO 60A-2-1-51. Explosive Ordnance Disposal Procedures. Shaped Charges: General Information, September 1992.
- Johnson, G. R. "High Velocity Impact Calculations in Three Dimensions." Journal of Applied Mechanics, vol. 99, no. 1, pp. 95-100, 1977.
- Johnson, G. R. "Short Presentation by G. R. Johnson." Theoretical Foundation for Large-Scale Computations of Nonlinear Material Behavior. Edited by S. Nemat Nasser et al. Boston: Martinus Nijhoff Publishers, 1984.
- Johnson, G. R., and W. H. Cook. "Fracture Characteristics of Three Metals Subjected to Various Strains, Strain Rates, Temperatures, and Pressures." Engineering Fracture Mechanics, vol. 21, no. 1, pp. 31-48, 1985.
- Johnson, G. R., R. A. Stryk, D. E. Pratt, and J. A. Schonhardt. EPIC Hydrocode User's Workshop. Alliant Techsystems, Inc., Brooklyn Park, MN, October 1992a.
- Johnson, G. R., R. A. Stryk, D. E. Pratt, and J. A. Schonhardt. User Instructions for the 1992 Version of the EPIC Code. Alliant Techsystems, Inc., Brooklyn Park, MN, October 1992b.
- Raftenberg, M. N. "Lagrangian Hydrocode Simulations of Rolled-Homogeneous-Armor Plate Perforation by a Shaped Charge Jet." International Journal of Impact Engineering, vol. 15, no. 5, pp. 619-643, 1994.
- Walters, W. P., and J. A. Zukas. Fundamentals of Shaped Charges. New York: John Wiley and Sons, 1989.

INTENTIONALLY LEFT BLANK.

APPENDIX A:
SHAPED CHARGE JET FORMATION
INPUT DECK AND COMPUTATIONAL RESULTS

INTENTIONALLY LEFT BLANK.


```

$.sys.nplt.lplt.dplt.....dtsys.....tsys....dtnode.....tnode.....dtdyn.....tdyn
    1      0           1.0e-6       0.0     0.25e-6       0.0

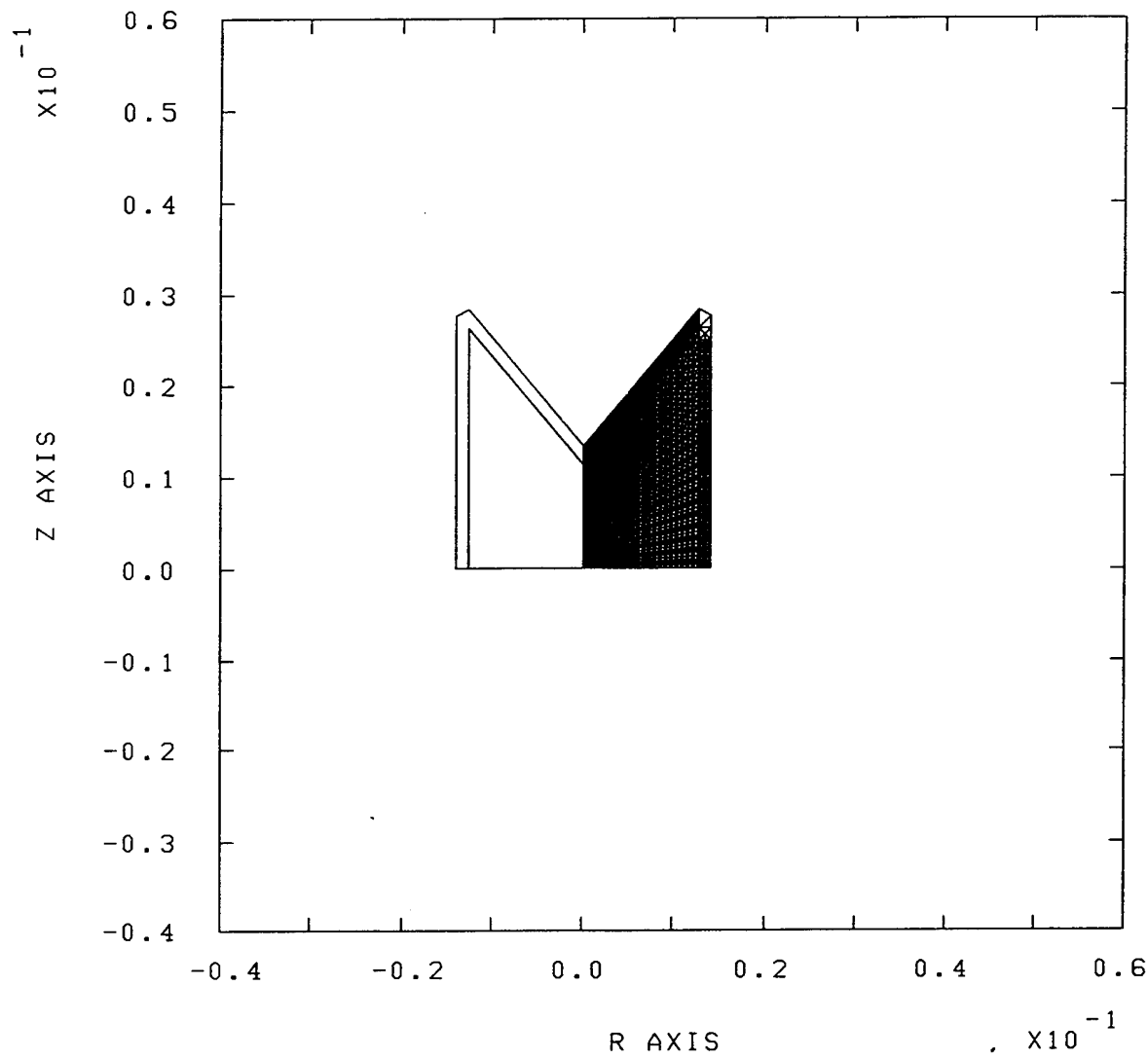
$type.case.....problem description.....]
    3      1 NEOD Linear Shaped Charge - S. Segletes & George Gazonas - NOV 1993
$
$ This restart run will start at 0 us and continue to 12 microseconds
$
$$ main run data ****
$cycl.ncpu.....time.....dtmax.....dtmin.....ssf.....tmax.....cpmax.....emax
    0      0 0000.0e-6      1.0      0.1e-9      0.80    12.0e-6   10800.00
$tplt.drop..add.pres.push..hrg....vfract....vnref...nabfact...sphdist/////////
    1      0      0      0      0      0
$.sys.nplt.lplt.dplt.....dtsys.....tsys....dtnode.....tnode.....dtdyn.....tdyn
    1      0           1.0e-6       0.0     0.25e-6       0.0
$.....time....echeck....ncheck....rdamp.save.burn.yprt.ndat.slpr.proj..pat.rzne
 02.0E-06    1001.0      999      0.0      3      0      1    500      2      0      0      0
 04.0E-06    1001.0      999      0.0      3      0      1    500      2      0      0      0
 06.0E-06    1001.0      999      0.0      3      0      1    500      2      0      0      0
 08.0E-06    1001.0      999      0.0      3      0      1    500      2      0      0      0
 10.0E-06   1001.0      999      0.0      3      0      1    500      2      0      0      0
 999.0E-06   1001.0      999      0.0      3      0      1    500      2      0      0      0

$type.case.....problem description.....]
    3      1 NEOD Linear Shaped Charge - S. Segletes & George Gazonas - NOV 1993
$
$ This restart run will restart at 12 us and then drop the explosive and
$ casing at 12.1 microseconds, continuing on until 20 microseconds.
$
$$ main run data ****
$cycl.ncpu.....time.....dtmax.....dtmin.....ssf.....tmax.....cpmax.....emax
    0      0 0012.0e-6      1.0      0.1e-9      0.80    20.0e-6   10800.00
$tplt.drop..add.pres.push..hrg....vfract....vnref...nabfact...sphdist/////////
    1      1      0      0      0      0
$.sys.nplt.lplt.dplt.....dtsys.....tsys....dtnode.....tnode.....dtdyn.....tdyn
    1      0           1.0e-6       0.0     0.25e-6       0.0
$.....tdrop.nnod.nnab.nele.nsld.nríg.nchk.load.nzon.nplt.lplt**RYZ.nfal****..per
 0012.1e-6   446      0    800      0      0      0      0      0      0    100      20      0
$.ef1..ef2..ef3..ef4..ef5..ef6..ef7..ef8..ef9..ef10..ef11..ef12..ef13..ef14..ef15..ef16
    1      2      3      4      5      6      7      8      9      10      11      12      13      14      15      16
$ef17..ef18..ef19..ef20
    17     18     19     20
$.....time....echeck....ncheck....rdamp.save.burn.yprt.ndat.slpr.proj..pat.rzne
 14.0E-06    1001.0      999      0.0      3      0      1    500      2      0      0      0
 16.0E-06    1001.0      999      0.0      3      0      1    500      2      0      0      0
 18.0E-06    1001.0      999      0.0      3      0      1    500      2      0      0      0
 21.0E-06    1001.0      999      0.0      3      0      1    500      2      0      0      0

```

EPIC POST PROCESSOR, POST1 (1992-2) 15:59:04 09-Dec-93
2-D PLANE STRAIN GEOMETRY

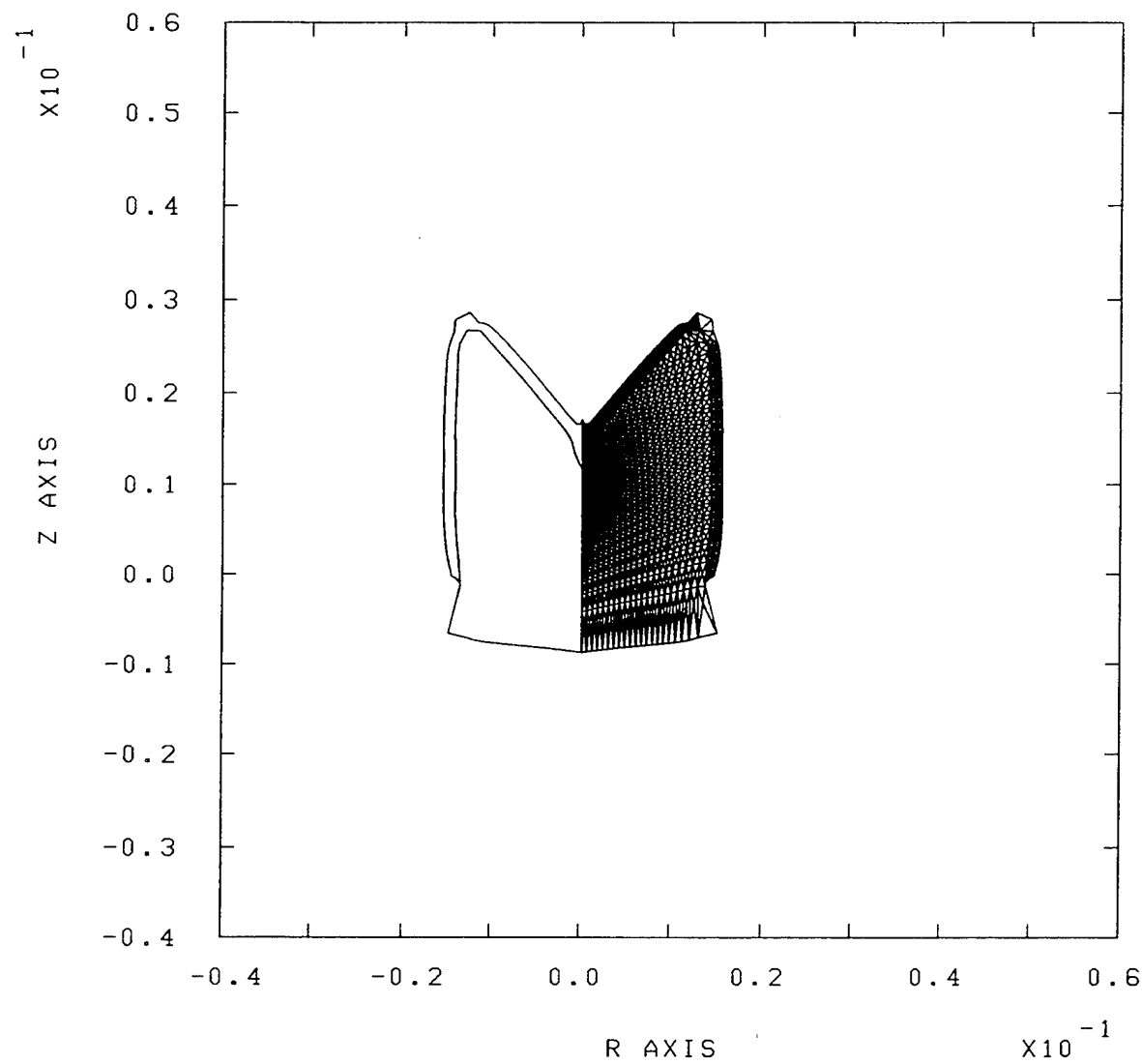
Linear SC Formation ; CASE = 1; TIME = 0.0000000; CYCLE = 0



EPIC POST PROCESSOR, POST1 (1992-2) 16:00:17 09-Dec-93
2-D PLANE STRAIN GEOMETRY

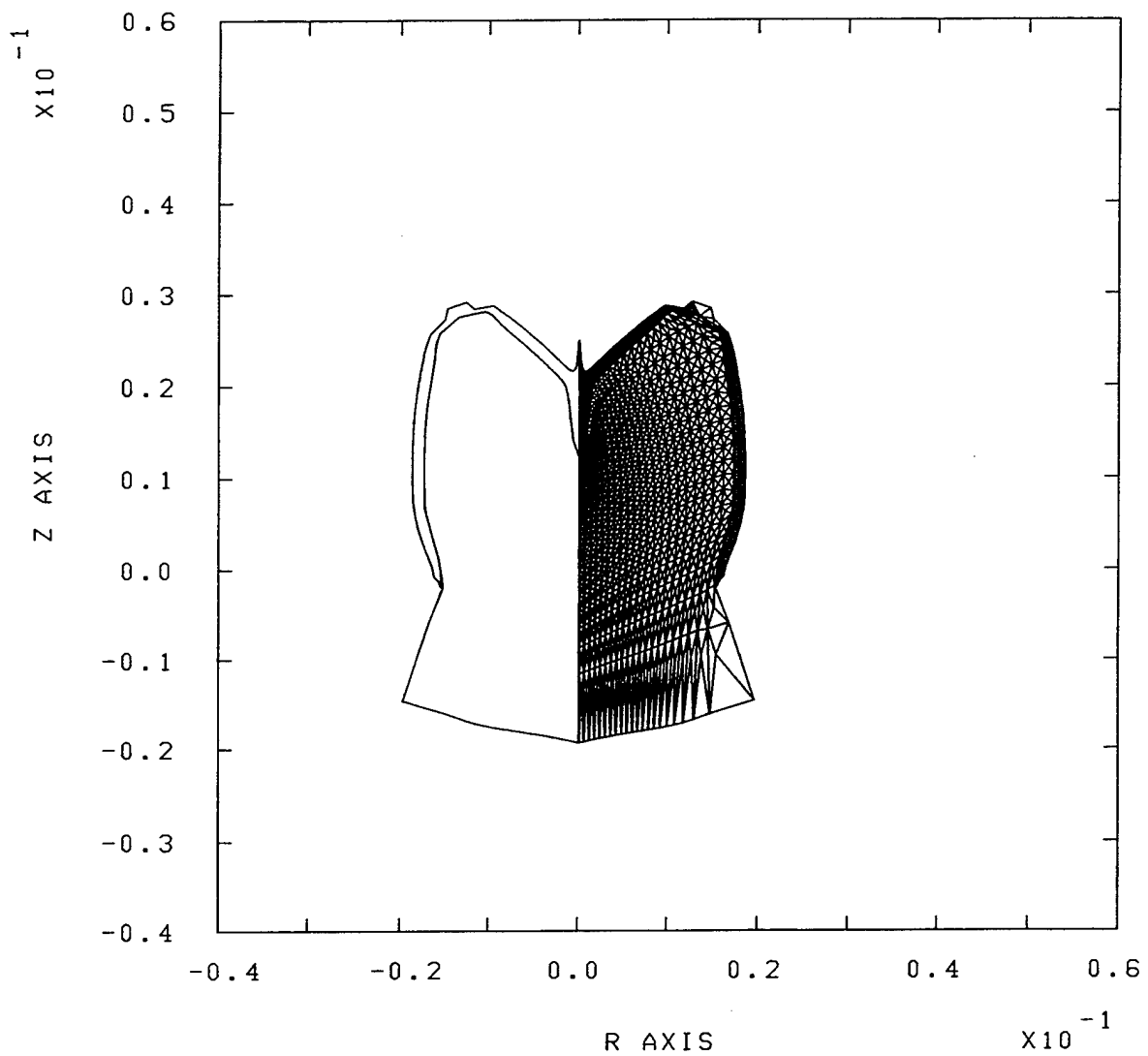
Linear SC Formation

; CASE = 1; TIME = 0.00000200; CYCLE = 374



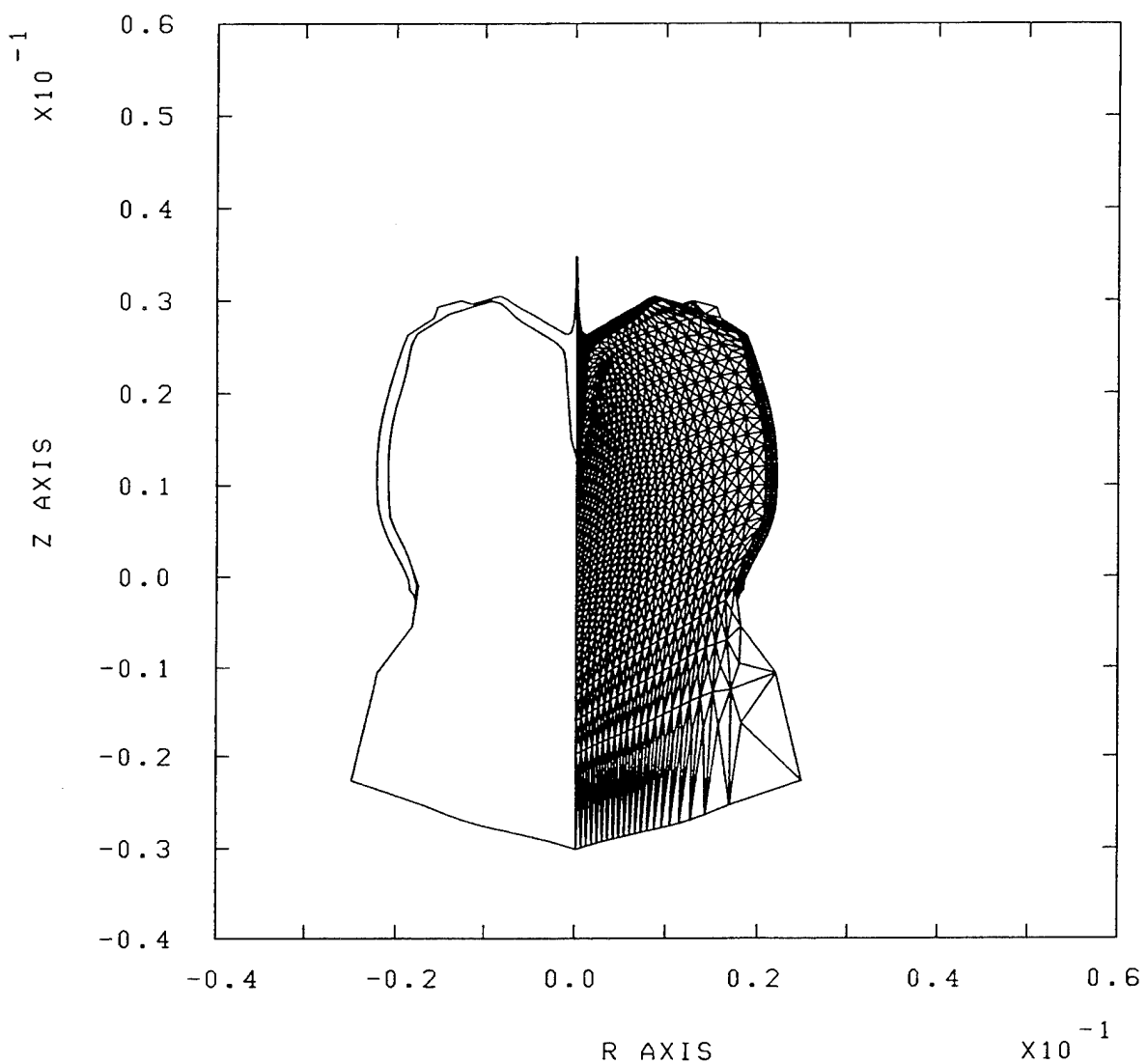
EPIC POST PROCESSOR, POST1 (1992-2) 16:00:21 09-Dec-93
2-D PLANE STRAIN GEOMETRY

Linear SC Formation ; CASE = 1; TIME = 0.00000400; CYCLE = 1937



EPIC POST PROCESSOR, POST1 (1992-2) 16:00:25 09-Dec-93
2-D PLANE STRAIN GEOMETRY

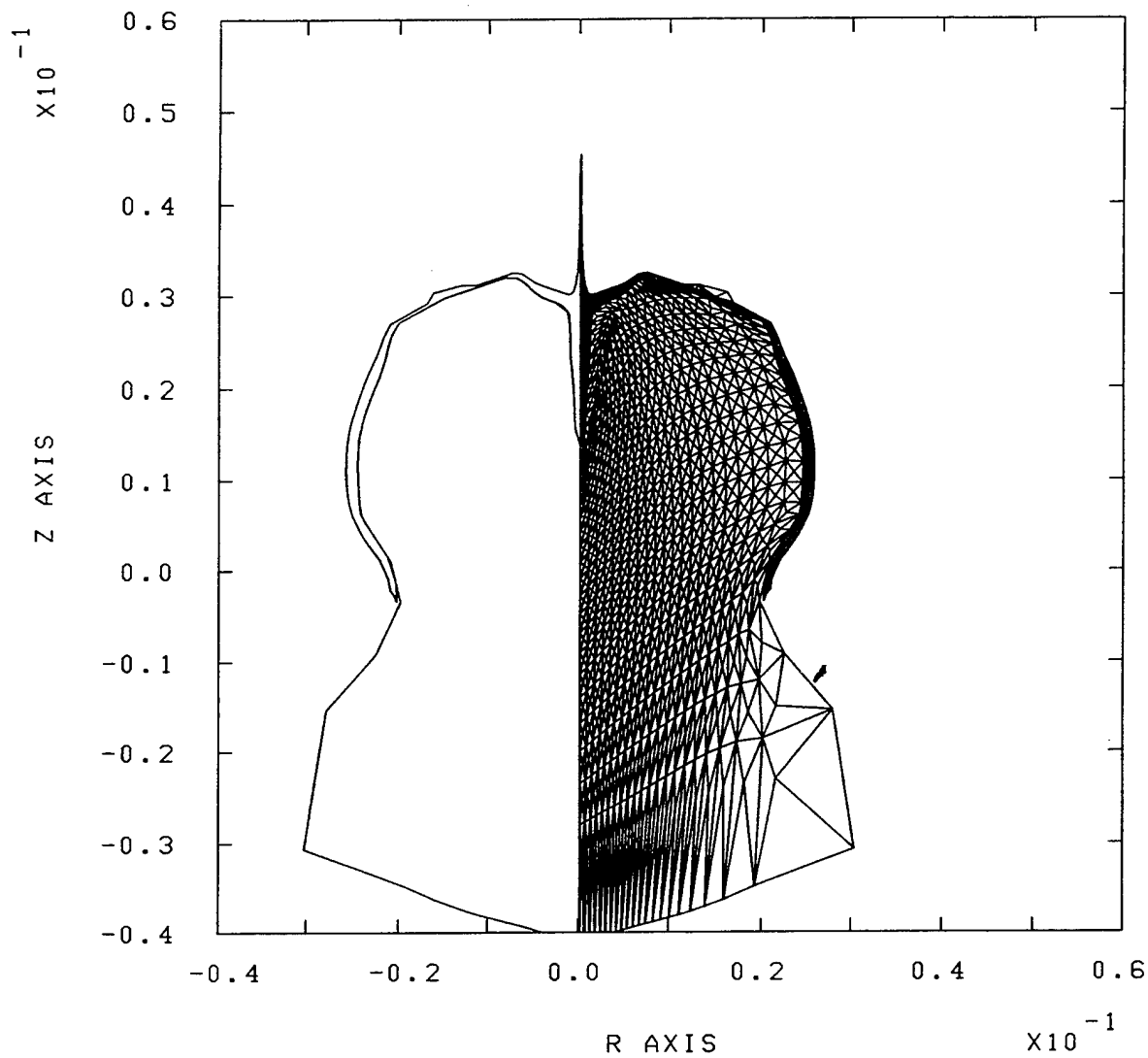
Linear SC Formation ; CASE = 1; TIME = 0.00000600; CYCLE = 5027



EPIC POST PROCESSOR, POST1 (1992-2) 16:00:29 09-Dec-93
2-D PLANE STRAIN GEOMETRY

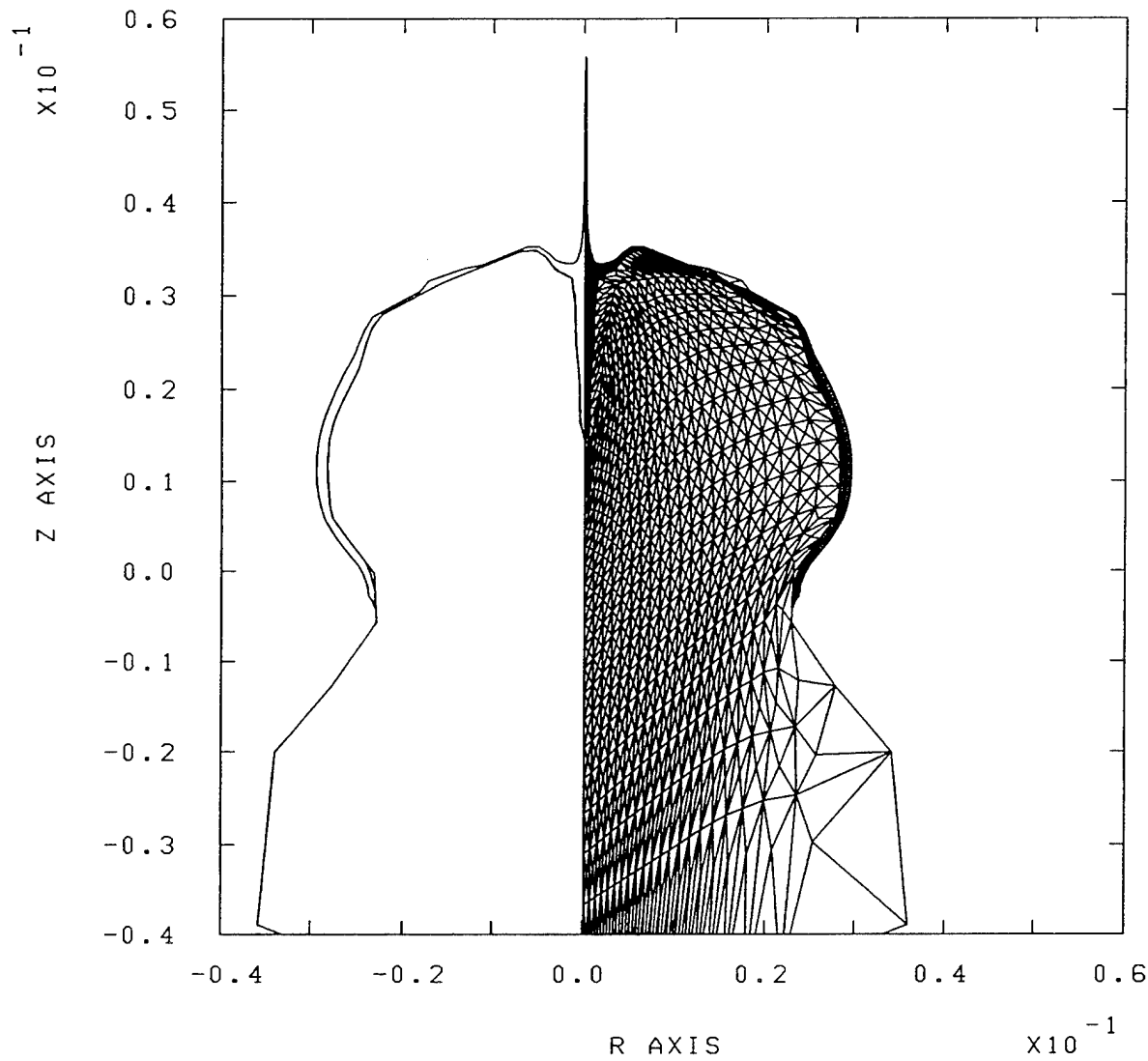
Linear SC Formation

; CASE = 1; TIME = 0.00000800; CYCLE = 9690



EPIC POST PROCESSOR, POST1 (1992-2) 16:00:32 09-Dec-93
2-D PLANE STRAIN GEOMETRY

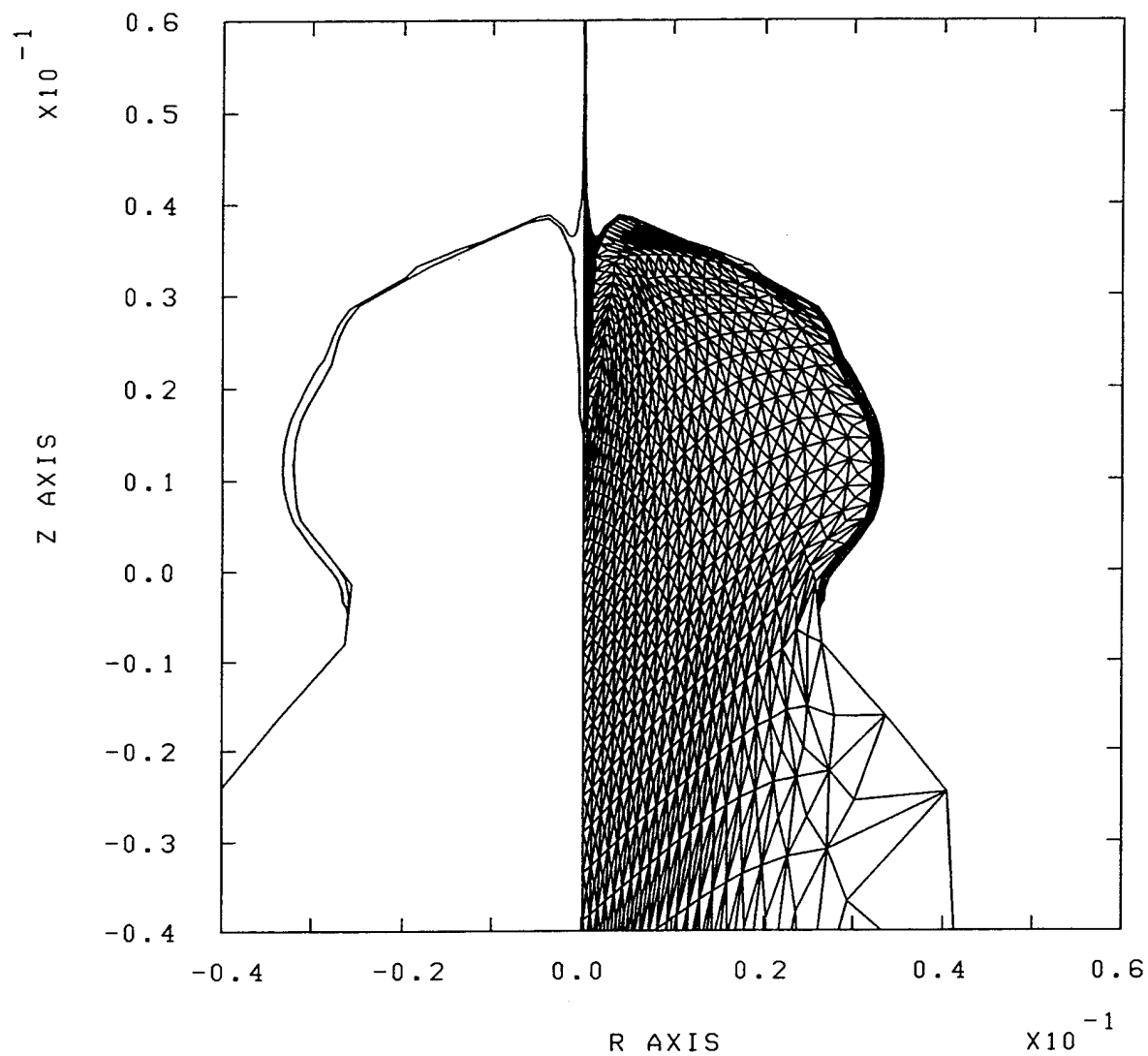
Linear SC Formation : CASE = 1; TIME = 0.00001000; CYCLE = 15948



EPIC POST PROCESSOR, POST1 (1992-2) 16:00:36 09-Dec-93
2-D PLANE STRAIN GEOMETRY

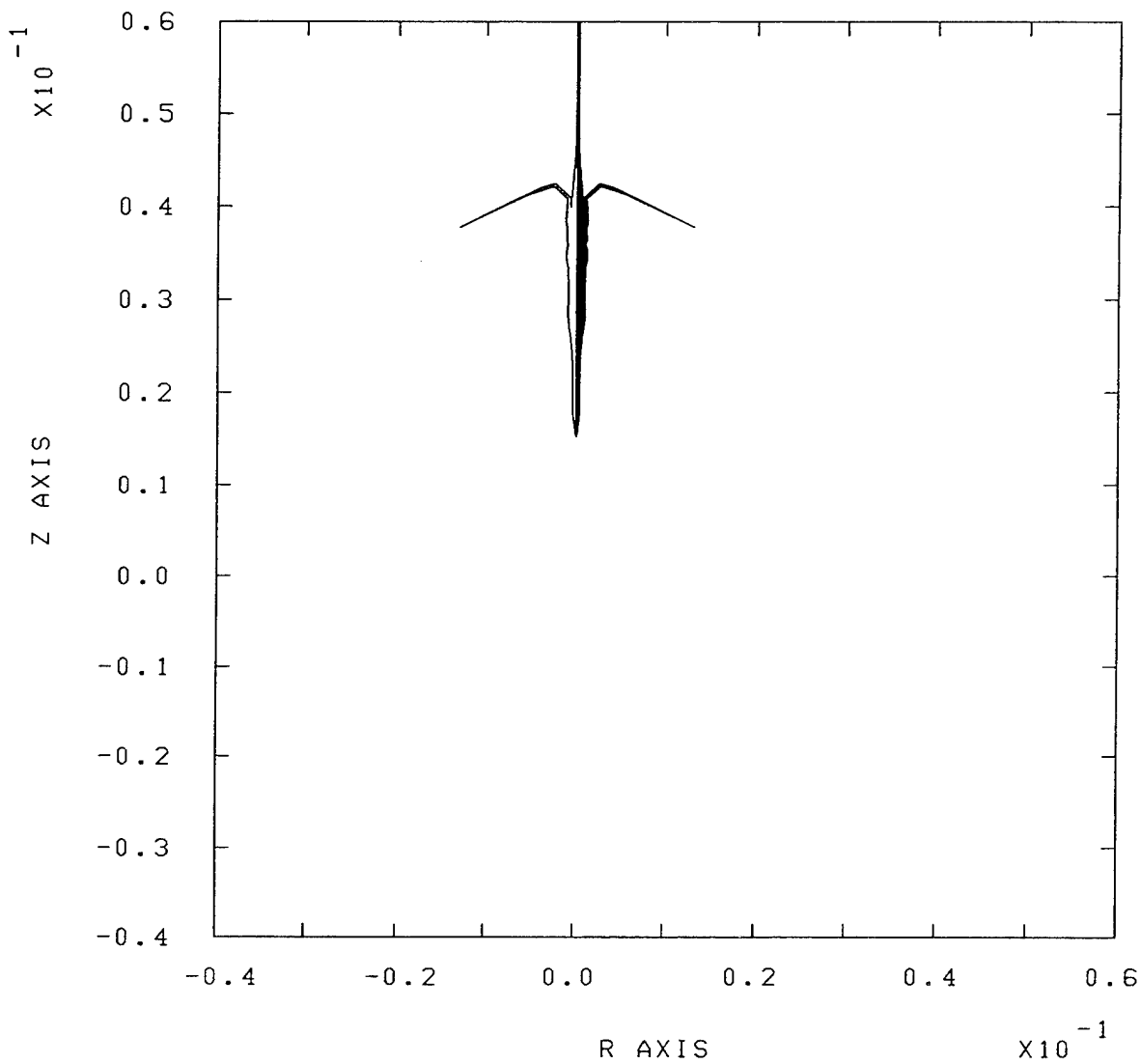
Linear SC Formation

; CASE = 1; TIME = 0.00001200; CYCLE = 23942



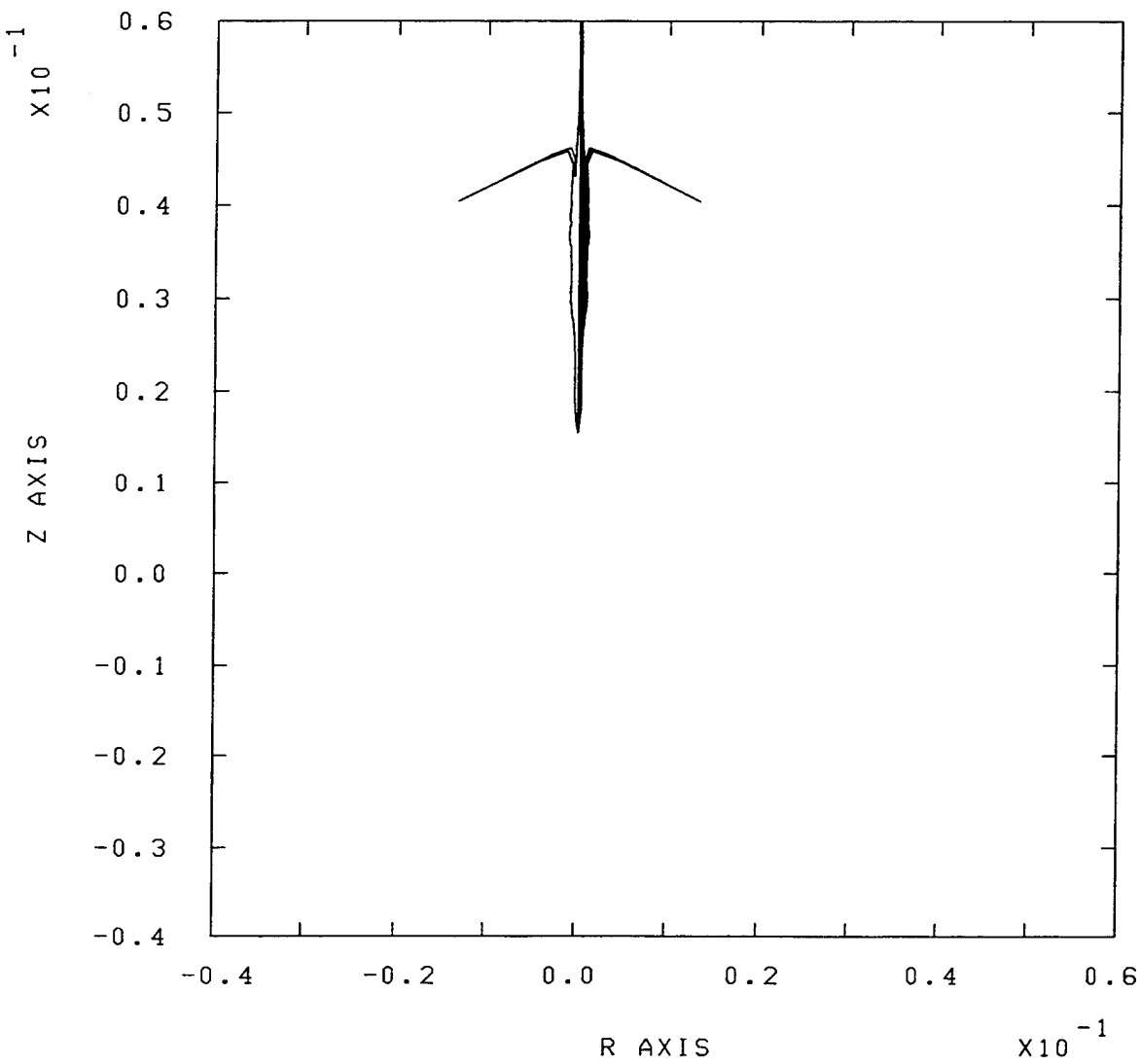
EPIC POST PROCESSOR, POST1 (1992-2) 16:00:39 09-Dec-93
2-D PLANE STRAIN GEOMETRY

Linear SC Formation ; CASE = 1; TIME = 0.00001400; CYCLE = 33746



EPIC POST PROCESSOR, POST1 (1992-2) 16:00:42 09-Dec-93
2-D PLANE STRAIN GEOMETRY

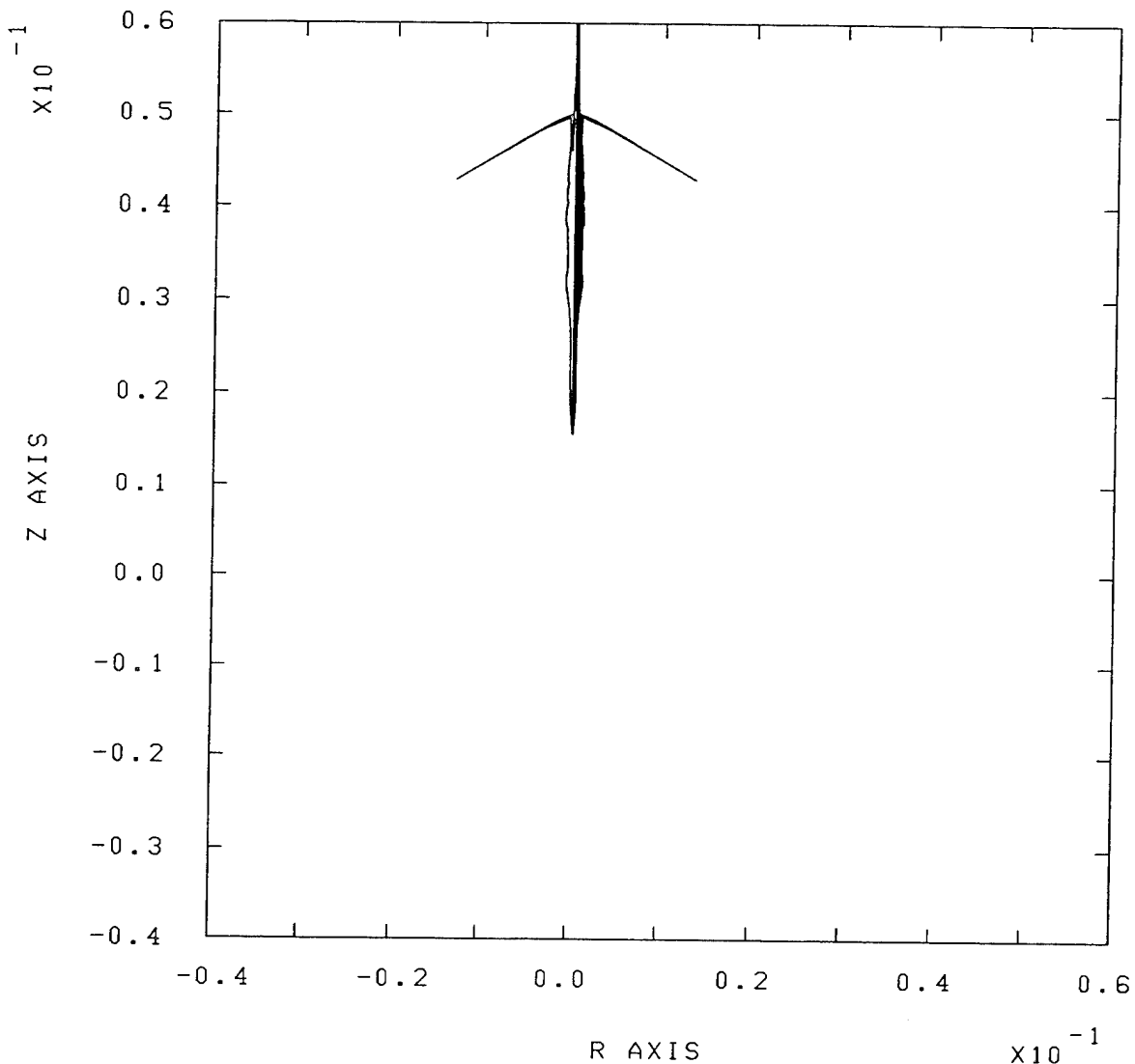
Linear SC Formation ; CASE = 1; TIME = 0.00001600; CYCLE = 45319



EPIC POST PROCESSOR, POST1 (1992-2) 16:00:46 09-Dec-93
2-D PLANE STRAIN GEOMETRY

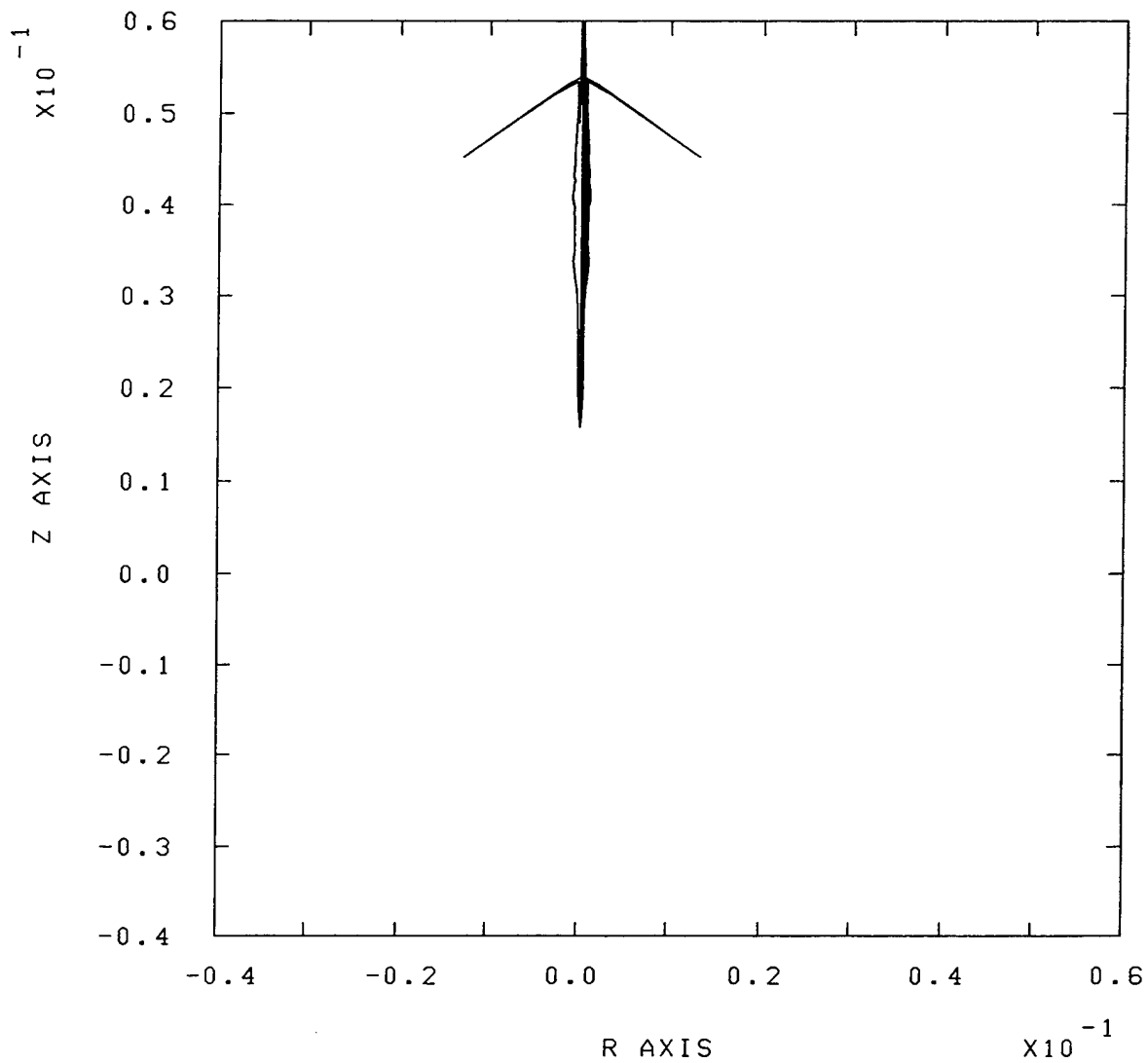
Linear SC Formation

; CASE = 1; TIME = 0.00001800; CYCLE = 58707



EPIC POST PROCESSOR, POST1 (1992-2) 16:00:49 09-Dec-93
2-D PLANE STRAIN GEOMETRY

Linear SC Formation ; CASE = 1; TIME = 0.00002000; CYCLE = 73975



INTENTIONALLY LEFT BLANK.

APPENDIX B:
SHAPED CHARGE JET PENETRATION
INPUT DECK AND COMPUTATIONAL RESULTS

INTENTIONALLY LEFT BLANK.

3.833E-02 3.837E-02 3.841E-02 3.845E-02 3.849E-02 3.853E-02 3.857E-02 3.861E-02
 3.865E-02 3.869E-02 3.873E-02 3.877E-02 3.881E-02 3.885E-02 3.889E-02 3.893E-02
 3.897E-02 3.901E-02 3.905E-02 3.909E-02 3.913E-02 3.917E-02 3.921E-02 3.925E-02
 3.929E-02 3.933E-02 3.937E-02 3.941E-02 3.945E-02 3.949E-02 3.953E-02 3.957E-02
 3.961E-02 3.965E-02 3.969E-02 3.973E-02 3.977E-02 3.981E-02 3.985E-02 3.989E-02
 3.993E-02 3.997E-02 4.001E-02 4.005E-02 4.009E-02 4.013E-02 4.017E-02 4.021E-02
 4.025E-02 4.029E-02 4.033E-02 4.037E-02 4.041E-02 4.045E-02 4.049E-02 4.053E-02
 4.057E-02 4.061E-02 4.065E-02 4.069E-02 4.073E-02 4.077E-02 4.081E-02
 \$RAD=2.RB1.....RB2.....RB3.....RB4.....RB5.....RB6.....RB7.....RB8
 2.841E-02 2.845E-02 2.849E-02 2.853E-02 2.857E-02 2.861E-02 2.865E-02 2.869E-02
 2.873E-02 2.877E-02 2.881E-02 2.885E-02 2.889E-02 2.893E-02 2.897E-02 2.901E-02
 2.905E-02 2.909E-02 2.913E-02 2.917E-02 2.921E-02 2.925E-02 2.929E-02 2.933E-02
 2.937E-02 2.941E-02 2.945E-02 2.949E-02 2.953E-02 2.957E-02 2.961E-02 2.965E-02
 2.969E-02 2.973E-02 2.977E-02 2.981E-02 2.985E-02 2.989E-02 2.993E-02 2.997E-02
 3.001E-02 3.005E-02 3.009E-02 3.013E-02 3.017E-02 3.021E-02 3.025E-02 3.029E-02
 3.033E-02 3.037E-02 3.041E-02 3.045E-02 3.049E-02 3.053E-02 3.057E-02 3.061E-02
 3.065E-02 3.069E-02 3.073E-02 3.077E-02 3.081E-02 3.085E-02 3.089E-02 3.093E-02
 3.097E-02 3.101E-02 3.105E-02 3.109E-02 3.113E-02 3.117E-02 3.121E-02 3.125E-02
 3.129E-02 3.133E-02 3.137E-02 3.141E-02 3.145E-02 3.149E-02 3.153E-02 3.157E-02
 3.161E-02 3.165E-02 3.169E-02 3.173E-02 3.177E-02 3.181E-02 3.185E-02 3.189E-02
 3.193E-02 3.197E-02 3.201E-02 3.205E-02 3.209E-02 3.213E-02 3.217E-02 3.221E-02
 3.225E-02 3.229E-02 3.233E-02 3.237E-02 3.241E-02 3.245E-02 3.249E-02 3.253E-02
 3.257E-02 3.261E-02 3.265E-02 3.269E-02 3.273E-02 3.277E-02 3.281E-02 3.285E-02
 3.289E-02 3.293E-02 3.297E-02 3.301E-02 3.305E-02 3.309E-02 3.313E-02 3.317E-02
 3.321E-02 3.325E-02 3.329E-02 3.333E-02 3.337E-02 3.341E-02 3.345E-02 3.349E-02
 3.353E-02 3.357E-02 3.361E-02 3.365E-02 3.369E-02 3.373E-02 3.377E-02 3.381E-02
 3.385E-02 3.389E-02 3.393E-02 3.397E-02 3.401E-02 3.405E-02 3.409E-02 3.413E-02
 3.417E-02 3.421E-02 3.425E-02 3.429E-02 3.433E-02 3.437E-02 3.441E-02 3.445E-02
 3.449E-02 3.453E-02 3.457E-02 3.461E-02 3.465E-02 3.469E-02 3.473E-02 3.477E-02
 3.481E-02 3.485E-02 3.489E-02 3.493E-02 3.497E-02 3.501E-02 3.505E-02 3.509E-02
 3.513E-02 3.517E-02 3.521E-02 3.525E-02 3.529E-02 3.533E-02 3.537E-02 3.541E-02
 3.545E-02 3.549E-02 3.553E-02 3.557E-02 3.561E-02 3.565E-02 3.569E-02 3.573E-02
 3.577E-02 3.581E-02 3.585E-02 3.589E-02 3.593E-02 3.597E-02 3.601E-02 3.605E-02
 3.609E-02 3.613E-02 3.617E-02 3.621E-02 3.625E-02 3.629E-02 3.633E-02 3.637E-02
 3.641E-02 3.645E-02 3.649E-02 3.653E-02 3.657E-02 3.661E-02 3.665E-02 3.669E-02
 3.673E-02 3.677E-02 3.681E-02 3.685E-02 3.689E-02 3.693E-02 3.697E-02 3.701E-02
 3.705E-02 3.709E-02 3.713E-02 3.717E-02 3.721E-02 3.725E-02 3.729E-02 3.733E-02
 3.737E-02 3.741E-02 3.745E-02 3.749E-02 3.753E-02 3.757E-02 3.761E-02 3.765E-02
 3.769E-02 3.773E-02 3.777E-02 3.781E-02 3.785E-02 3.789E-02 3.793E-02 3.797E-02
 3.801E-02 3.805E-02 3.809E-02 3.813E-02 3.817E-02 3.821E-02 3.825E-02 3.829E-02
 3.833E-02 3.837E-02 3.841E-02 3.845E-02 3.849E-02 3.853E-02 3.857E-02 3.861E-02
 3.865E-02 3.869E-02 3.873E-02 3.877E-02 3.881E-02 3.885E-02 3.889E-02 3.893E-02
 3.897E-02 3.901E-02 3.905E-02 3.909E-02 3.913E-02 3.917E-02 3.921E-02 3.925E-02
 3.929E-02 3.933E-02 3.937E-02 3.941E-02 3.945E-02 3.949E-02 3.953E-02 3.957E-02
 3.961E-02 3.965E-02 3.969E-02 3.973E-02 3.977E-02 3.981E-02 3.985E-02 3.989E-02
 3.993E-02 3.997E-02 4.001E-02 4.005E-02 4.009E-02 4.013E-02 4.017E-02 4.021E-02
 4.025E-02 4.029E-02 4.033E-02 4.037E-02 4.041E-02 4.045E-02 4.049E-02 4.053E-02
 4.057E-02 4.061E-02 4.065E-02 4.069E-02 4.073E-02 4.077E-02 4.081E-02
 \$SAX=2..ZT1.....ZT2.....ZT3.....ZT4.....ZT5.....ZT6.....ZT7.....ZT8
 0. 0. 0. 0. 0. 0. 0. 0.
 0. 0. 0. 0. 0. 0. 0. 0.
 0. 0. 0. 0. 0. 0. 0. 0.
 0. 0. 0. 0. 0. 0. 0. 0.
 0. 0. 0. 0. 0. 0. 0. 0.
 0. 0. 0. 0. 0. 0. 0. 0.
 0. 0. 0. 0. 0. 0. 0. 0.
 0. 0. 0. 0. 0. 0. 0. 0.

\$AX=2..ZB1.....ZB2.....ZB3.....ZB4.....ZB5.....ZB6.....ZB7.....ZB8
 -1.037E-03-9.828E-04-9.359E-04-8.947E-04-8.581E-04-8.254E-04-7.958E-04-7.689E-04
 -7.442E-04-7.214E-04-7.003E-04-6.807E-04-6.624E-04-6.453E-04-6.291E-04-6.139E-04
 -5.996E-04-5.860E-04-5.730E-04-5.607E-04-5.490E-04-5.378E-04-5.270E-04-5.168E-04
 -5.069E-04-4.975E-04-4.883E-04-4.796E-04-4.711E-04-4.630E-04-4.551E-04-4.475E-04
 -4.401E-04-4.329E-04-4.260E-04-4.193E-04-4.128E-04-4.065E-04-4.003E-04-3.943E-04
 -3.885E-04-3.828E-04-3.773E-04-3.719E-04-3.667E-04-3.616E-04-3.566E-04-3.517E-04
 -3.469E-04-3.423E-04-3.378E-04-3.333E-04-3.290E-04-3.247E-04-3.205E-04-3.165E-04
 -3.125E-04-3.086E-04-3.047E-04-3.010E-04-2.973E-04-2.937E-04-2.901E-04-2.867E-04
 -2.832E-04-2.799E-04-2.766E-04-2.734E-04-2.702E-04-2.671E-04-2.640E-04-2.610E-04
 -2.581E-04-2.552E-04-2.523E-04-2.495E-04-2.467E-04-2.440E-04-2.413E-04-2.387E-04
 -2.361E-04-2.336E-04-2.310E-04-2.286E-04-2.261E-04-2.237E-04-2.214E-04-2.191E-04
 -2.168E-04-2.145E-04-2.123E-04-2.101E-04-2.079E-04-2.058E-04-2.037E-04-2.016E-04
 -1.996E-04-1.976E-04-1.956E-04-1.936E-04-1.917E-04-1.898E-04-1.879E-04-1.861E-04
 -1.842E-04-1.824E-04-1.806E-04-1.789E-04-1.772E-04-1.754E-04-1.738E-04-1.721E-04
 -1.704E-04-1.688E-04-1.672E-04-1.656E-04-1.641E-04-1.625E-04-1.610E-04-1.595E-04
 -1.580E-04-1.565E-04-1.551E-04-1.536E-04-1.522E-04-1.508E-04-1.494E-04-1.481E-04
 -1.467E-04-1.454E-04-1.441E-04-1.428E-04-1.415E-04-1.402E-04-1.389E-04-1.377E-04
 -1.365E-04-1.353E-04-1.341E-04-1.329E-04-1.317E-04-1.305E-04-1.294E-04-1.283E-04
 -1.271E-04-1.260E-04-1.249E-04-1.239E-04-1.228E-04-1.217E-04-1.207E-04-1.197E-04
 -1.186E-04-1.176E-04-1.166E-04-1.157E-04-1.147E-04-1.137E-04-1.128E-04-1.118E-04
 -1.109E-04-1.100E-04-1.091E-04-1.082E-04-1.073E-04-1.064E-04-1.055E-04-1.047E-04
 -1.038E-04-1.030E-04-1.021E-04-1.013E-04-1.005E-04-9.976E-05-9.897E-05-9.819E-05
 -9.742E-05-9.666E-05-9.590E-05-9.516E-05-9.442E-05-9.369E-05-9.298E-05-9.227E-05
 -9.157E-05-9.088E-05-9.020E-05-8.952E-05-8.886E-05-8.820E-05-8.756E-05-8.692E-05
 -8.629E-05-8.567E-05-8.506E-05-8.446E-05-8.386E-05-8.328E-05-8.270E-05-8.214E-05


```

$$ Main Processor data ****
$ type.case.....problem description.....]
   3      1 NEOD Linear Shaped Charge Penetration - S. Segletes JUN 1994
$
$$ main run data ****
$
$cycl.ncpu.....time.....dtmax.....dtmin.....ssf.....tmax.....cpmax.....emax
  0    0 0000.0e-6      1.0     1.e-11      0.80    15.0e-6 00000.00
$tplt.drop..add.pres.push..hrg....vfract.....vnref...nabfact...sphdist/////////
  1    0    0    0    0    0
$.sys.nplt.lplt.dplt.....dtsys.....tsys....dtnode.....tnode.....dtdyn.....tdyn
  1    0           1.0e-6       0.0     0.25e-6      0.0
$.....time....echeck....ncheck.....rdamp.save.burn.yprt.ndat.slpr.proj..pat.rzne
 0.4E-06   1001.0      999      0.0      3      0      1    500      0      0      0      0
 0.8E-06   1001.0      999      0.0      3      0      1    500      0      0      0      0
 01.2E-06   1001.0      999      0.0      3      0      1    500      0      0      0      0
 01.6E-06   1001.0      999      0.0      3      0      1    500      0      0      0      0
 02.0E-06   1001.0      999      0.0      3      0      1    500      0      0      0      0
 04.0E-06   1001.0      999      0.0      3      0      1    500      0      0      0      0
 06.0E-06   1001.0      999      0.0      3      0      1    500      0      0      0      0
 08.0E-06   1001.0      999      0.0      3      0      1    500      0      0      0      0
 10.0E-06   1001.0      999      0.0      3      0      1    500      0      0      0      0
 15.1E-06   1001.0      999      0.0      3      0      1    500      0      0      0      0

```

```
$$ Main Processor data ****
$ 
$type.case.....problem description.....]
```

```

3      1 NEOD Linear Shaped Charge Penetration - S. Segletes JUN 1994
$  

$$ main run data ****  

$  

$scycl.ncpu.....time.....dtmax.....dtmin.....ssf.....tmax.....cpmax.....emax  

    0      0 0015.0e-6      1.0      1.e-11      0.80      30.0e-6  00000.00  

$tplt.drop..add.pres.push..hrg....vfract.....vnref...nabfact...sphdist//////////  

    1      0      0      0      0      0  

$.sys.nplt.lplt.dplt.....dtsys.....tsys....dtnode.....tnode.....dtdyn.....tdyn  

    1      0              1.0e-6      0.0      0.25e-6      0.0  

$.....time....echeck....ncheck.....rdamp.save.burn.yprt.ndat.slpr.proj..pat.rzne  

  20.0E-06    1001.0      999      0.0      3      0      1      500      0      0      0  

  25.0E-06    1001.0      999      0.0      3      0      1      500      0      0      0  

  30.1E-06    1001.0      999      0.0      3      0      1      500      0      0      0

```

```

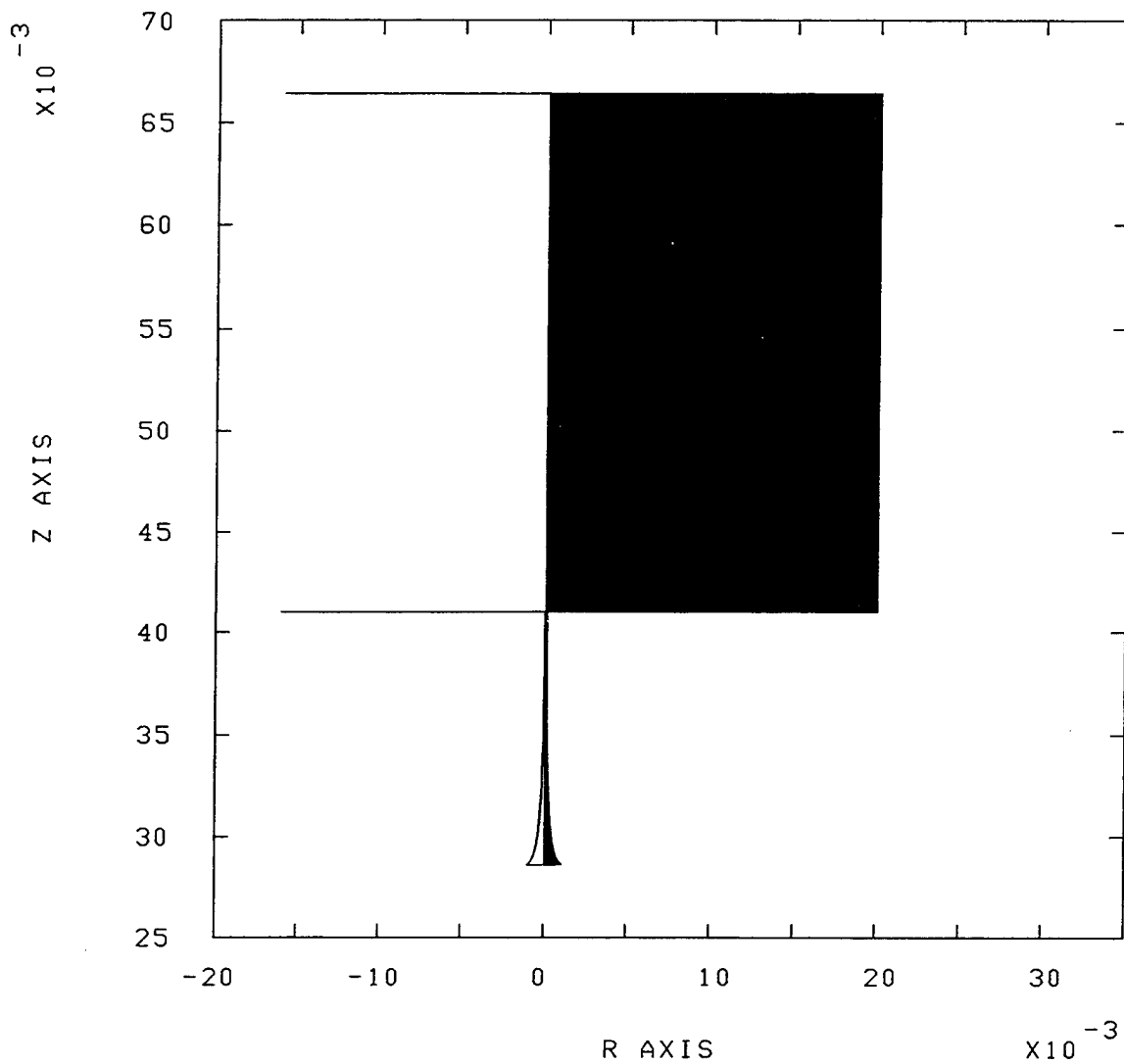
& 5051.104, 5036.811, 5022.705, 5008.770, 4995.006,
& 4981.402, 4967.948, 4954.640, 4941.470, 4928.432,
& 4915.522, 4902.730, 4890.058, 4877.499, 4865.044/
  data f2 (101:200) /
& 4852.695, 4840.443, 4828.293, 4816.229, 4804.255,
& 4792.370, 4780.569, 4768.847, 4757.201, 4745.629,
& 4734.132, 4722.703, 4711.340, 4700.047, 4688.817,
& 4677.646, 4666.537, 4655.483, 4644.486, 4633.543,
& 4622.653, 4611.813, 4601.025, 4590.284, 4579.589,
& 4568.938, 4558.335, 4547.771, 4537.249, 4526.767,
& 4516.324, 4505.918, 4495.553, 4485.220, 4474.923,
& 4464.657, 4454.425, 4444.227, 4434.060, 4423.919,
& 4413.810, 4403.728, 4393.673, 4383.646, 4373.641,
& 4363.665, 4353.709, 4343.778, 4333.874, 4323.984,
& 4314.120, 4304.275, 4294.449, 4284.642, 4274.856,
& 4265.087, 4255.335, 4245.596, 4235.875, 4226.173,
& 4216.479, 4206.805, 4197.142, 4187.492, 4177.854,
& 4168.226, 4158.610, 4149.006, 4139.414, 4129.829,
& 4120.253, 4110.687, 4101.126, 4091.576, 4082.031,
& 4072.493, 4062.959, 4053.431, 4043.913, 4034.394,
& 4024.881, 4015.372, 4005.866, 3996.359, 3986.856,
& 3977.356, 3967.855, 3958.356, 3948.855, 3939.354,
& 3929.855, 3920.353, 3910.849, 3901.341, 3891.831,
& 3882.318, 3872.799, 3863.280, 3853.754, 3844.221/
  data f3 (201:300) /
& 3834.684, 3825.138, 3815.587, 3806.028, 3796.463,
& 3786.886, 3777.305, 3767.709, 3758.105, 3748.493,
& 3738.867, 3729.229, 3719.582, 3709.917, 3700.242,
& 3690.552, 3680.849, 3671.128, 3661.395, 3651.639,
& 3641.872, 3632.084, 3622.281, 3612.458, 3602.614,
& 3592.750, 3582.864, 3572.957, 3563.029, 3553.076,
& 3543.100, 3533.097, 3523.072, 3513.018, 3502.937,
& 3492.827, 3482.693, 3472.525, 3462.327, 3452.100,
& 3441.836, 3431.540, 3421.210, 3410.843, 3400.439,
& 3389.999, 3379.520, 3369.000, 3358.439, 3347.835,
& 3337.187, 3326.496, 3315.757, 3304.969, 3294.135,
& 3283.246, 3272.307, 3261.312, 3250.263, 3239.155,
& 3227.989, 3216.759, 3205.468, 3194.111, 3182.687,
& 3171.193, 3159.625, 3147.983, 3136.264, 3124.465,
& 3112.583, 3100.617, 3088.560, 3076.413, 3064.168,
& 3051.824, 3039.376, 3026.822, 3014.156, 3001.373,
& 2988.468, 2975.438, 2962.275, 2948.973, 2935.527,
& 2921.930, 2908.173, 2894.251, 2880.155, 2865.874,
& 2851.396, 2836.715, 2821.818, 2806.689, 2791.314,
& 2775.681, 2759.770, 2743.559, 2727.032, 2710.160/
  data f4 (301:311) /
& 2692.922, 2675.279, 2657.195, 2638.635, 2619.551,
& 2599.880, 2579.562, 2558.512, 2536.633, 2513.806,
& 2489.873/
C
  write (*,100) field
100 format (5f10.3)
  mjdelt = 311
  idelt = 621
C  DO FOR NODES IN JET ONLY
  do 10 n = 1, 2174
    index = mod(n-1,idelt) + 1

```

```
c      print *, 'index=', index
      if (index .le. mjdel) then
          i2 = mjdel + 1 - index
c      print *, 'i2=',i2
      zdot(n) = field(i2)
      else
          i1 = index - mjdel
          i2 = mjdel + 1 - i1
c      print *,'i1,i2=',i1,i2
      zdot(n) = (field(i2) + field(i2-1)) * 0.5
      end if
10 continue
      return
      end
```

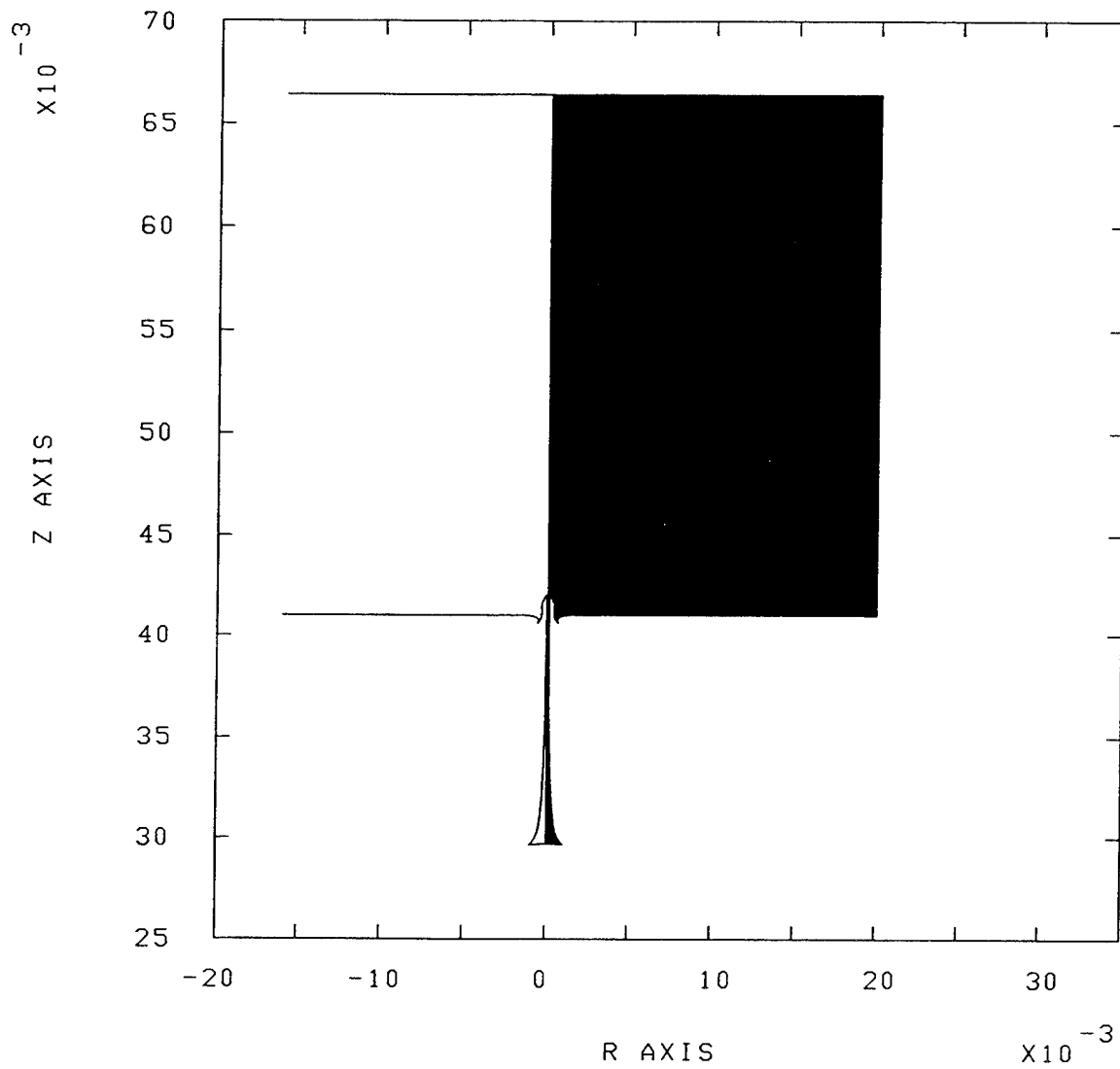
EPIC POST PROCESSOR, POST1 (1992-2) 09:31:15 25-Jul-94
2-D PLANE STRAIN GEOMETRY

Linear SC Jet Penetration , CASE = 1; TIME = 0.00000000; CYCLE = 0



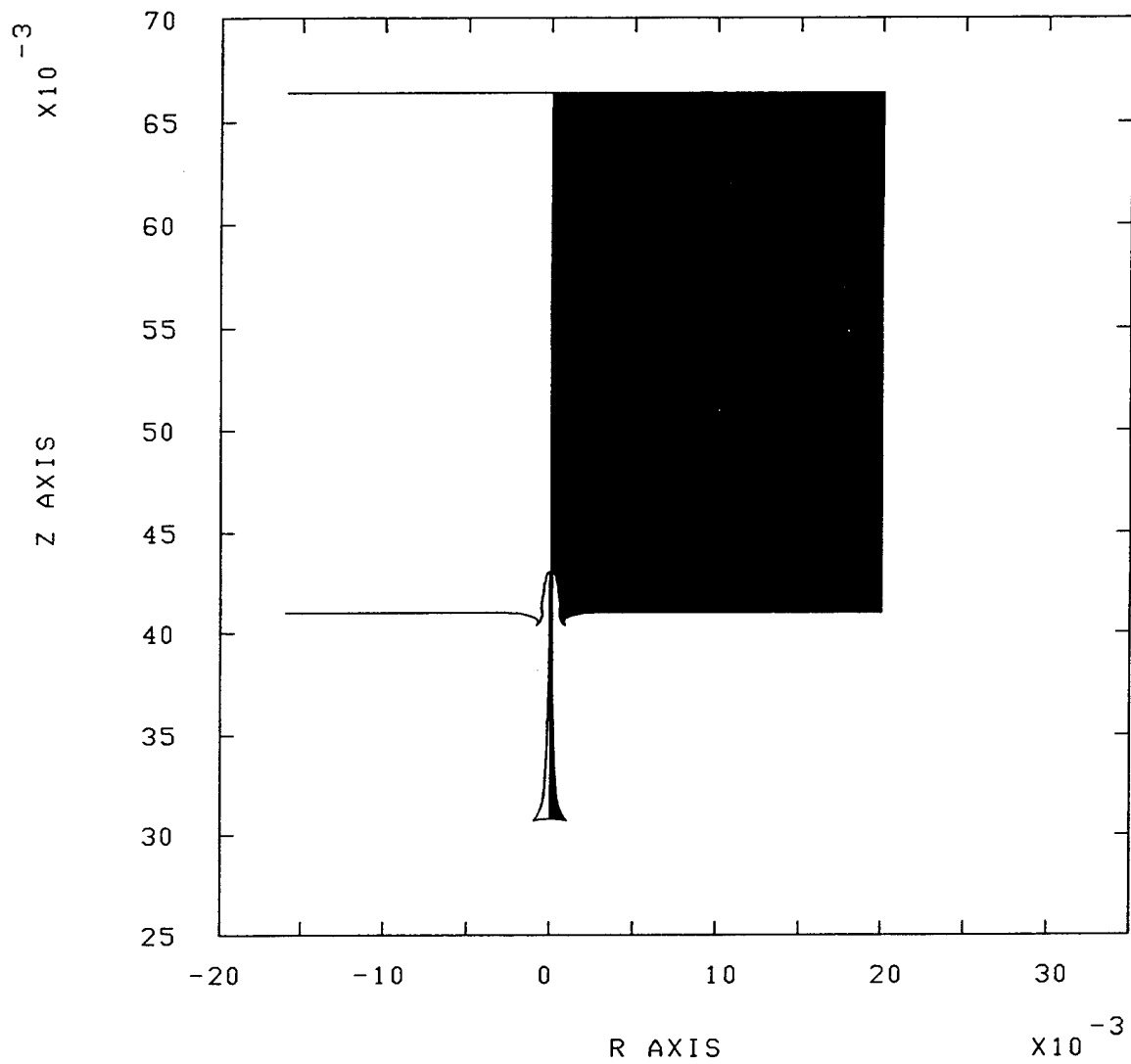
EPIC POST PROCESSOR, POST1 (1992-2) 09:31:57 25-Jul-94
2-D PLANE STRAIN GEOMETRY

Linear SC Jet Penetration ; CASE = 1; TIME = 0.00000040; CYCLE = 809



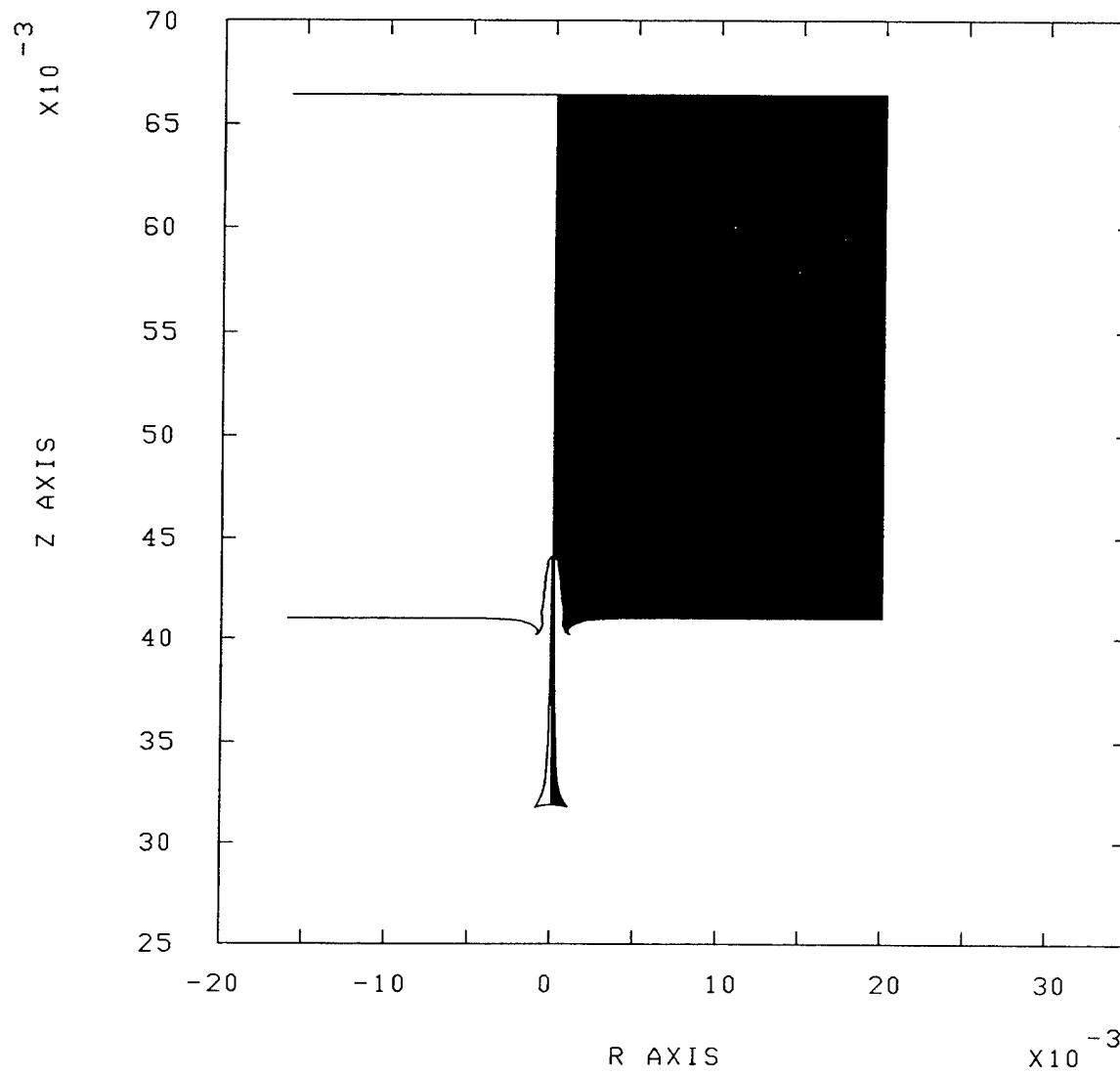
EPIC POST PROCESSOR, POST1 (1992-2) 09:32:38 25-Jul-94
2-D PLANE STRAIN GEOMETRY

Linear SC Jet Penetration ; CASE = 1; TIME = 0.00000080; CYCLE = 1601



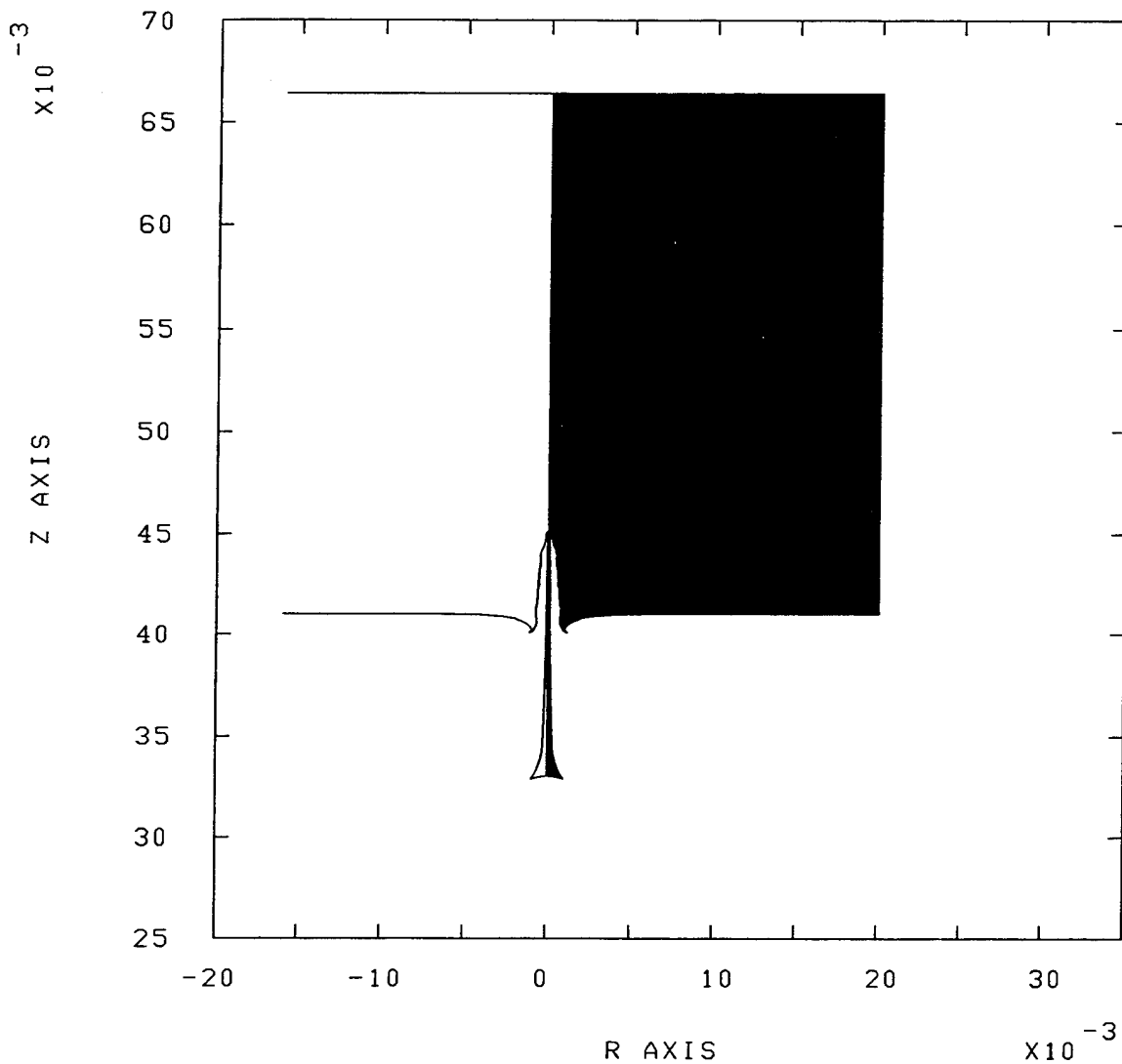
EPIC POST PROCESSOR, POST1 (1992-2) 09:33:18 25-Jul-94
2-D PLANE STRAIN GEOMETRY

Linear SC Jet Penetration ; CASE = 1; TIME = 0.00000120; CYCLE = 2339



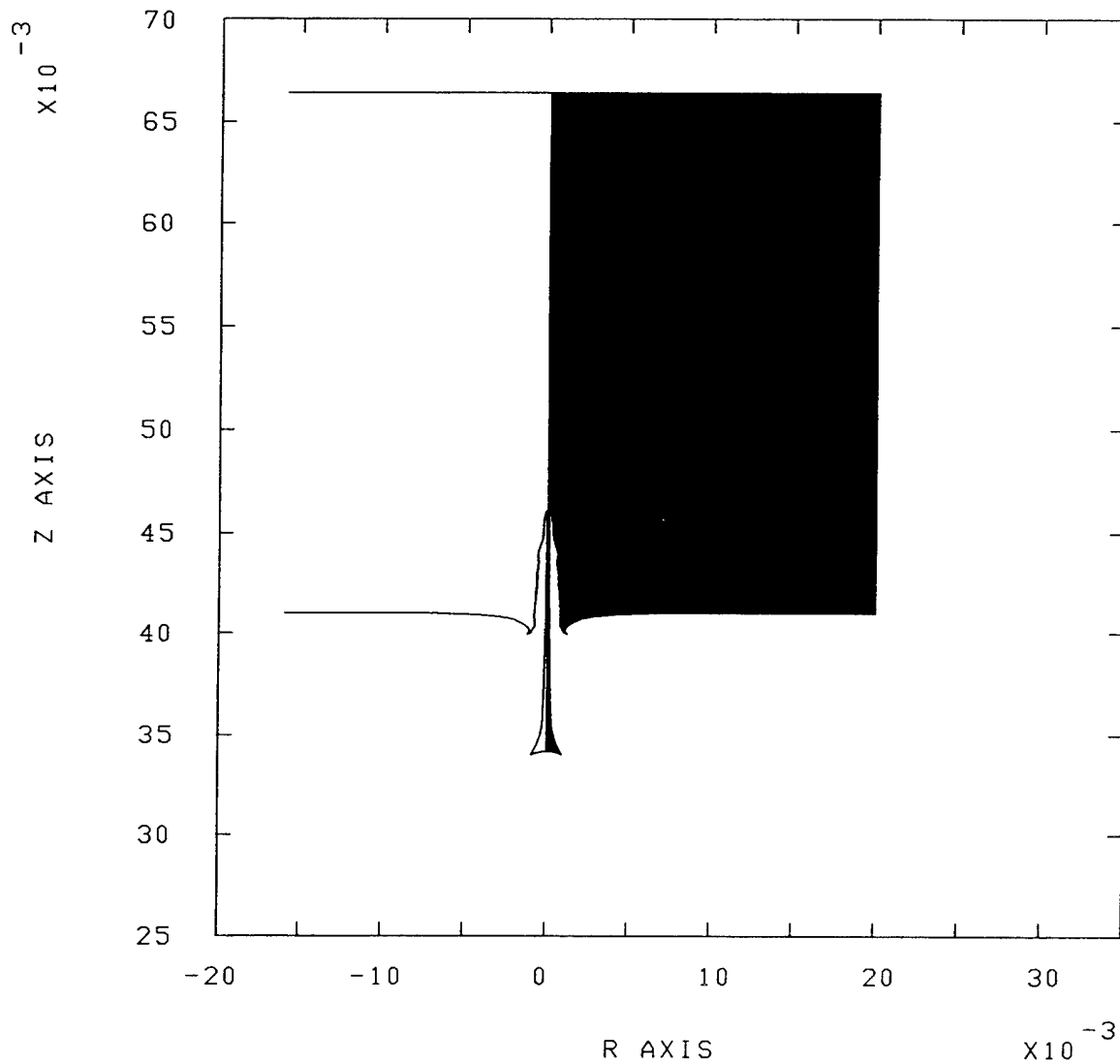
EPIC POST PROCESSOR, POST1 (1992-2) 09:33:55 25-Jul-94
2-D PLANE STRAIN GEOMETRY

Linear SC Jet Penetration ; CASE = 1; TIME = 0.00000160; CYCLE = 2910



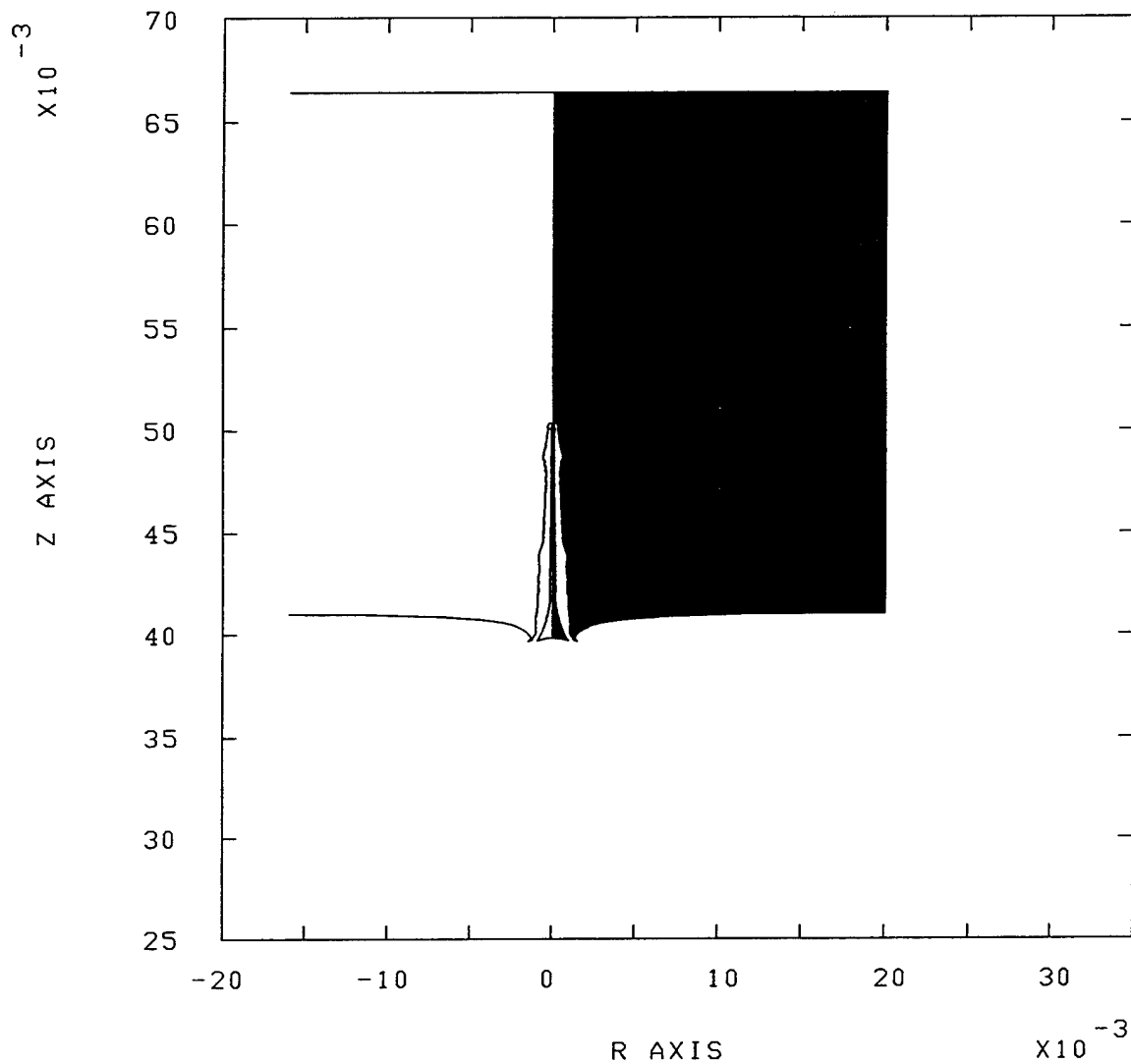
EPIC POST PROCESSOR, POST1 (1992-2) 09:34:45 25-Jul-94
2-D PLANE STRAIN GEOMETRY

Linear SC Jet Penetration ; CASE = 1; TIME = 0.00000200; CYCLE = 3474



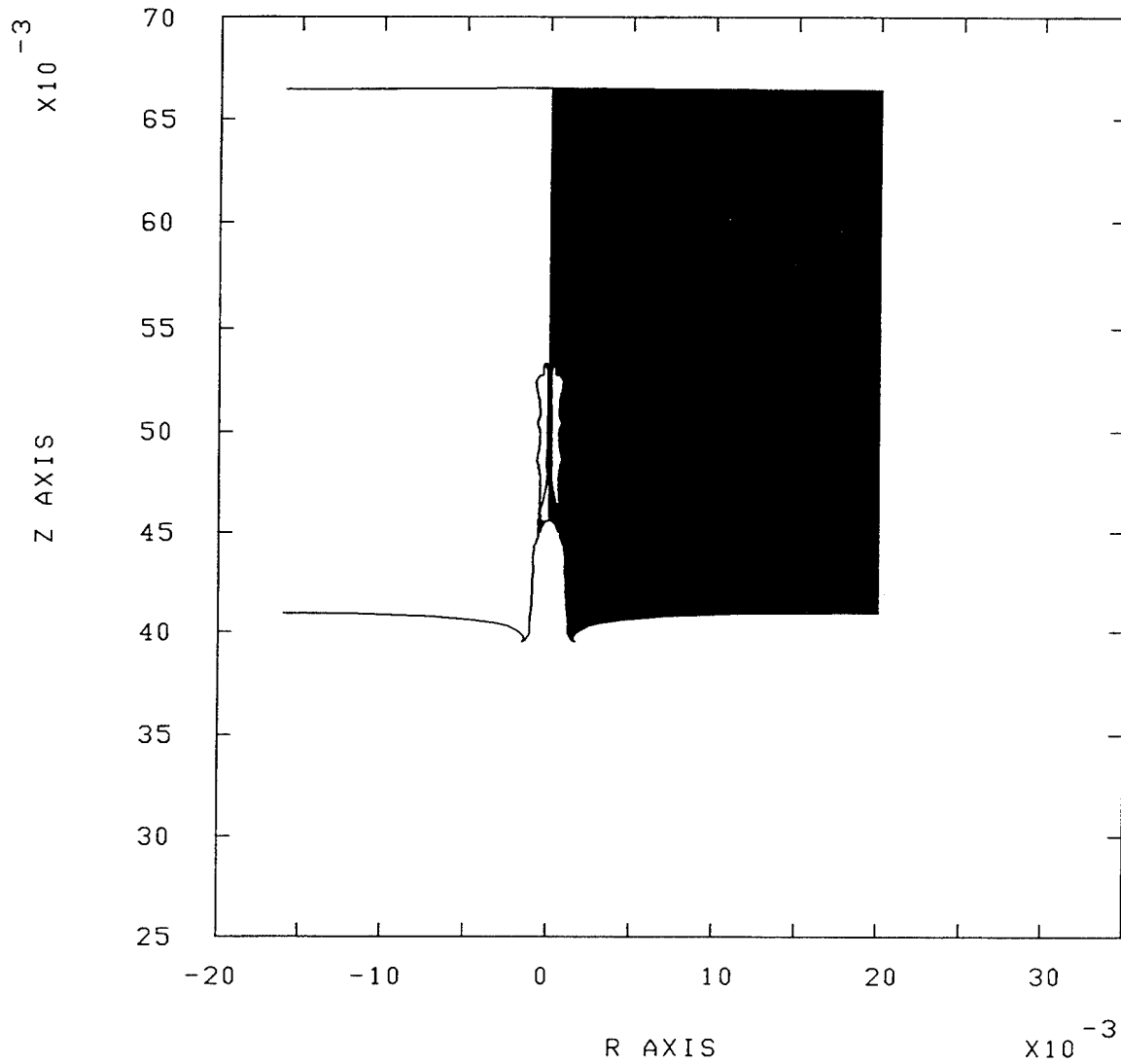
EPIC POST PROCESSOR, POST1 (1992-2) 09:35:29 25-Jul-94
2-D PLANE STRAIN GEOMETRY

Linear SC Jet Penetration ; CASE = 1; TIME = 0.00000400; CYCLE = 6111



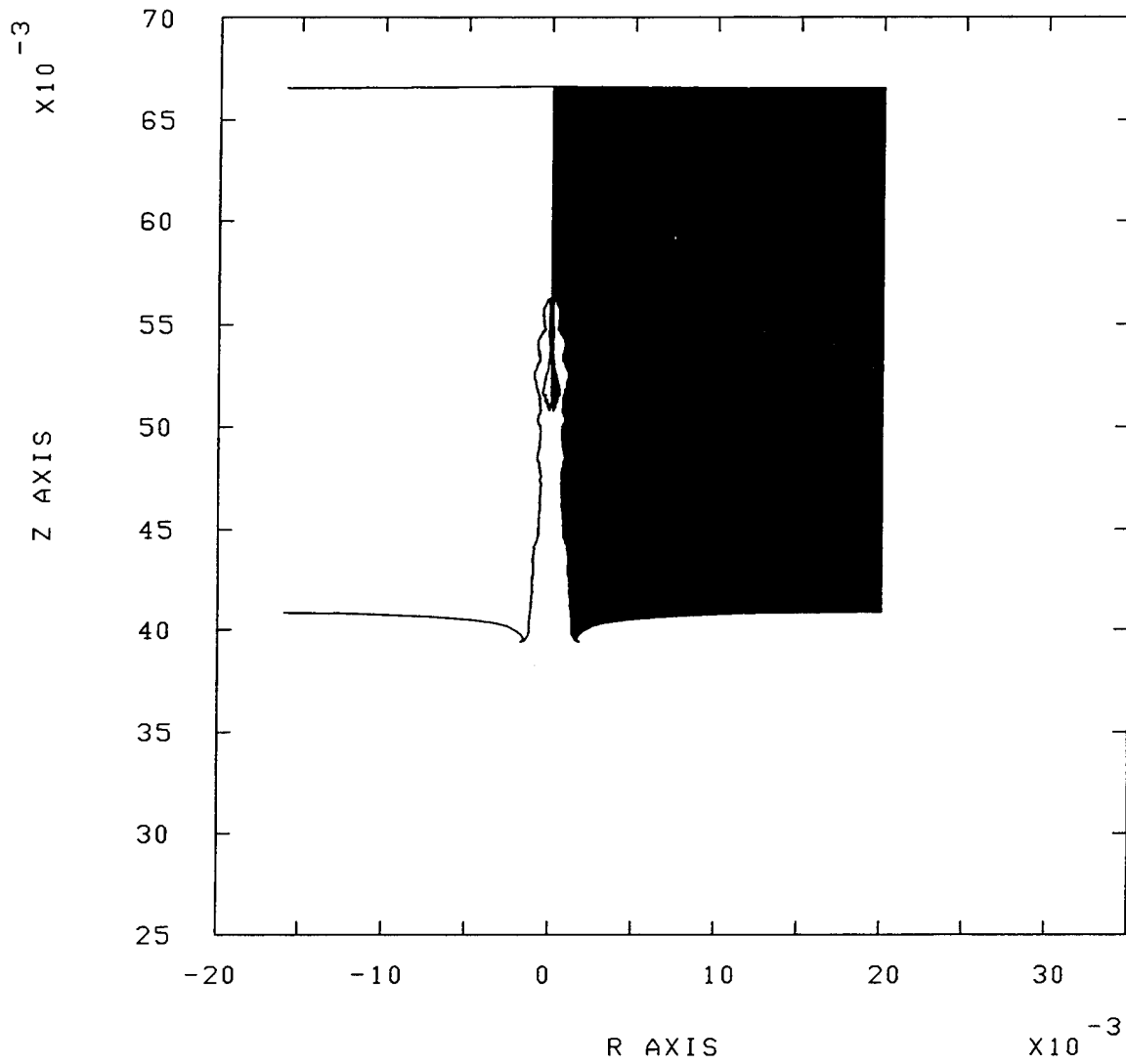
EPIC POST PROCESSOR, POST1 (1992-2) 09:36:00 25-Jul-94
2-D PLANE STRAIN GEOMETRY

Linear SC Jet Penetration ; CASE = 1; TIME = 0.00000600; CYCLE = 8646



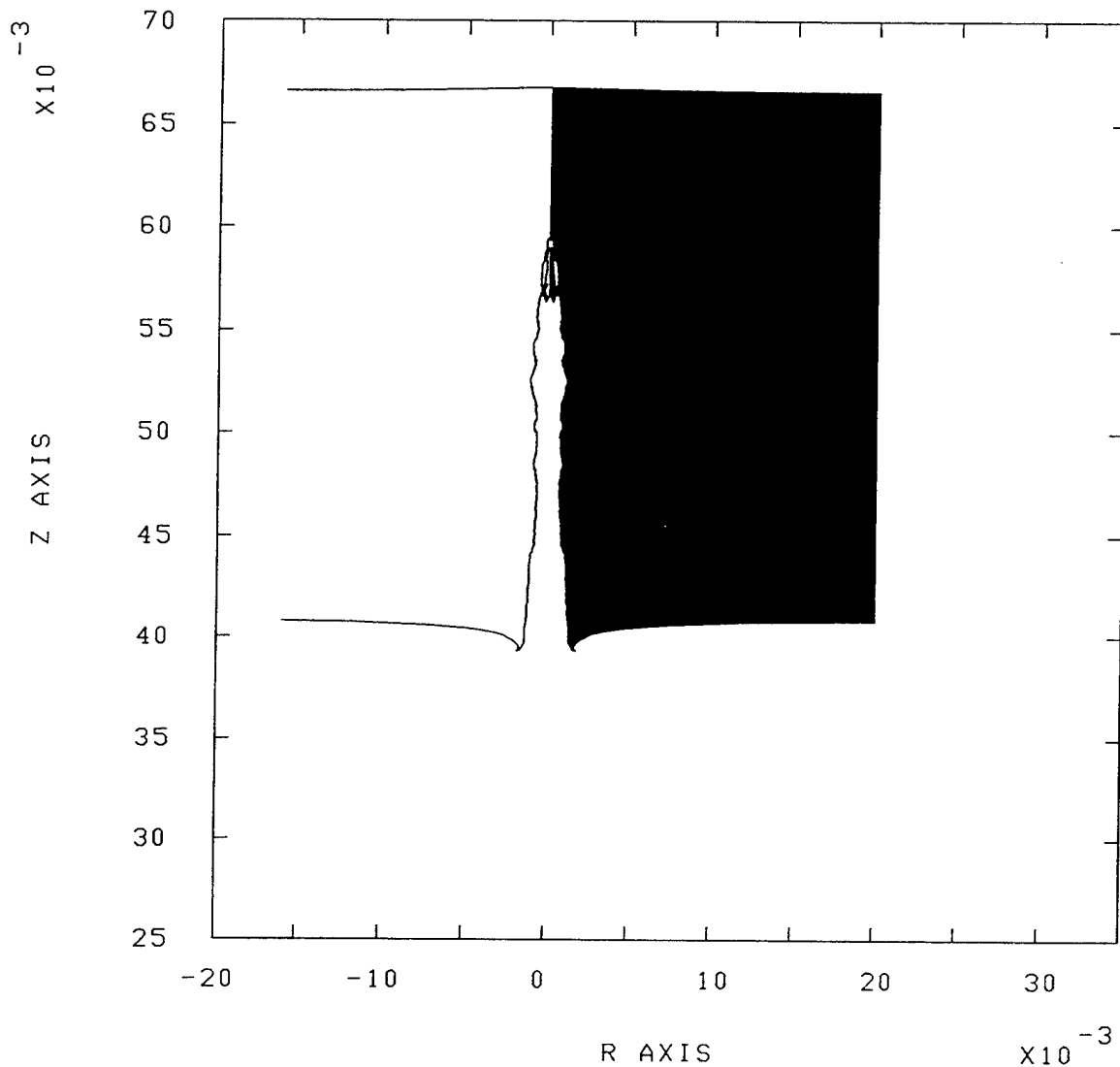
EPIC POST PROCESSOR, POST1 (1992-2) 09:36:23 25-Jul-94
2-D PLANE STRAIN GEOMETRY

Linear SC Jet Penetration ; CASE = 1; TIME = 0.00000800; CYCLE = 11163



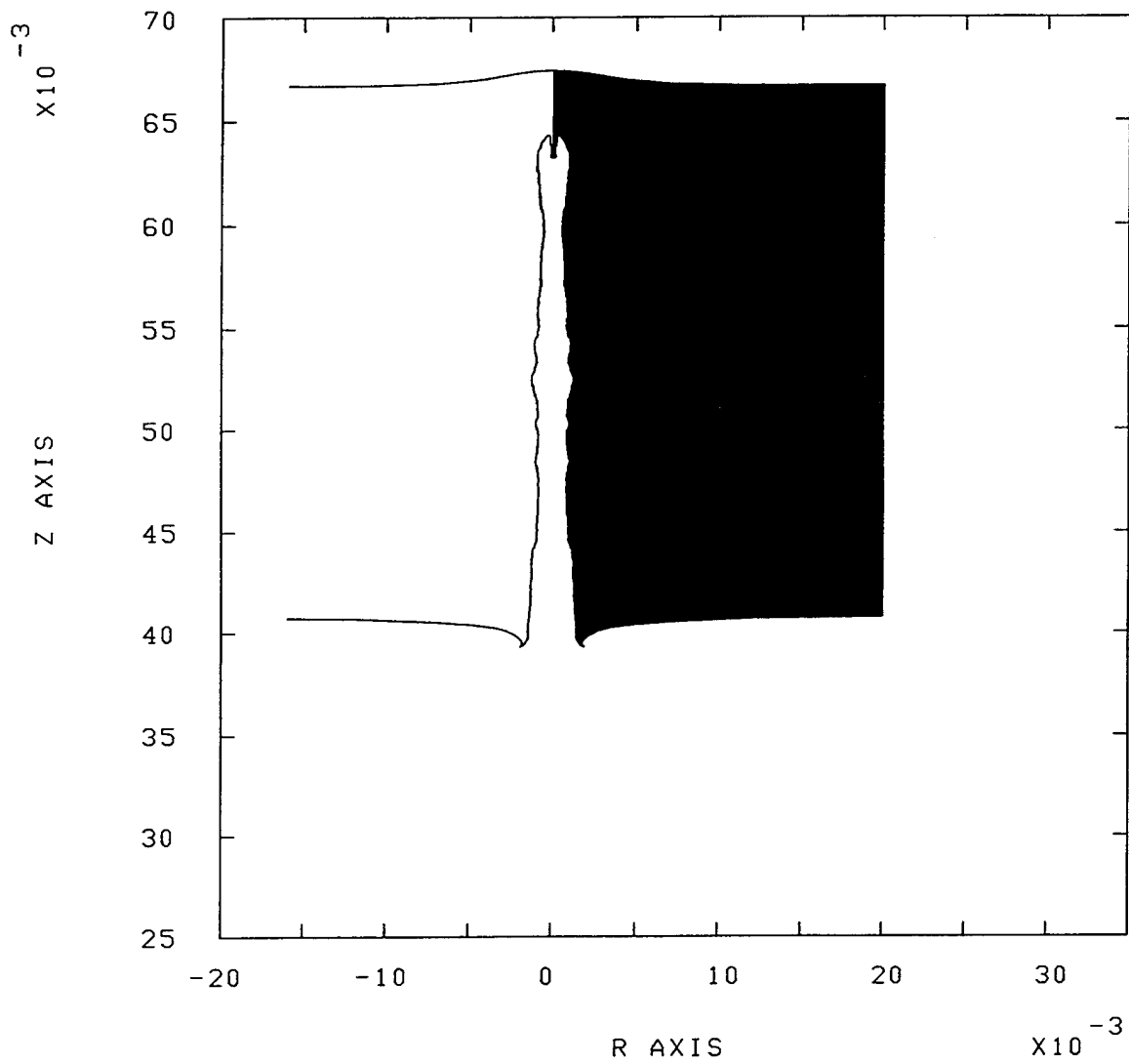
EPIC POST PROCESSOR, POST1 (1992-2) 09:36:45 25-Jul-94
2-D PLANE STRAIN GEOMETRY

Linear SC Jet Penetration ; CASE = 1; TIME = 0.00001000; CYCLE = 13670



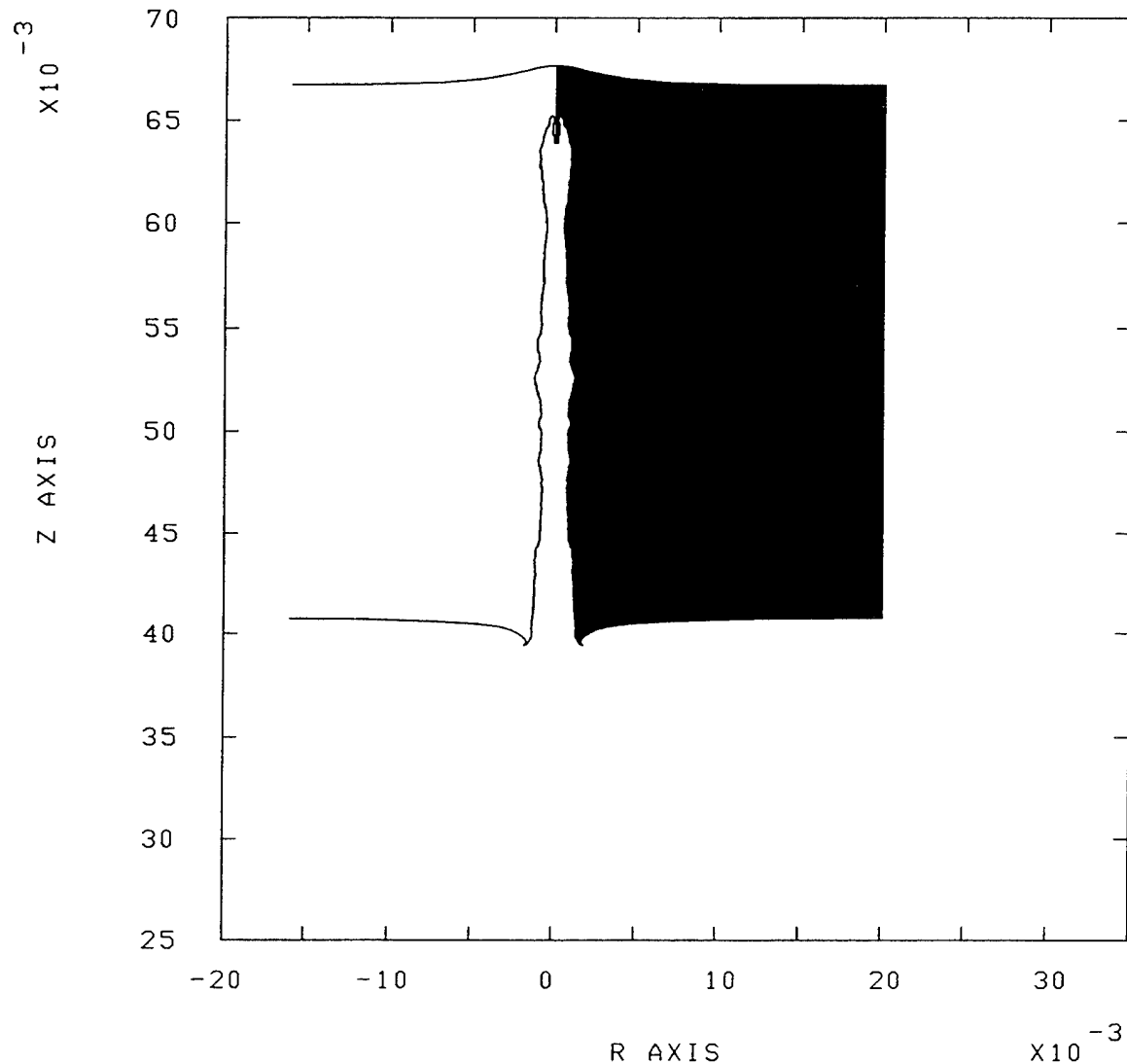
EPIC POST PROCESSOR, POST1 (1992-2) 09:37:06 25-Jul-94
2-D PLANE STRAIN GEOMETRY

Linear SC Jet Penetration ; CASE = 1; TIME = 0.00001500; CYCLE = 19897



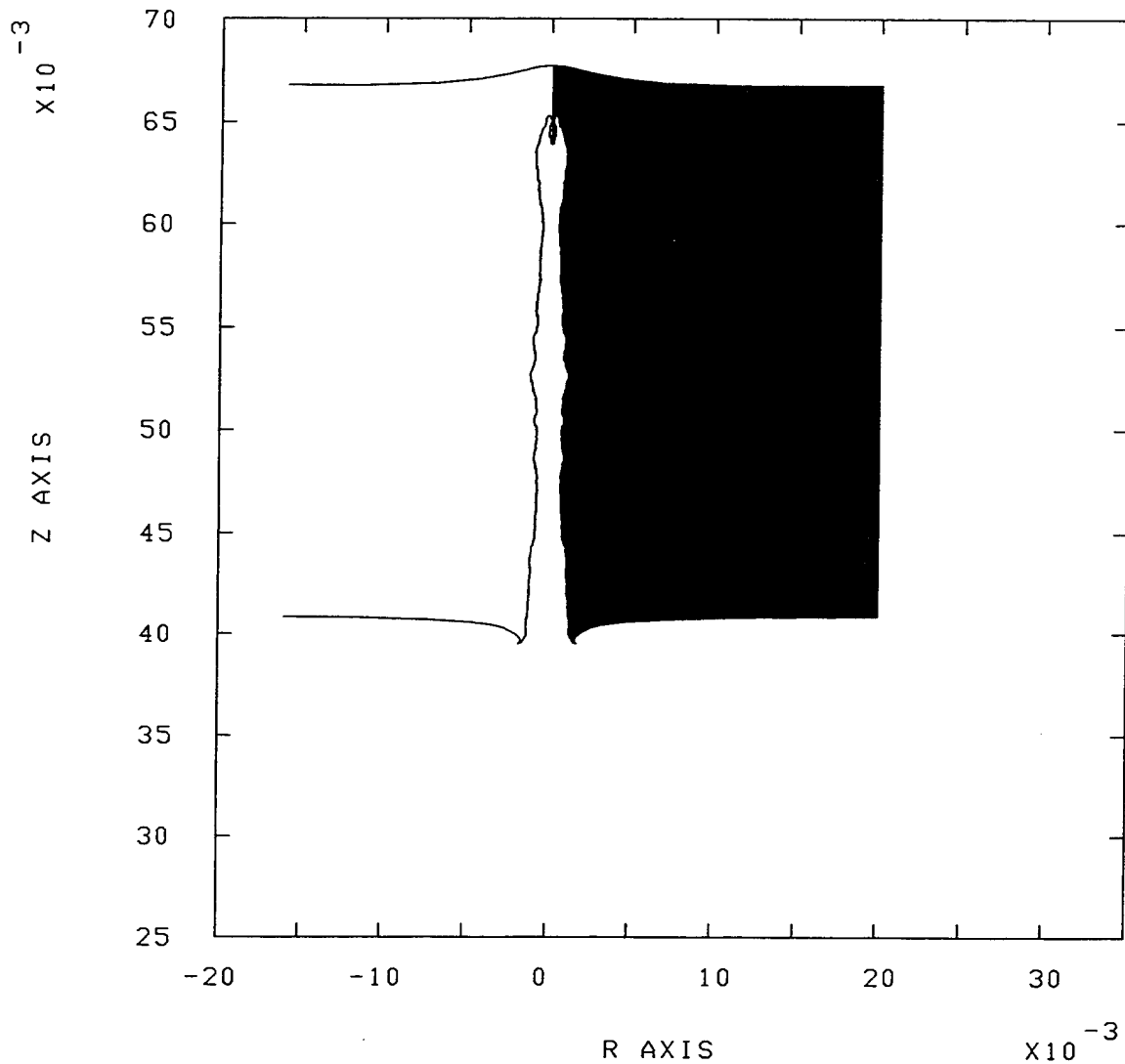
EPIC POST PROCESSOR, POST1 (1992-2) 10:52:37 10-Aug-94
2-D PLANE STRAIN GEOMETRY

Linear SC Jet Penetration ; CASE = 1; TIME = 0.00002000; CYCLE = 24520



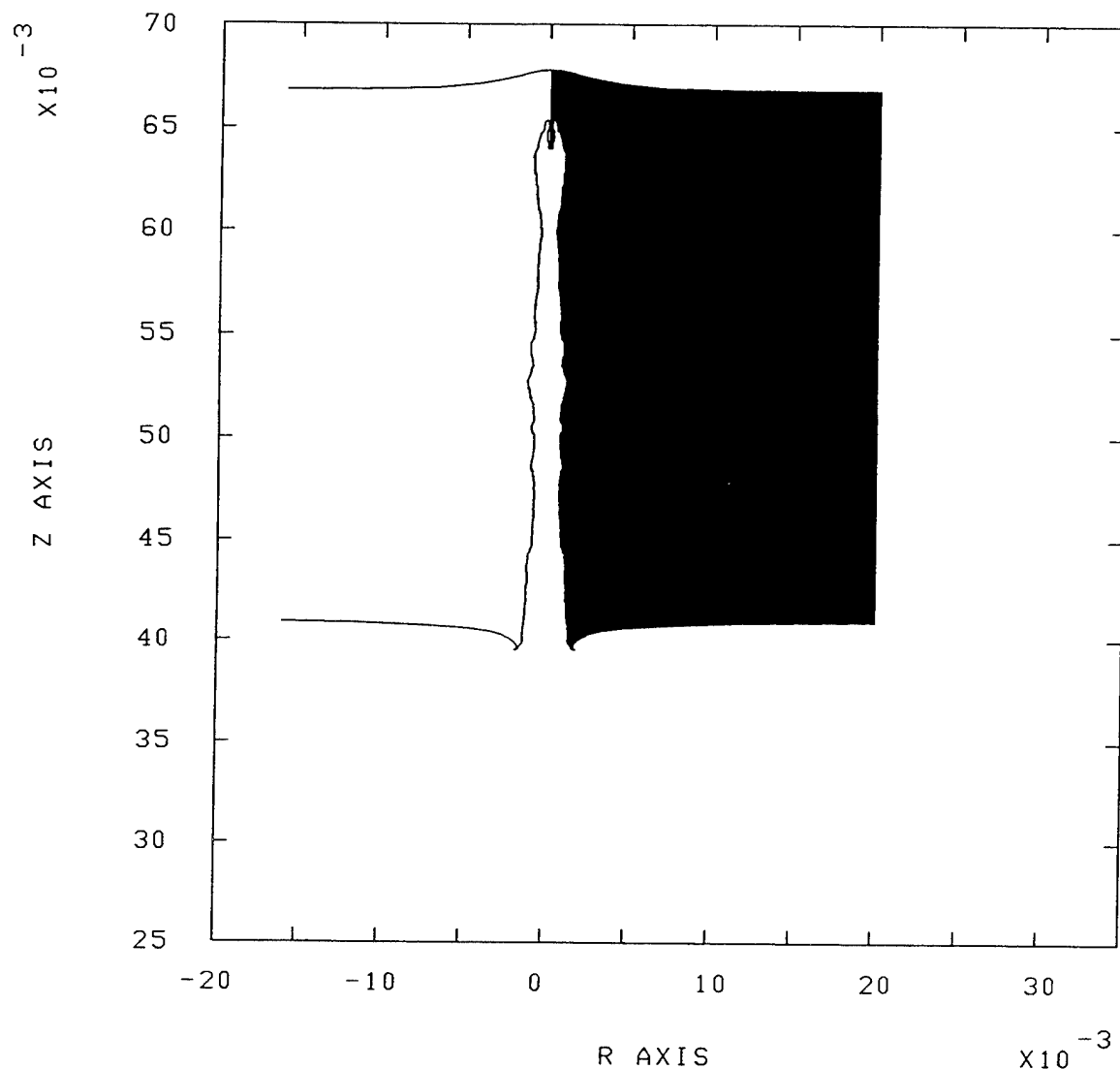
EPIC POST PROCESSOR, POST1 (1992-2) 08:05:14 12-Aug-94
2-D PLANE STRAIN GEOMETRY

Linear SC Jet Penetration ; CASE = 1; TIME = 0.00002500; CYCLE = 29139



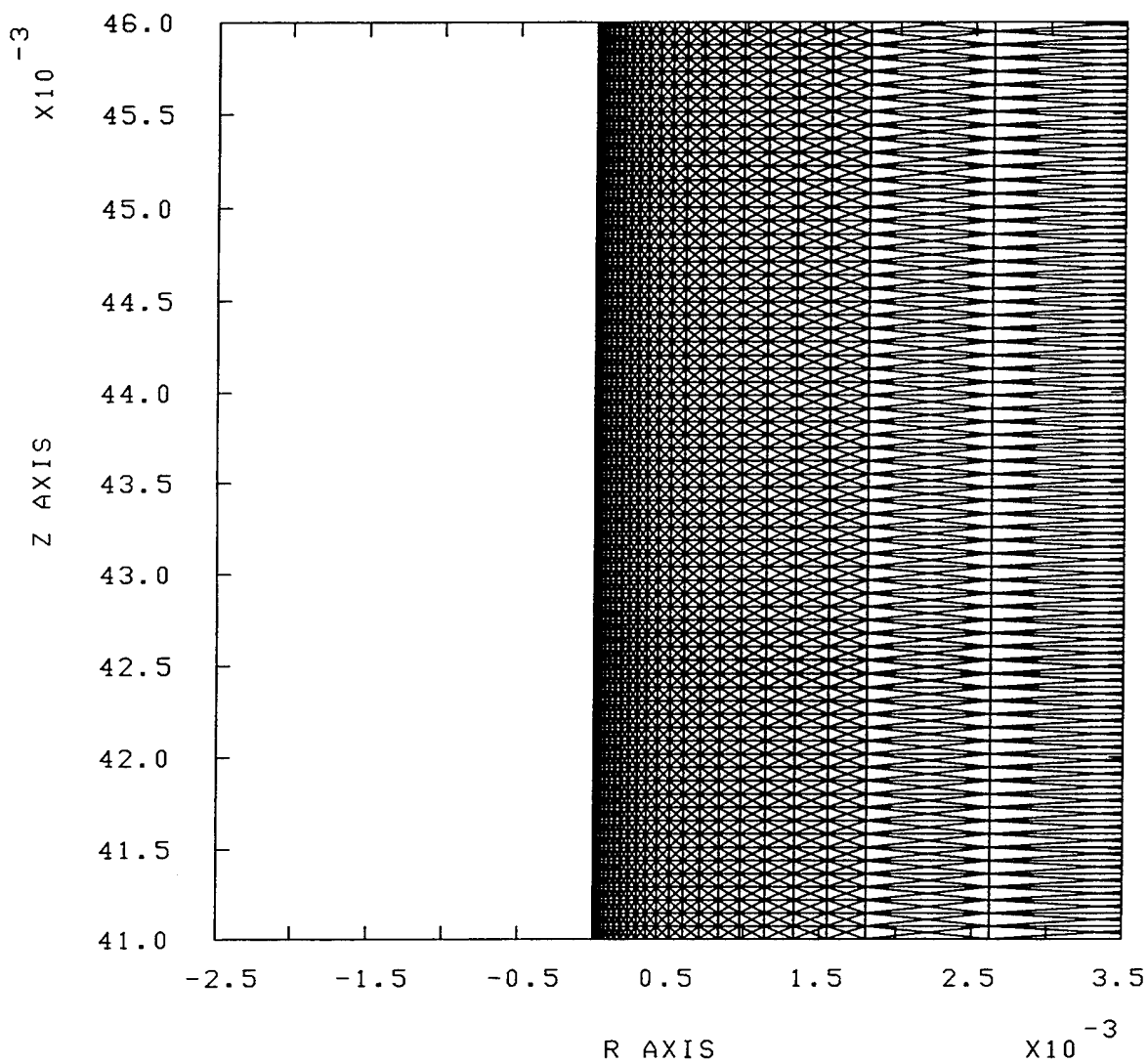
EPIC POST PROCESSOR, POST1 (1992-2) 08:05:32 12-Aug-94
2-D PLANE STRAIN GEOMETRY

Linear SC Jet Penetration ; CASE = 1; TIME = 0.00003000; CYCLE = 33752



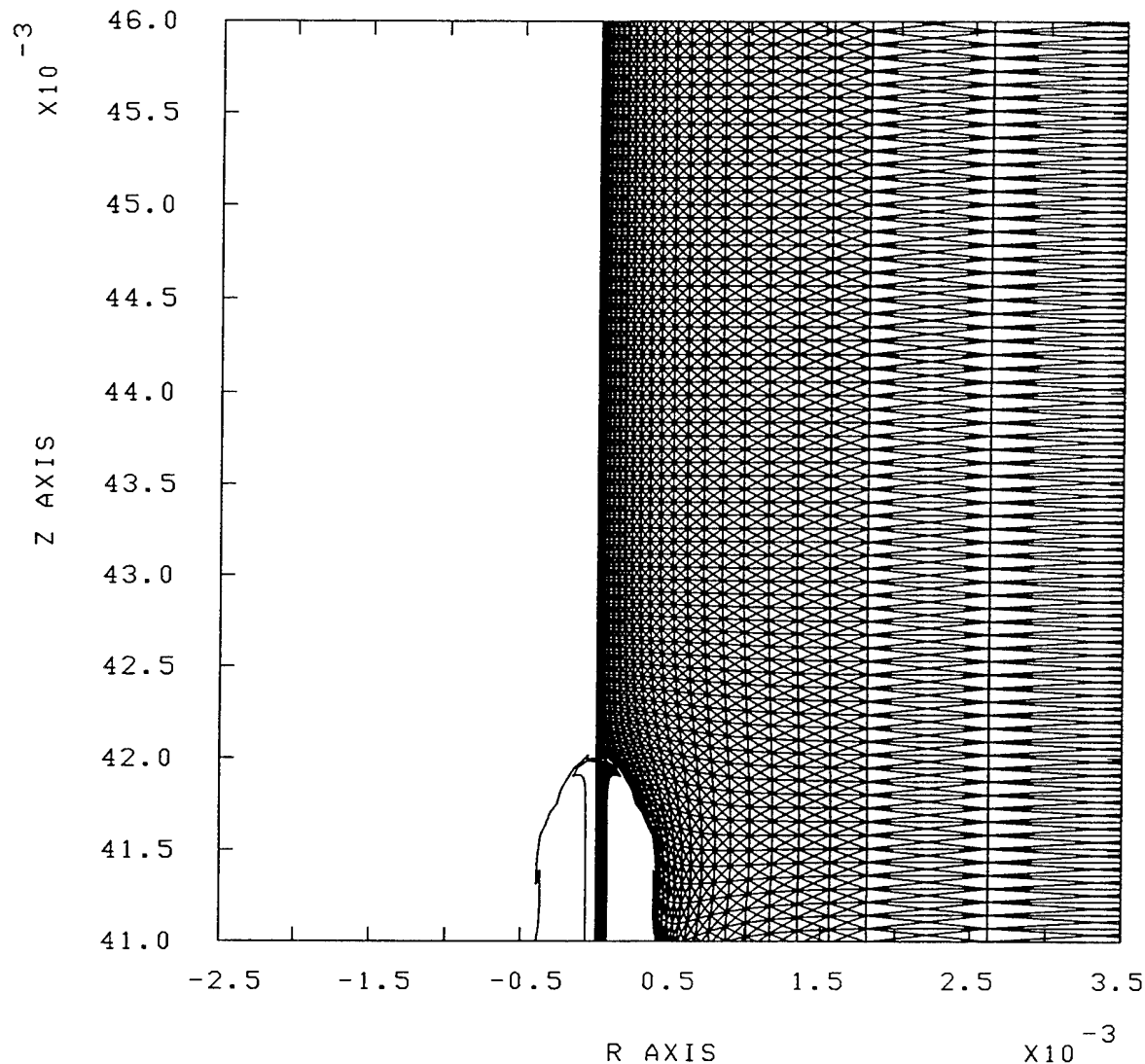
EPIC POST PROCESSOR, POST1 (1992-2) 09:31:14 25-Jul-94
2-D PLANE STRAIN GEOMETRY

Linear SC Jet Penetration ; CASE = 1; TIME = 0.00000000; CYCLE = 0



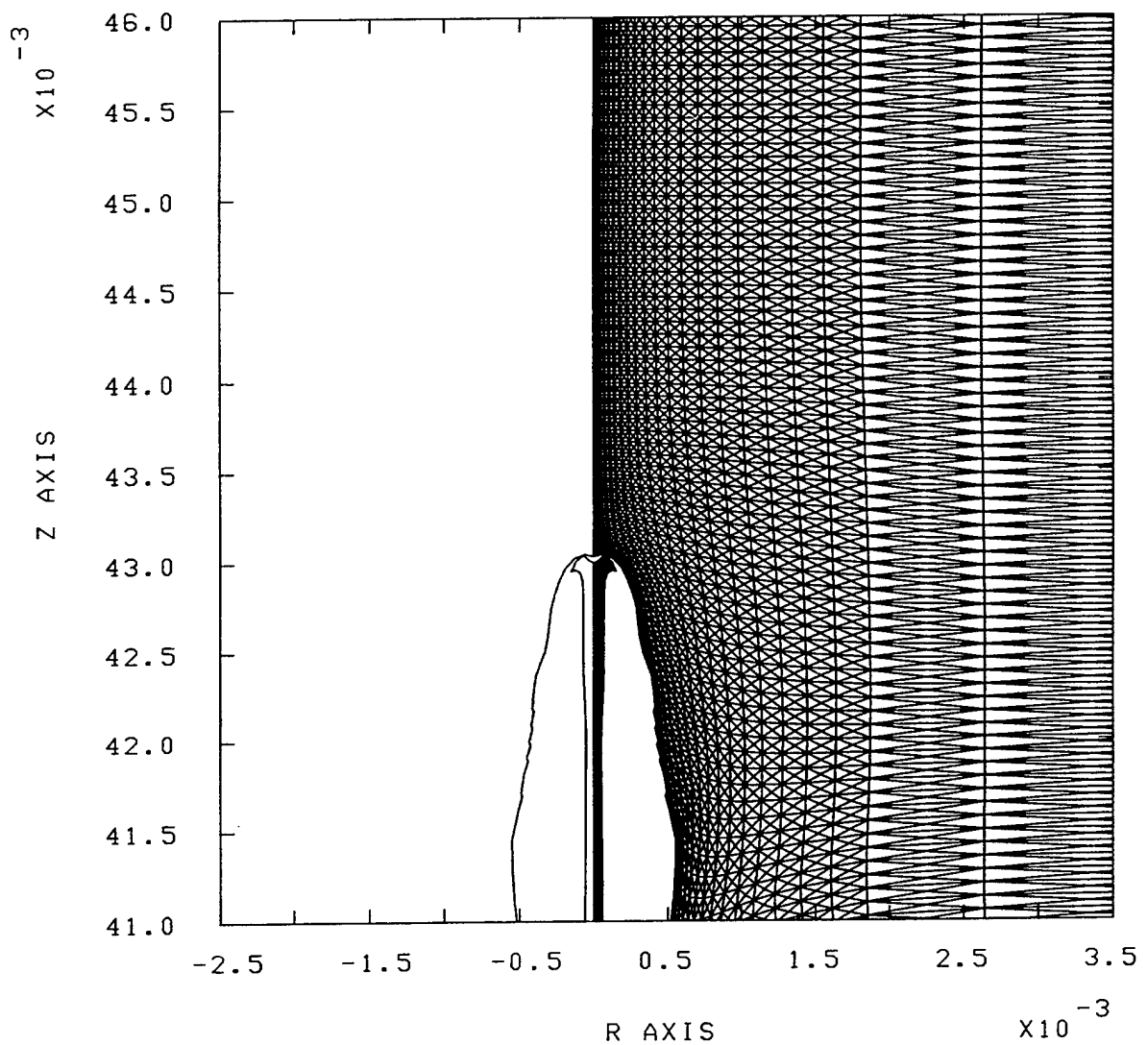
EPIC POST PROCESSOR, POST1 (1992-2) 09:31:55 25-Jul-94
2-D PLANE STRAIN GEOMETRY

Linear SC Jet Penetration ; CASE = 1; TIME = 0.00000040; CYCLE = 809



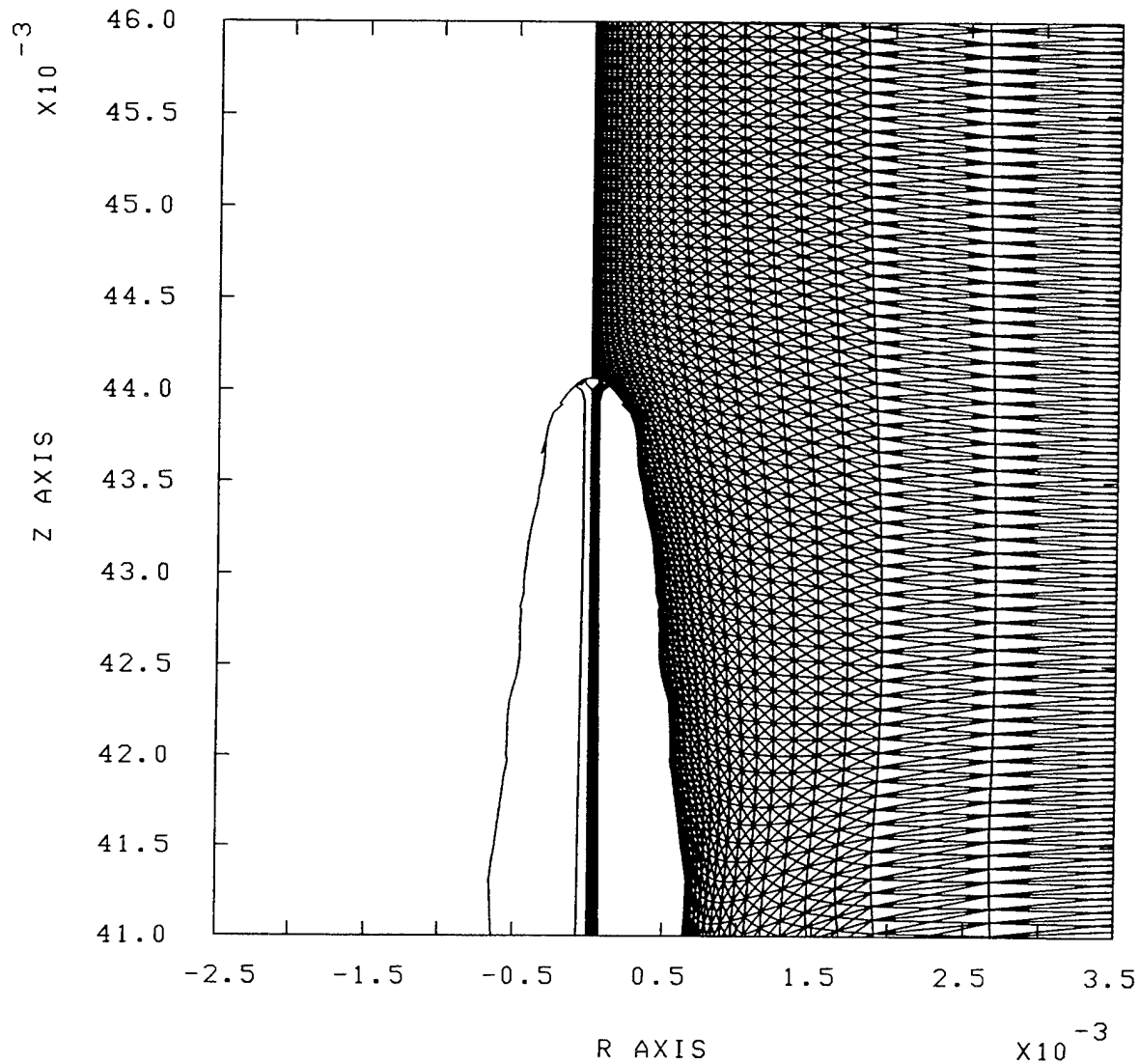
EPIC POST PROCESSOR, POST1 (1992-2) 09:32:36 25-Jul-94
2-D PLANE STRAIN GEOMETRY

Linear SC Jet Penetration ; CASE = 1; TIME = 0.00000080; CYCLE = 1601



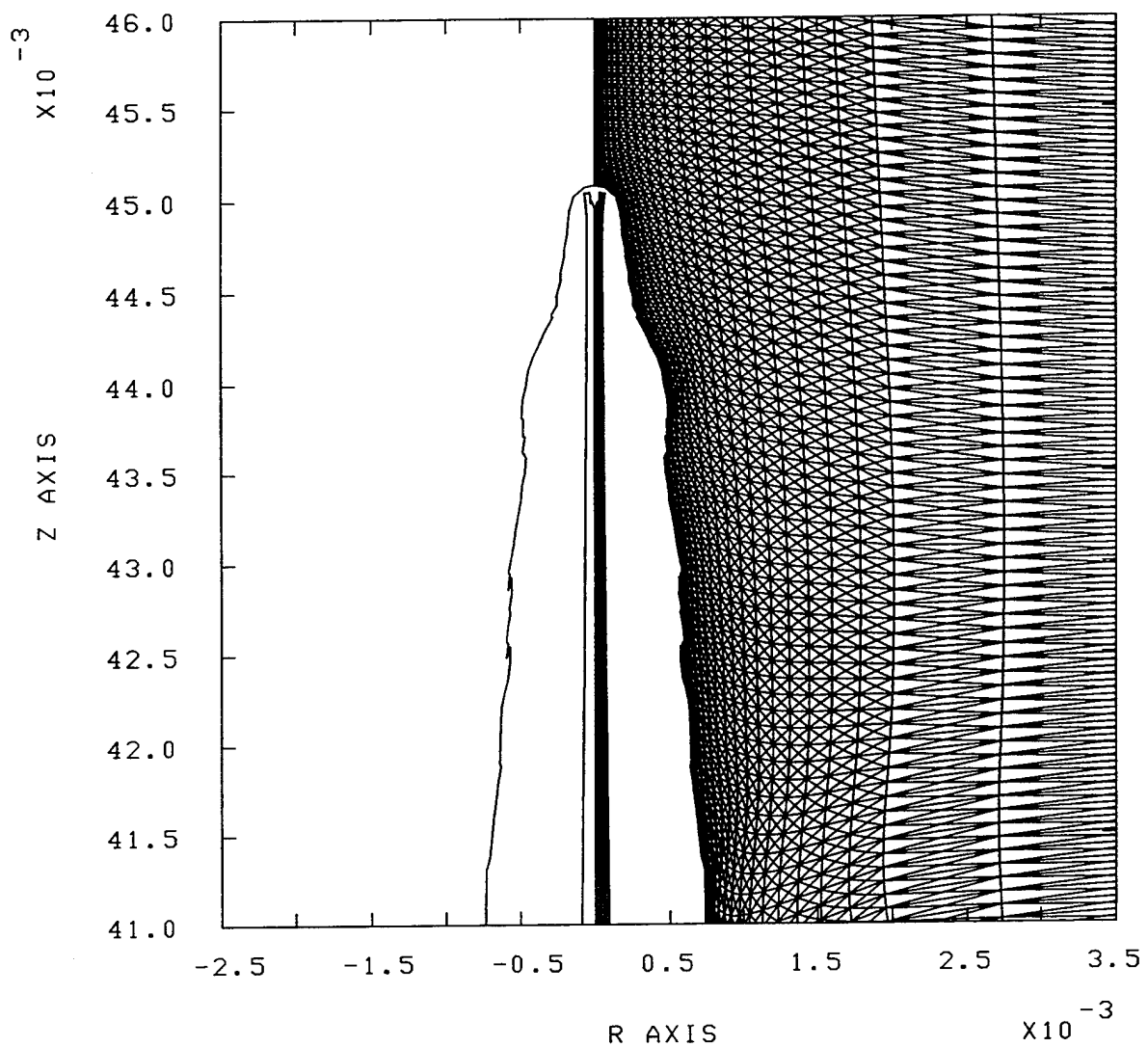
EPIC POST PROCESSOR, POST1 (1992-2) 09:33:16 25-Jul-94
2-D PLANE STRAIN GEOMETRY

Linear SC Jet Penetration ; CASE = 1; TIME = 0.00000120; CYCLE = 2339



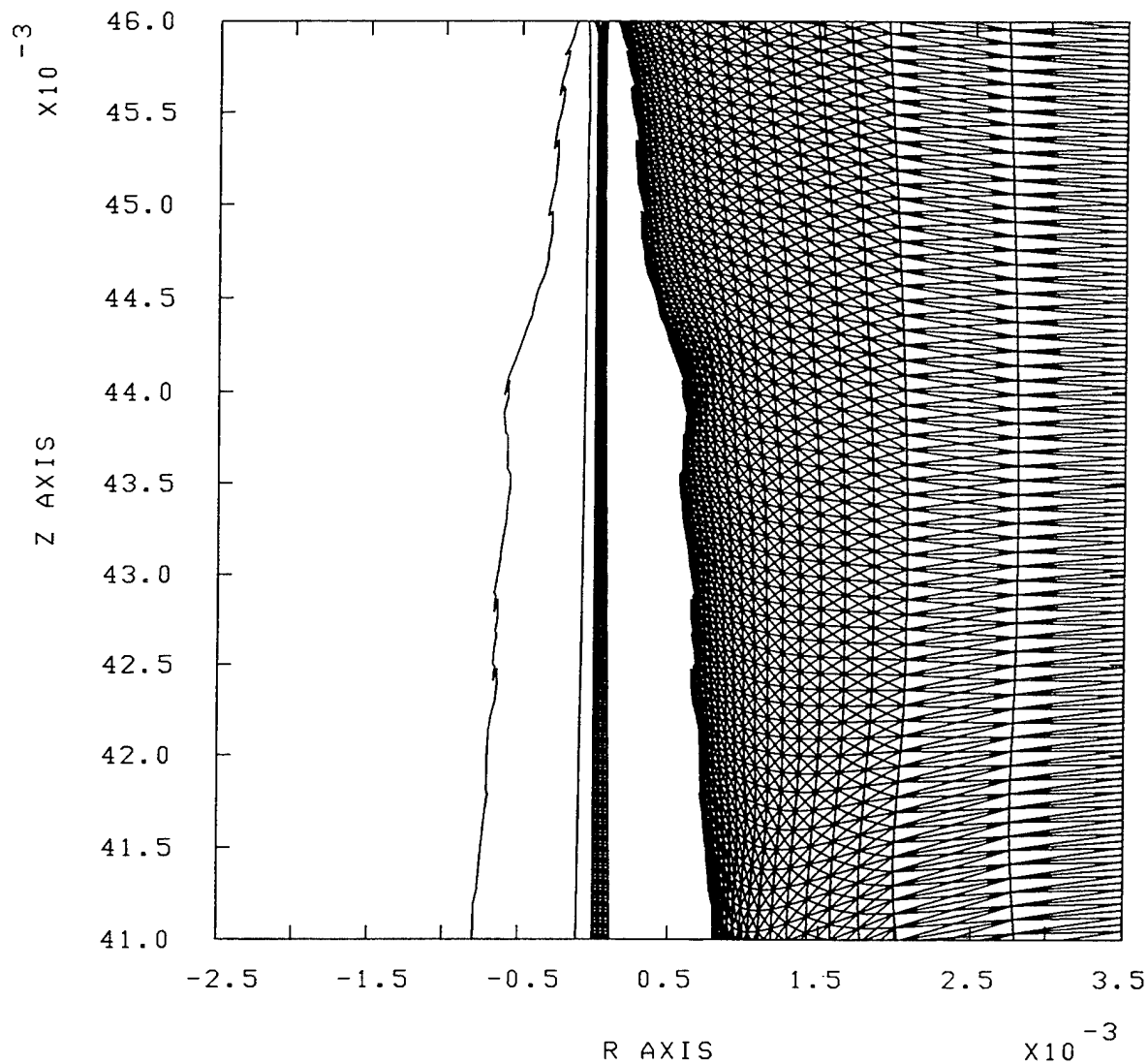
EPIC POST PROCESSOR, POST1 (1992-2) 09:33:52 25-Jul-94
2-D PLANE STRAIN GEOMETRY

Linear SC Jet Penetration ; CASE = 1; TIME = 0.00000160; CYCLE = 2910



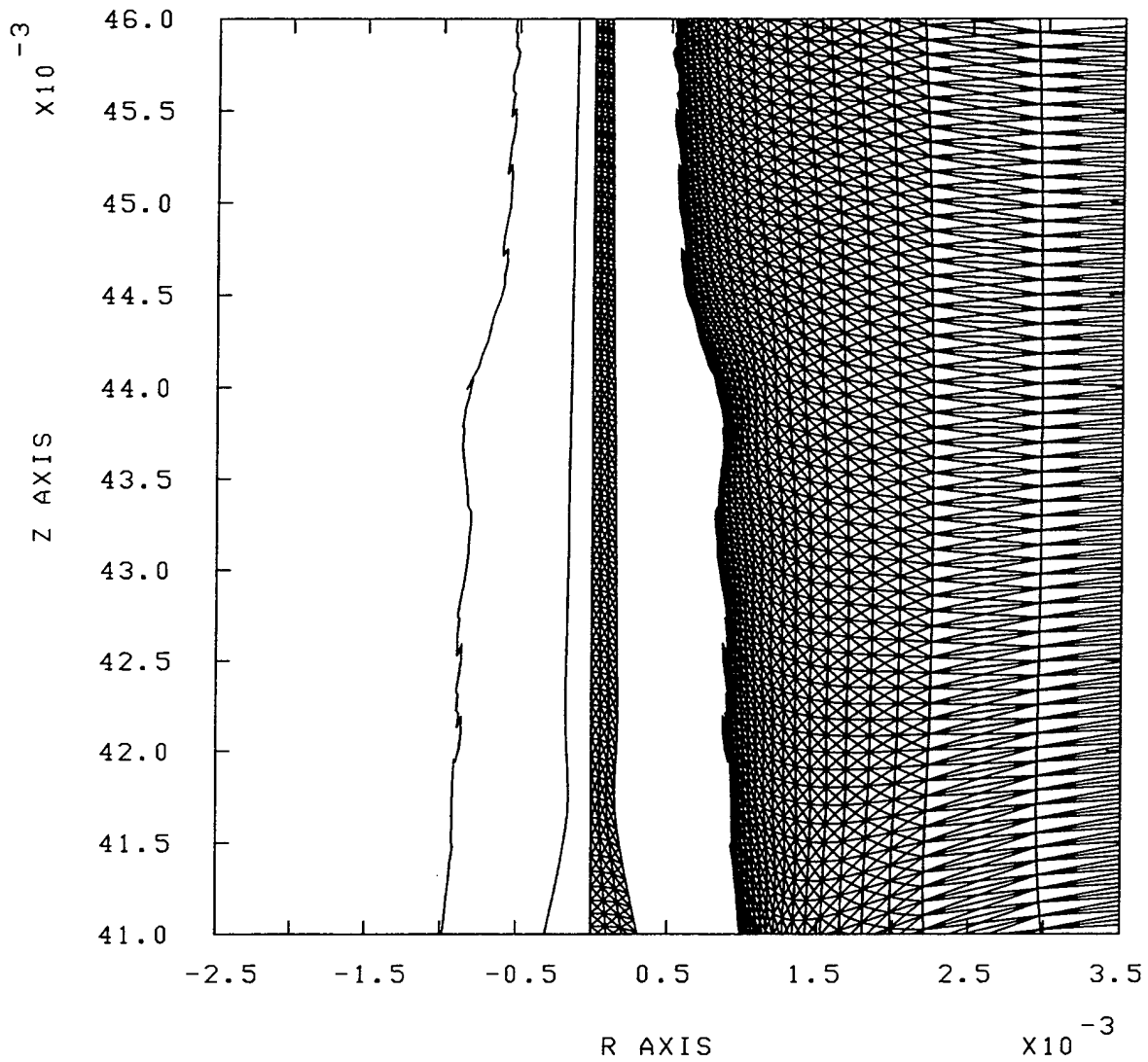
EPIC POST PROCESSOR, POST1 (1992-2) 09:34:40 25-Jul-94
2-D PLANE STRAIN GEOMETRY

Linear SC Jet Penetration ; CASE = 1; TIME = 0.00000200; CYCLE = 3474



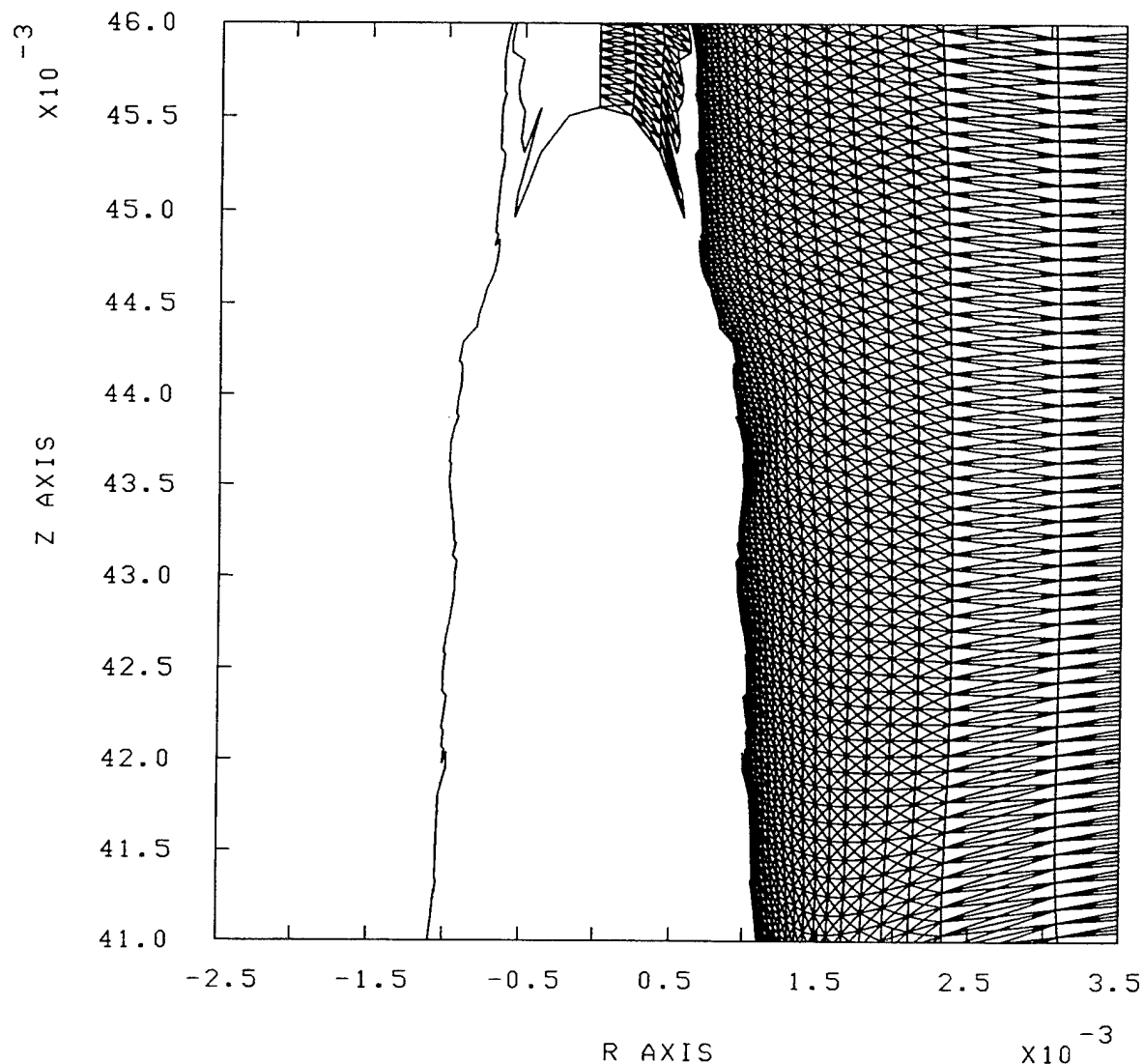
EPIC POST PROCESSOR, POST1 (1992-2) 09:35:26 25-Jul-94
2-D PLANE STRAIN GEOMETRY

Linear SC Jet Penetration ; CASE = 1; TIME = 0.00000400; CYCLE = 6111



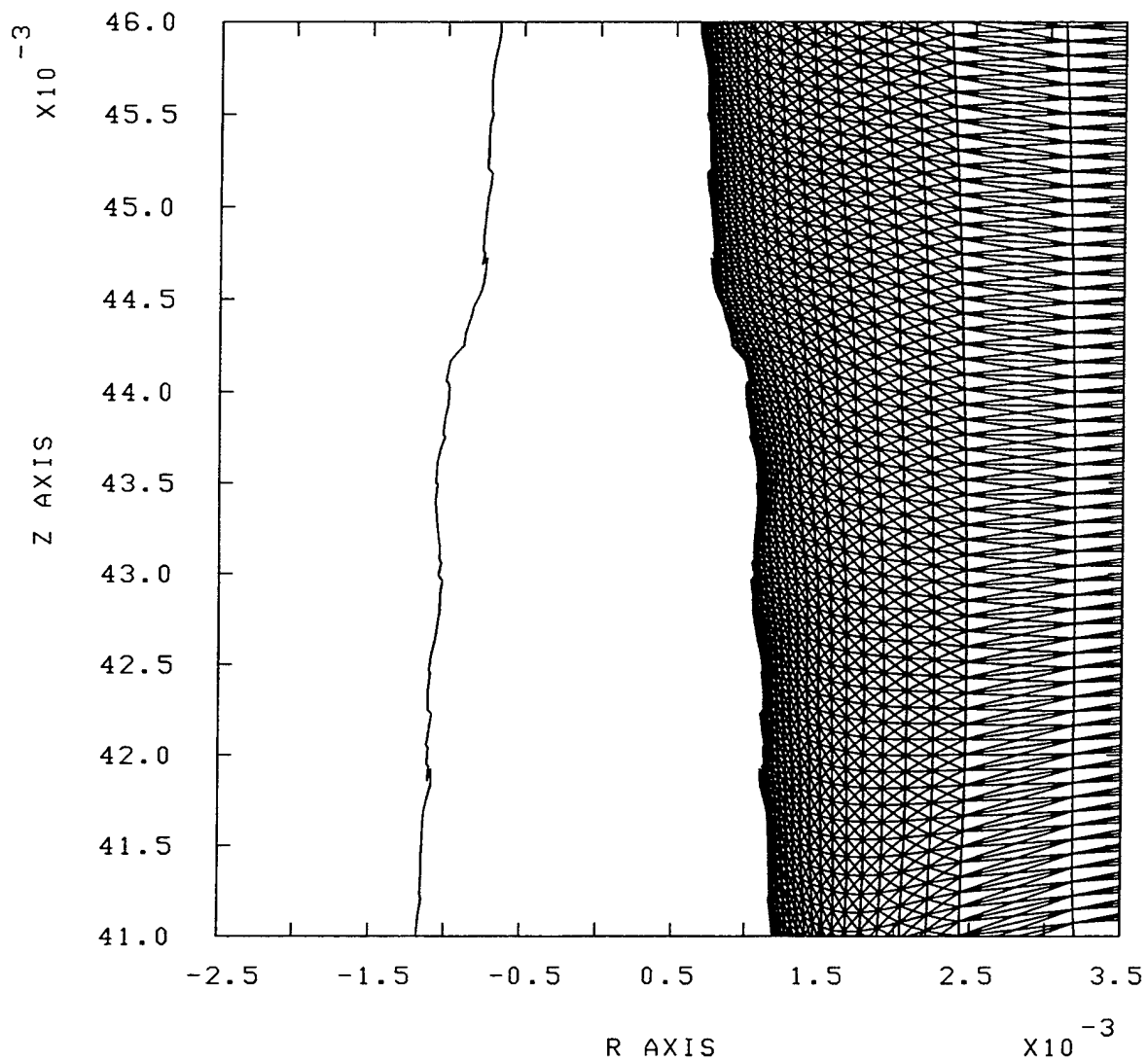
EPIC POST PROCESSOR, POST1 (1992-2) 09:35:58 25-Jul-94
2-D PLANE STRAIN GEOMETRY

Linear SC Jet Penetration ; CASE = 1; TIME = 0.00000600; CYCLE = 8646



EPIC POST PROCESSOR, POST1 (1992-2) 09:36:22 25-Jul-94
2-D PLANE STRAIN GEOMETRY

Linear SC Jet Penetration ; CASE = 1; TIME = 0.00000800; CYCLE = 11163



INTENTIONALLY LEFT BLANK.

<u>NO. OF COPIES</u>	<u>ORGANIZATION</u>
2	ADMINISTRATOR ATTN DTIC DDA DEFENSE TECHNICAL INFO CTR CAMERON STATION ALEXANDRIA VA 22304-6145
1	DIRECTOR ATTN AMSRL OP SD TA US ARMY RESEARCH LAB 2800 POWDER MILL RD ADELPHI MD 20783-1145
3	DIRECTOR ATTN AMSRL OP SD TL US ARMY RESEARCH LAB 2800 POWDER MILL RD ADELPHI MD 20783-1145
1	DIRECTOR ATTN AMSRL OP SD TP US ARMY RESEARCH LAB 2800 POWDER MILL RD ADELPHI MD 20783-1145
<u>ABERDEEN PROVING GROUND</u>	
5	DIR USARL ATTN AMSRL OP AP L (305)

<u>NO. OF COPIES</u>	<u>ORGANIZATION</u>	<u>NO. OF COPIES</u>	<u>ORGANIZATION</u>
1	HEADQUARTERS ATTN SARD TT DR F MILTON PENTAGON WASHINGTON DC 20310-0103	4	COMMANDER ATTN SMCAR FSE T GORA E ANDRICOPOULOS B KNUTELSKY A GRAF US ARMY ARDEC PCTNY ARSNL NJ 07806-5000
1	HEADQUARTERS ATTN SARD TT MR J APPEL PENTAGON WASHINGTON DC 20310-0103	3	COMMANDER ATTN SMCAR TD R PRICE V LINDER T DAVIDSON US ARMY ARDEC PCTNY ARSNL NJ 07806-5000
1	HEADQUARTERS ATTN SARD TT MS C NASH PENTAGON WASHINGTON DC 20310-0103	1	COMMANDER ATTN F MCLAUGHLIN US ARMY ARDEC PCTNY ARSNL NJ 07806-5000
1	HEADQUARTERS ATTN SARD TR DR R CHAIT PENTAGON WASHINGTON DC 20310-0103	5	COMMANDER ATTN SMCAR CCH T S MUSALLI P CHRISTIAN K FEHSAL N KRASNOW R CARR US ARMY ARDEC PCTNY ARSNL NJ 07806-5000
1	HEADQUARTERS ATTN SARD TR MS K KOMINOS PENTAGON WASHINGTON DC 20310-0103	1	COMMANDER ATTN SMCAR CCH V E FENNELL US ARMY ARDEC PCTNY ARSNL NJ 07806-5000
1	DIRECTOR ATTN AMSRL CP CA D SNIDER US ARMY RESEARCH LAB 2800 POWDER MILL ROAD ADELPHI MD 20783-1145	1	COMMANDER ATTN SMCAR CCH J DELORENZO US ARMY ARDEC PCTNY ARSNL NJ 07806-5000
8	DIRECTOR ATTN AMSRL MA P L JOHNSON B HALPIN T CHOU C WHITE J MCLAUGHLIN AMSRL MA PA D GRANVILLE W HASKELL AMSRL MA MA G HAGNAUER US ARMY RESEARCH LAB WATERTOWN MA 02172-0001	2	COMMANDER ATTN SMCAR CC J HEDDERICH COL SINCLAIR US ARMY ARDEC PCTNY ARSNL NJ 07806-5000

<u>NO. OF COPIES</u>	<u>ORGANIZATION</u>	<u>NO. OF COPIES</u>	<u>ORGANIZATION</u>
1	COMMANDER ATTN SMCAR CCH P J LUTZ US ARMY ARDEC PCTNY ARSNL NJ 07806-5000	1	COMMANDER ATTN AMSMC PBM K US ARMY ARDEC PCTNY ARSNL NJ 07806-5000
2	COMMANDER ATTN SMCAR FSA M D DEMELLA F DIORIO US ARMY ARDEC PCTNY ARSNL NJ 07806-5000	1	DIRECTOR ATTN P DUTTA US ARMY CRREL 72 LYME ROAD HANOVER NH 03755
1	COMMANDER ATTN SMCAR FSA C SPINELLI US ARMY ARDEC PCTNY ARSNL NJ 07806-5000	1	DIRECTOR ATTN AMSRL WT L D WOODBURY US ARMY RESEARCH LABORATORY 2800 POWDER MILL ROAD ADELPHI MD 20783-1145
11	DIRECTOR ATTN SMCAR CCB C KITCHENS J KEANE J SANTINI J VASILAKIS G FRIAR R FISCELLA V MONTVORI J WRZOCHALSKI J BATTAGLIA R HASENBEIN SMCAR CCB R S SOPOK BENET LABORATORIES WATERVLIET NY 12189-4050	4	COMMANDER ATTN AMSMI RD W MCCORKLE AMSMI RD ST P DOYLE AMSMI RD ST CN T VANDIVER AMSMI RD ST WF M COLE US ARMY MISSILE COMMAND REDSTONE ARSNL AL 35898-5247
1	COMMANDER ATTN SMCWV QAE Q C HOWD BLDG 44 WATERVLIET ARSENAL WATERVLIET NY 12189-4050	2	DIRECTOR ATTN A CROWSON J CHANDRA US ARMY RESEARCH OFFICE MATH & COMPUTER SCIENCES DIV PO BOX 12211 RSRCH TRI PK NC 27709-2211
1	COMMANDER ATTN SMCWV SPM T MCCLOSKEY BLDG 25 3 WATERVLIET ARSENAL WATERVLIET NY 12189-4050	2	DIRECTOR ATTN G ANDERSON R SINGLETON US ARMY RESEARCH OFFICE ENGINEERING SCIENCES DIVISION PO BOX 12211 RSRCH TRI PK NC 27709-2211
1	COMMANDER ATTN SMCWV QA QS K INSCO WATERVLIET ARSENAL WATERVLIET NY 12189-4050	2	PROJECT MANAGER SADARM PCTNY ARSNL NJ 07806-5000
1	COMMANDER ATTN SMCWV QA QS K INSCO WATERVLIET ARSENAL WATERVLIET NY 12189-4050	2	PM TMAS ATTN SFAE AR TMA COL BREGARD C KIMKER PCTNY ARSNL NJ 07806-5000

<u>NO. OF COPIES</u>	<u>ORGANIZATION</u>	<u>NO. OF COPIES</u>	<u>ORGANIZATION</u>
3	PM TMAS ATTN SFAE AR TMA MD H YUEN J MCGREEN R KOWALSKI PCTNY ARSNL NJ 07806-5000	1	OFFICE OF NAVAL RESEARCH ATTN YAPA RAJAPAKSE MECH DIV CODE 1132SM ARLINGTON VA 22217
2	PM TMAS ATTN SFAE AR TMA MS R JOINSON D GUZIEWICZ PCTNY ARSNL NJ 07806-5000	1	NAVAL ORDNANCE STATION ATTN D HOLMES CODE 2011 ADVANCED SYSTEMS TECHNOLOGY BR LOUISVILLE KY 40214-5245
1	PM TMAS ATTN SFAE AR TMA MP W LANG PCTNY ARSNL NJ 07806-5000	1	DAVID TAYLOR RESEARCH CTR SHIP STRUCTURES AND PROT DEPT ATTN J CORRADO CODE 1702 BETHESDA MD 20084
2	PEO ARMAMENTS ATTN SFAE AR PM D ADAMS T MCWILLIAMS PCTNY ARSNL NJ 07806-5000	2	DAVID TAYLOR RESEARCH CTR ATTN R ROCKWELL W PHYILLAER BETHESDA MD 20054-5000
1	PEO FIELD ARTILLERY SYSTEMS ATTN SFAE FAS PM H GOLDMAN PCTNY ARSNL NJ 07806-5000	5	DIRECTOR ATTN R CHRISTENSEN S DETERESA W FENG F MAGNESS M FINGER LAWRENCE LIVERMORE NATL LAB PO BOX 808 LIVERMORE CA 94550
4	PM AFAS ATTN LTC D ELLIS G DELCOCO J SHIELDS B MACHAK PCTNY ARSNL NJ 07806 5000	1	DIRECTOR ATTN D RABERN MEE 13 MAIL STOP J 576 LOS ALAMOS NATL LAB PO BOX 1633 LOS ALAMOS NM 87545
2	COMMANDER ATTN WL FIV A MAYER WL MLBM S DONALDSON WRIGHT PATTERSON AFB DAYTON OH 45433	2	NAVAL EOD TECH CTR ATTN CODE 6012A A PATEL R GOLD INDIAN HEAD MD 20640-5070
2	NASA Langley RSRCH CTR ATTN AMSRL VS W ELBER AMSRL VS S F BARTLETT JR MAIL STOP 266 HAMPTON VA 23681-0001	1	OAK RIDGE NATIONAL LAB ATTN R M DAVIS PO BOX 2008 OAK RIDGE TN 37831-6195
2	NAVAL SURFACE WARFARE CTR CODE G33 DAHLGREN VA 22448		

<u>NO. OF COPIES</u>	<u>ORGANIZATION</u>	<u>NO. OF COPIES</u>	<u>ORGANIZATION</u>
2	BATTELLE PNL ATTN M SMITH M C C BAMPTON PO BOX 999 RICHLAND WA 99352	1	AAI CORPORATION ATTN TECH LIBRARY PO BOX 126 HUNT VALLEY MD 21030-0126
6	DIRECTOR ATTN C ROBINSON G BENEDETTI W KAWAHARA K PERANO D DAWSON P NIELAN SANDIA NATL LABS PO BOX 969 LIVERMORE CA 94550-0096	1	ARMTEC DEFENSE PRODUCTS ATTN STEVE DYER PO BOX 848 COACHELLA CA 92236
1	PENNSYLVANIA STATE UNIV ATTN RICHARD MCNITT 227 HAMMOND BLDG UNIVERSITY PARK PA 16802	3	ALLIANT TECHSYSTEMS INC ATTN J BODE C CANDLAND K WARD 5901 LINCOLN DR MINNEAPOLIS MN 55346-1674
1	SOUTHWEST RSRCH INSTITUTE ATTN C ANDERSON 6220 CULEBRA RD SAN ANTONIO TX 78284	2	ALLIANT TECHSYSTEMS INC ATTN TIM HOLMQUIST G R JOHNSON 600 SECOND STREET NE HOPKINS MN 55343
1	UCLA MANE DEPT ENGRG IV ATTN H THOMAS HAHN LOS ANGELES CA 90024 1597	1	BALLISTIC IMPACT DYNAMICS ATTN RODNEY RECHT 3650 S CHEROKEE 2 ENGLEWOOD CO 80110
2	UNIV OF DAYTON RESEARCH INST ATTN RAN Y KIM AJIT K ROY 300 COLLEGE PARK AVENUE DAYTON OH 45469-0168	1	CALIFORNIA RSRCH & TECH ATTN DENNIS ORPHAL 5117 JOHNSON DRIVE PLEASANTON CA 94566
2	UNIV OF DELAWARE ATTN J GILLESPE M SANTARE CTR FOR COMPOSITE MATERIALS 201 SPENCER LABORATORY NEWARK DE 19716	1	CHAMBERLAIN MFG CORP R&D DIV ATTN M TOWNSEND PO BOX 2545 WATERLOO IA 50704
1	UNIV OF TEXAS AT AUSTIN ATTN J PRICE CTR FOR ELECTROMECHANICS 10100 BURNET ROAD AUSTIN TX 78758-4497	1	COMPUTNL MECHANICS ASSOC ATTN JONAS A ZUKAS PO BOX 11314 BALTIMORE MD 21239-0314
		1	CUSTOM ANALYTICAL ENGRNG SYS INC ATTN A ALEXANDER STAR ROUTE BOX 4A FLINTSTONE MD 21530

<u>NO. OF COPIES</u>	<u>ORGANIZATION</u>	<u>NO. OF COPIES</u>	<u>ORGANIZATION</u>
1	GEN DYNAMICS LAND SYS DIV ATTN D BARTLE PO BOX 1901 WARREN MI 48090	2	MARTIN MARIETTA CORP ATTN P DEWAR L SPOONAR 230 EAST GODDARD BLVD KING OF PRUSSIA PA 19406
1	IAP RESEARCH INC ATTN A CHALLITA 2763 CULVER AVENUE DAYTON OHIO 45429	2	OLIN CORP FLINCHBAUGH DIV ATTN E STEINER B STEWART PO BOX 127 RED LION PA 17356
3	INSTITUTE FOR ADV TECHNOLOGY ATTN T KIEHNE H FAIR P SULLIVAN S BLESS R SUBRAMANIAN 4030 2 W BRAKER LANE AUSTIN TX 78759	1	OLIN CORP ATTN L WHITMORE 10101 9TH ST NORTH ST PETERSBURG FL 33702
1	INTERFEROMETRICS INC ATTN R LARRIVA VP 8150 LESSBURG PIKE VIENNA VA 22100	2	UNIV OF MINNESOTA AHPCRC ATTN G SELL D AUSTIN 1100 WASHINGTON AVE S MINNEAPOLIS MN 55415
2	KAMAN SCIENCES CORP ATTN D ELDER T HAYDEN N ARI PO BOX 7463 COLORADO SPRINGS CO 80933		<u>ABERDEEN PROVING GROUND</u>
1	DR KENNEDY & ASSOCIATES INC ATTN D KENNEDY PO BOX 4003 MOUNTAIN VIEW CA 94040	21	DIR USARL ATTN AMSRL CI C MERMEGAN 394 AMSRL CI C W STUREK 1121 AMSRL CI CB R KASTE 394 AMSRL CI S A MARK 309 AMSRL SL B P DIETZ 328 AMSRL SL BA J WALBERT 1065 AMSRL SL BL D BELY 328 AMSRL SL I D HASKILL 1065 AMSRL WT P A HORST 390A AMSRL WT PA T MINOR 390 C LEVERITT 390 D KOOKER 390A AMSRL WT PB E SCHMIDT 120 P PLOSTINS 120 AMSRL WT PC R FIFER 390A AMSRL WT PD B BURNS 390 W DRYSDALE 390 K BANNISTER 390 T BOGETTI 390 J BENDER 390 R MURRAY 390
1	LIVERMORE SOFTWARE TECH CORP ATTN J O HALLQUIST 2876 WAVERLY WAY LIVERMORE CA 94550		
2	LORAL VOUGHT SYSTEMS CORP ATTN G JACKSON K COOK 1701 W MARSHALL DR GRAND PRAIRIE TX 75051		
1	LORAL VOUGHT SYS CORP ATTN K HAVENS MS EM 36 PO BOX 650003 DALLAS TX 75265-0003		

<u>NO. OF COPIES</u>	<u>ORGANIZATION</u>	<u>NO. OF COPIES</u>	<u>ORGANIZATION</u>
<u>ABERDEEN PROVING GROUND (CONT.)</u>			
51	DIR USARL ATTN AMSRL WT PD R KIRKENDALL 390 T ERLINE 390 D HOPKINS 390 S WILKERSON 390 C MCCALL 390 D HENRY 390 R KASTE 390 L BURTON 390 J TZENG 390 R LIEB 390 G GAZONAS 390 5 CP M LEADORE 390 AMSRL WT PD ALC A ABRAHAMIAN K BARNES M BERMAN H DAVISON A FRYDMAN T LI W MCINTOSH E SZYMANSKI AMSRL WT T W MORRISON 309 T WRIGHT 309 AMSRL WT TA W GILLICH 390 W BRUCHEY 390 J DEHN 390 AMSRL WT TB K BENJAMIN 309 T DORSEY 309 R FREY 309 F GREGORY 309 W HILLSTROM 309 W LAWRENCE 309 O LYMAN 1185 J STARKENBERG 309 L VANDE KIEFT 309 J WATSON 309 V BOYLE 309 S STEGALL 1185 5 CP AMSRL WT TC K KIMSEY 309 R COATES 309 W DE ROSSET 309 F GRACE 309 M LAMPSON 309 D SCHEFFLER 309	38	DIR USARL ATTN AMSRL WT TC B SORENSEN 309 R SUMMERS 309 E WALKER 309 W WALTERS 309 AMSRL WT TD D DIETRICH 309 G RANDERS PEHRSON 309 J HUFFINGTON 309 A DAS GUPTA 309 J SANTIAGO 309 K FRANK J HARRISON M SCHEIDLER S SEGLETES 5 CP J WALTER C PAXTON 5 CP AMSRL WT NC R LOTTERO 309 R PEARSON 309 S SCHRAML 309 AMSRL WT W C MURPHY 120 AMSRL WT WA H ROGERS 394 B MOORE 394 A BARAN 394 AMSRL WT WB F BRANDON 120 W D'AMICO 120 AMSRL WT WC J ROCCHIO 120 AMSRL WT WD A ZIELINSKI 120 J POWELL 120 A PRAKASH 120 AMSRL WT WE J TEMPERLEY 120 J THOMAS 394

INTENTIONALLY LEFT BLANK.

USER EVALUATION SHEET/CHANGE OF ADDRESS

This Laboratory undertakes a continuing effort to improve the quality of the reports it publishes. Your comments/answers to the items/questions below will aid us in our efforts.

1. ARL Report Number ARL-TR-788 Date of Report July 1995

2. Date Report Received _____

3. Does this report satisfy a need? (Comment on purpose, related project, or other area of interest for which the report will be used.) _____

4. Specifically, how is the report being used? (Information source, design data, procedure, source of ideas, etc.)

5. Has the information in this report led to any quantitative savings as far as man-hours or dollars saved, operating costs avoided, or efficiencies achieved, etc? If so, please elaborate. _____

6. General Comments. What do you think should be changed to improve future reports? (Indicate changes to organization, technical content, format, etc.)

Organization _____

CURRENT
ADDRESS

Name _____

Street or P.O. Box No. _____

City, State, Zip Code _____

7. If indicating a Change of Address or Address Correction, please provide the Current or Correct address above and the Old or Incorrect address below.

Organization _____

OLD
ADDRESS

Name _____

Street or P.O. Box No. _____

City, State, Zip Code _____

(Remove this sheet, fold as indicated, tape closed, and mail.)
(DO NOT STAPLE)